UNIVERSITÉ DE STRASBOURG

ÉCOLE DOCTORALE DES SCIENCES CHIMIQUES

Institue de Chimie et procèdes pour l'Energie, l'environnement et la santé

THÈSE   présentée par :

Qinqin JI

soutenue le : **3 février 2017**

pour obtenir le grade de : **Docteur de l'université de Strasbourg**

Discipline/ Spécialité : Chimie / Catalyse hétérogène

The synthesis of higher alcohols from CO_2 hydrogenation with Co, Cu, Fe-based catalysts

---

THÈSE dirigée par :
  Mme ROGER Anne-Cécile   Professeur, ICPEES - Université de Strasbourg

RAPPORTEURS :
  Mme BATIOT DUPEYRAT Catherine   Professeur, IC2MP - Université de Poitiers
  M. KHODAKOV Andrei   Directeur de recherche, UCCS -   Université Lille 1

AUTRES MEMBRES DU JURY :
  M. LOUIS Benoît   Directeur de recherche, Institut de Chimie – Strasbourg

ACKNOWLEDGEMENTS

Résumé

1 Introduction

En conséquence de la consommation des énergies fossiles, les émissions anthropiques de CO_2 à l'échelle mondiale ne cessent de croitre. Elles ont triplé de 12 à 35 Gt/an entre 1965 et 2013[1].Ces émissions renforcent l'effet de serre qui fait augmenter la température moyenne de l'atmosphère terrestre. Afin de limiter l'échauffement moyen de l'atmosphère à 2°C par rapport à l'ère préindustrielle, il faut diviser par deux les émissions annuelles de CO_2 (référence de l'année 2009) d'ici 2050.

Toutes les voies de valorisation chimique ou énergétique de CO_2 vont dans le sens de la diminution de ces émissions. Une de ces voies est son hydrogénation en produits énergétiques ou de haute valeur ajoutée. La synthèse d'alcools supérieurs fait partie des routes actuellement à l'étude. Les mélanges d'alcools issus de CO_2 peuvent être additionnés à l'essence en satisfaisant les critères européens sur les pourcentages de renouvelables dans les carburants [2]. De plus ils permettent d'augmenter l'indice d'octane de l'essence et d'en réduire la volatilité.

Mon travail de thèse propose la synthèse et l'optimisation de catalyseurs de type spinelle pour la synthèse d'alcools supérieurs à partir de mélanges CO_2/H_2. La première partie du travail consiste en l'étude des spinelles massifs comme catalyseurs, dans un second temps leur dispersion sur deux types de supports de grande surface a été étudiée. Enfin, l'ajout de promoteurs alcalins a été étudié.

L'activité des différents matériaux après réduction permet de mieux comprendre les mécanismes mis en jeu pour les différentes familles de catalyseurs.

2 Synthèse des catalyseurs

Les catalyseurs sont préparés par la méthode pseudo sol-gel qui est basée sur la décomposition des précurseurs de type propionates [3].Cette méthode consiste à

dissoudre les sels de départ appropriés, c'est-à-dire qui conduiront exclusivement à l'obtention de propionates, dans de l'acide propionique à chaud en vue de l'obtention de solutions de concentration 0,12 mol/L en cation. Les sels de départ pour Co, Cu, Fe sont l'acétate de cobalt (II) hydraté, l'acétate de cuivre (II) hydraté, l'acétate de fer(II) anhydre. Après dissolution de chaque sel métallique et chauffage, les solutions de propionates sont mélangées dans un ballon et chauffées à reflux durant 90 minutes. Le solvant est ensuite évaporé jusqu'à l'obtention d'une résine. Cette résine est calcinée durant 6 h à 800 °C après une montée en température de 2 °C·min^{-1}.

Pour les catalyseurs avec support (nanotubes de carbone et TUD-1), la méthode suivante d'imprégnation est utilisée : la résine a été redissoute dans de l'acide propionique à une concentration contrôlée, la solution obtenue est déposée goutte à goutte sur les supports jusqu'à obtention de la teneur en spinelle désirée. Les supports imprégnés sont ensuite séchés à 100 °C et calcinés à 800 °C durant 6 h pour cristalliser les spinelles sur les supports.

3 Caractérisation des catalyseurs

Diverses techniques de caractérisation ont été employées afin de vérifier la structure (diffraction des rayons X), la texture (physisorption d'azote), la réductibilité (réduction en température programmée) des catalyseurs préparés.

Quatre séries de catalyseurs massifs de type spinelle ont été synthétisés : $CoFe_2O_4$, $CuFe_2O_4$, $CuCo_2O_4$, $Co_{0.5}Cu_{0.5}Fe_2O_4$, nommés CoFe-precursor-800, CuFe-precursor-800, CuCo-precursor-800, CoCuFe-precursor-800.

CuFe-precursor-800 a été ensuite été déposé sur différents supports (nanotubes de carbone et TUD-1).

Enfin, l'ajout de promoteur à CuFe-precursor sur nanotubes de carbone a été étudié.

3.1 Les caractérisations des catalyseurs

3.1.1 Diffraction des rayons X

La structure cristalline des catalyseurs ($CoFe_2O_4$, $CuFe_2O_4$, $CuCo_2O_4$,

$Cu_{0.5}Co_{0.5}Fe_2O_4$) est présentée Figure 1 (a),(b),(c) et (d).
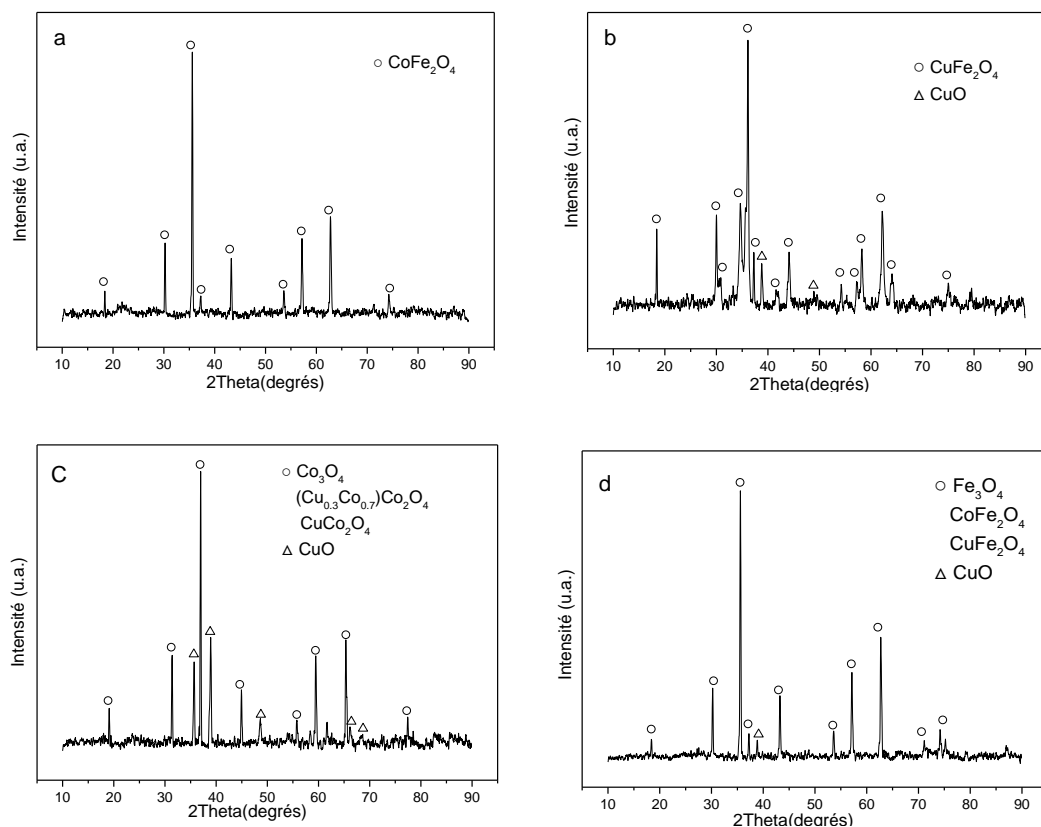
Figure 1 Diffractogramme de a) CoFe-precursor-800, b) CuFe-precursor-800, c) CuCo-recursor-800, d) CuCoFe-precursor-800

Selon les diffractogrammes, seul le spinelle CoFe-precursor-800 pur a pu être obtenu. Pour CuFe-precursor-800, la phase CuO a été mise en évidence en plus du spinelle $CuFe_2O_4$. Pour CuCo-precursor-800, le spinelle n'est pas pur, CuO est également présent, la formation de Co_3O_4 est également très probable. Pour CoCuFe-precursor-800, CuO, $CoFe_2O_4$ et $CuFe_2O_4$ sont présents.

3.1.2 Réduction à température programmée

La Figure 2 présente les profils de consommation d'H_2 en montée en température pour les 4 matériaux spinelle.
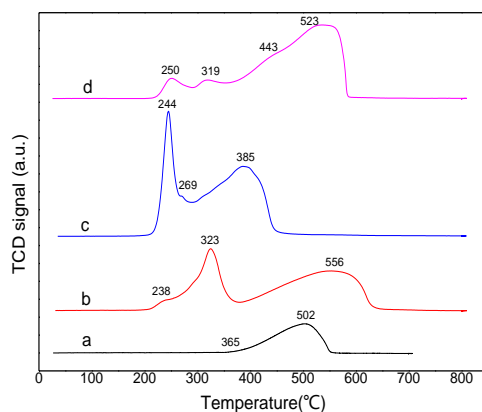
Figure 2 Profils TPR des catalyseurs : a) CoFe-precursor-800, b)CuFe-precursor-800,
c)CuCo-precursor-800 et d)CoCuFe-precursor-800

Selon les profils des réductions, et dans le but de générer une phase métallique active en hydrogénation de CO_2 suffisamment dispersée, la température de réduction de 400 °C a été choisie pour le prétraitement réducteur des catalyseurs.

Une analyse par DRX des catalyseurs préréduits (Figure 3) a montré que seule une phase métallique d'alliage CoFe est obtenue pour le spinelle Co-Fe. Le spinelle Cu-Fe est seulement partiellement réduit, la phase métalique Cu-Fe coexiste avec la phase spinelle. Pour $CuCo_2O_4$ la réduction en métal Cu et Co est totale. Pour le spinelle Co-Cu-Fe les phases métalliques d'alliage CoFe et Cu sont obtenues.
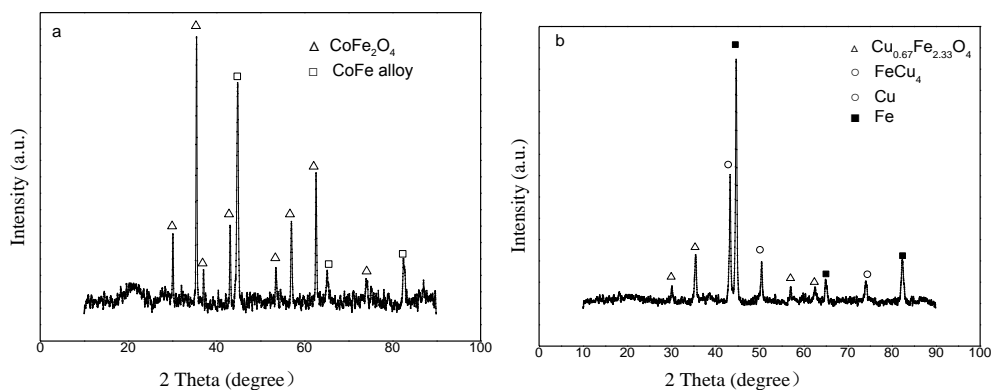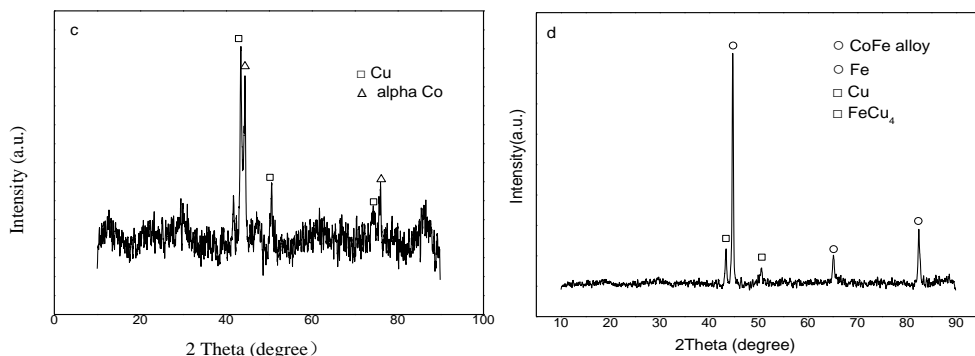
Figure 3 Diffractogramme de catalyseurs après partiel réduction a) CoFe-precursor-800, b) CuFe-precursor-800, c) CuCo-precursor-800, d) CuCoFe-precursor-800

3.2 Test catalytiques

Après être réduit à 400 °C durant 1 heure, les tests de catalyseurs sont menés à différentes températures entre 250 °C et 350 °C et à des pressions de 50bar avec un GHSV (calculé dans les conditions standard de T et P) de $5000h^{-1}$, le rapport de H_2 / CO_2 est de 3, le débit total gazeux est 50 mL.min^{-1}. La Figure 4 présente les conversions de CO_2 et H_2 obtenus à 250 °C, 300 °C et 350 °C pour les 4 catalyseurs.

Figure 4 Conversions de a) CO_2 et b) H_2 à 250 °C, 300 °C et 350 °C, 50 bar.

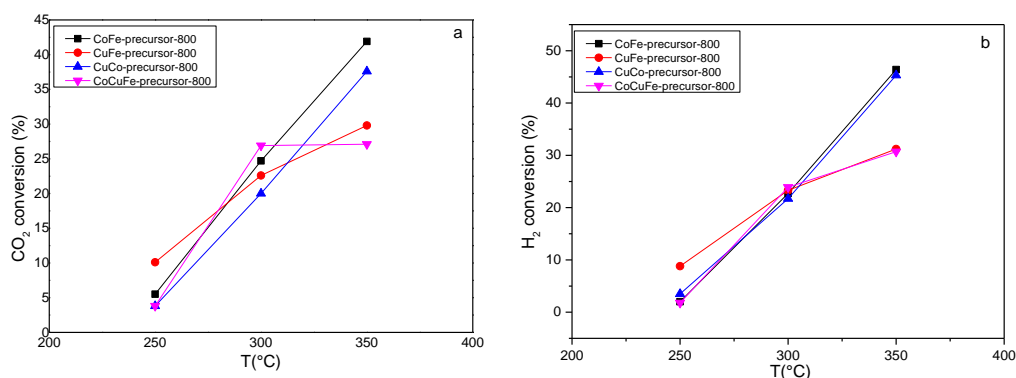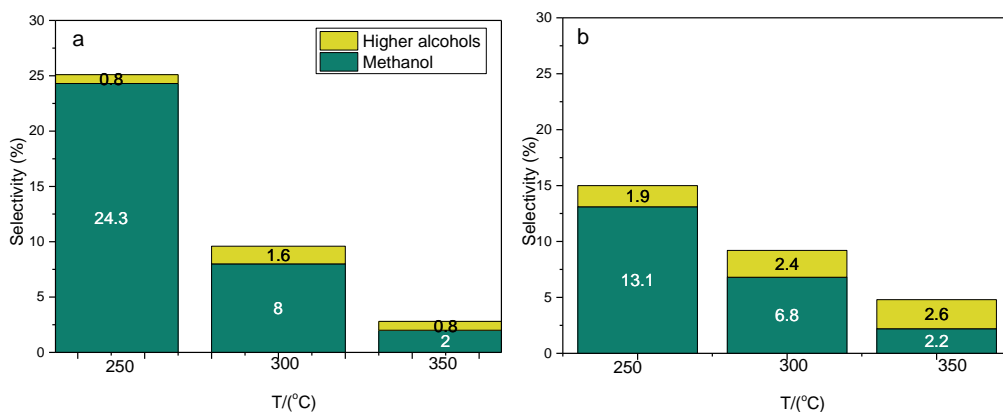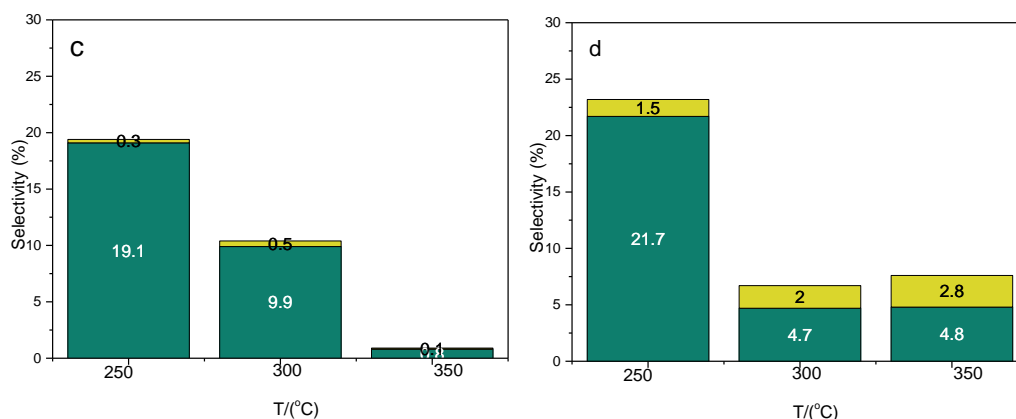Figure 5 Les sélectivités des produits obtenus pour les différents catalyseurs a) CoFe-precursor-800, b) CuFe-precursor-800, c) CuCo-precursor-800, d) CuCoFe-precursor-800 à 250 °C,300 °C 350 °C, 50 bar

Selon les Figure 4 et Figure 5, les conversions augmentent avec la température pour tous les catalyseurs. Pour les alcools, les sélectivités des alcools totaux et du méthanol ont beaucoup diminué lorsque la température de réaction augmente. CoFe-precursor-800 présente une sélectivité la plus élevée des alcools totaux (25,1%) et du méthanol (24,3%) à 250 °C, mais diminuée à 2,8% (alcools totaux) et 2,0% (méthanol) à 350 °C. C'est également le cas pour le catalyseur CuFe-précurseur-800 et CuCo-précurseur-800, les sélectivités des alcools totaux ont diminué de 15,0% à 4,8% et de 19,4% à 0,9% respectivement avec une température augmentée de 250 °C à 350 °C. CuCoFe-precursor-800 est un peu différent, bien que les sélectivités des alcools totaux et du méthanol aient diminué de 250 °C à 300 °C (23,2% à 6,7% et 21,7% à 4,7%), ils ont augmenté un peu lorsque la température a augmenté à 350 °C. Les productivités les plus élevées d'alcools totaux et de méthanol ont été observées à 300 °C, à l'exception de CuCoFe-precursor-800, pour lequel la température optimale est de 350 °C.

La tendance des sélectivités et des productivités des alcools supérieurs est la même entre le catalyseur CoFe-precursor-800 et le CuCo-precursor-800. Les sélectivités les plus élevées sont respectivement 1,6% et 0,5% à 300 °C. Le comportement du CuFe-precursor-800 et CuCoFe-precursor-800 est similaire, les sélectivités les plus élevées des alcools supérieurs sont respectivement 2,6% et 2,8% à

350 ºC. Le CuFe-precursor-800 présente une productivité d'alcools la plus élevée (11,2 g · gcata^{-1} · h^{-1}) à 350 ºC. On peut également constater qu'à une température fixée, les sélectivités et les productivités des alcools supérieurs sont plus élevées dans les réactions avec le cuivre présent dans les catalyseurs

4 Les catalyseurs avec supports (CNTs et TUD-1)

Afin d'augmenter la surface active des catalyseurs et la sélectivité en alcools supérieurs, leur dépôt sur des supports de grande surface spécifique a été envisagé. L'étude a porté sur le spinelle Cu-Fe (meilleurs rendement et sélectivité en alcools supérieurs) et sur deux types de supports : des nanotubes de carbone commerciaux (CNTs) et une silice de grande surface TUD-1 synthétisée au laboratoire. Différents échantillons de différentes teneurs en spinelle ont été synthétisés : de 10 à 70% en masse.

4.1 Les caractérisations des catalyseurs

4.1.1 Surface spécifique

La surface spécifique par BET, le volume des pores et la densité apparente des catalyseurs et des supports sont indiqués dans le Tableau1.

Tableau 1 S_{BET}, volume poreux, densité apparente des échantillons

Echantillons	S_{BET} $(m^2·g^{-1})$	V_{total} $(cm^3·g^{-1})$	Density $(g·cm^{-3})$
10CuFeCNTs	361	1,6	0,16
30CuFeCNTs	276	1,1	0,20
50CuFeCNTs	200	0,7	0,30
70CuFeCNTs	101	0,3	0,43
pure CNTs [a]	238	1,0	0,31
30CuFeTUD-1	199	0,3	0,71
pure TUD-1	303	0,4	0,65

Par rapport au support CNTs seul, la surface de 30CuFeCNTs augmente de 238 à 276 $m^2 g^{-1}$, A teneur plus élevée, la surface de 70CuFeCNTs chute à 101 $m^2 g^{-1}$,

L'échantillon 30CuFeCNTs a donc été choisi pour la réactivité catalytique, La même teneur de 30% en masse a été déposée sur TUD-1, pour comparaison.

4,1,2 Diffraction des rayons X

La Figure 6 présente les diffractogrammes des catalyseurs avec supports CNTs et TUD-1,
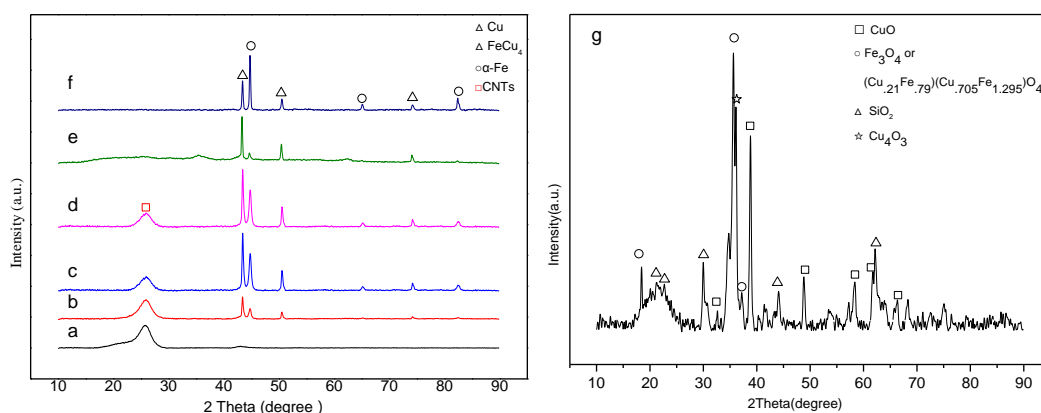
Figure 6 Diffractogrammes de (a) pure CNTs calcined under N_2 atmosphere, (b) 10CuFeCNTs, (c) 30CuFeCNTs, (d) 50CuFeCNTs, (e) 70CuFeCNTs, (f) CuFe-precursor-N_2, (g)30CuFeTUD-1

Parce que le catalyseur sur support CNTs est calciné sous atmosphère inerte de façon à préserver les nanotubes de l'oxydation, seuls les phases métalliques Fe et Cu sont présentes après calcination. Pour le 30CuFeTUD-1, calciné sous air, contrairement au catalyseur massif en poudre, la phase spinelle $CuFe_2O_4$ n'est pas obtenue, Le dépôt sur TUD-1 engendre un nombre de phases plus important dans l'échantillon : les oxydes simples, en addition à différents oxydes mixtes,

4,1,3 Réduction à température programmée

Les profils H_2-TPR des échantillons sont présentés dans la
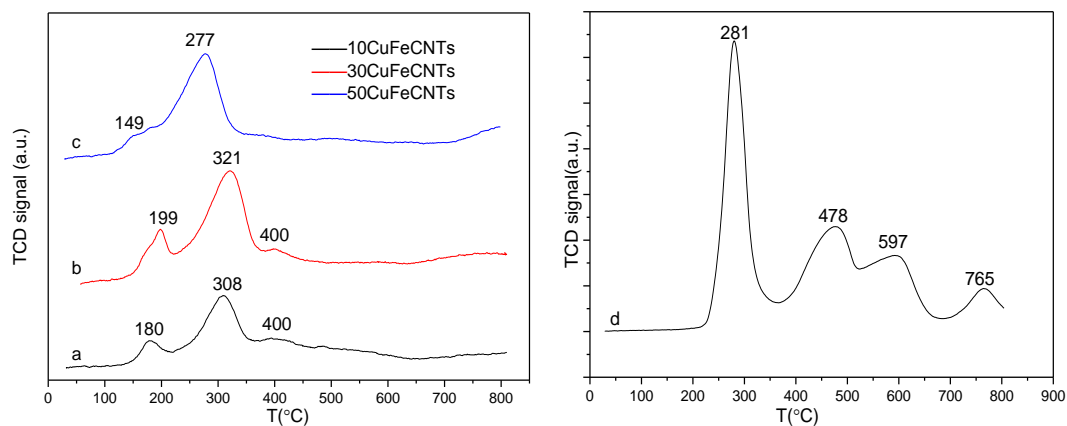
Figure 7. La consommation d'H$_2$ des échantillons est reportée dans le Tableau2.
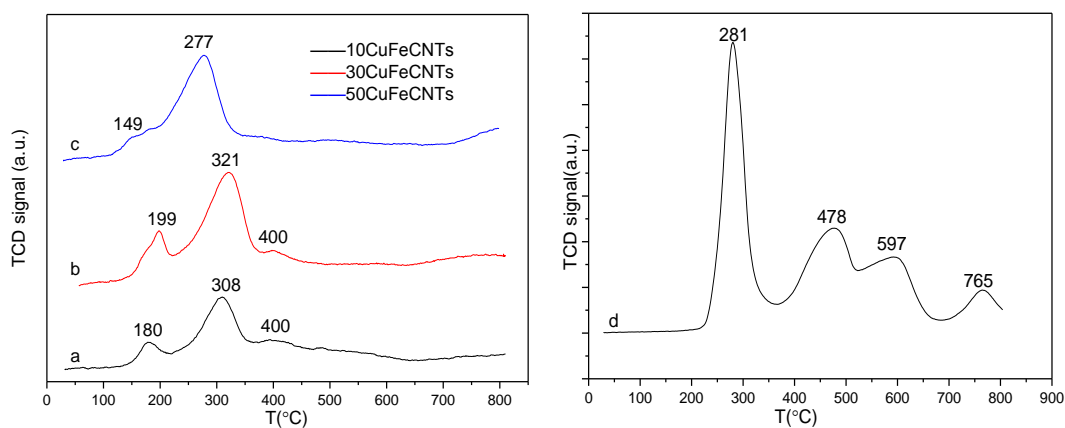
Figure 7 Profils de réduction de a) 10CuFeCNTs, b) 30CuFeCNTs, c) 50CuFeCNTs et d) 30CuFeTUD-1

Tableau 2 La consommation d'H$_2$ des échantillons 30CuFeCNTs et 30CuFeTUD-1

Catalyseurs	La consommation de H$_2$ (mmol·g^{-1})	
	expérimentale	théorique
10CuFeCNTs	0,39	1,41
30CuFeCNTs	0,51	5,27
50CuFeCNTs	0,48	10,03
30CuFeTUD-1	4,44	5,00

La consommation d'H$_2$ des échantillons avec CNTs est faible, au maximum de 0,51 mmol g^{-1} et, dans le cas de 30CuFeTUD-1, est de 4,44 mmol g^{-1}. Ceci est consistant avec les résultats DRX montrant que seul le métal est obtenu après

x

synthèse de 30CuFeCNTs. Le profil de réduction de 30CuFeTUD-1 est logiquement assez différent de celui obtenu pour $CuFe_2O_4$ (Figure 2). Le dépôt sur TUD-1 stabilise différents oxydes en interaction différente avec le support. Le pic à 279 °C est cohérent avec la réduction de CuO. Les autres oxydes présentent des températures de réduction supérieures à 400 °C, température de prétraitement réducteur.

4,2 Test catalytiques

Les mêmes conditions de réaction que pour les spinelles massifs ont été utilisées. Les conversions en CO_2 et en H_2 des catalyseurs 10CuFeCNTs, 30CuFeCNTs, 50CuFeCNTs, 70CuFeCNTs et 30CuFeTUD-1 à 250 °C, 300 °C et 350 °C sont montrées dans Figure 8 (a) et (b), Les sélectivités des produits sont représentées dans la Figure 9.

Figure 8 Conversions de a) CO_2 et b) H_2 à 250 °C, 300 °C et 350 °C, 50 bar

Figure 9 Les sélectivités des produits obtenus pour les différents catalyseurs a) 10CuFeCNTs, b) 30CuFeCNTs, c) 50CuFeCNTs, d) 70CuFeCNTs, e) 30CuFeTUD-1 à 250 °C, 300 °C 350 °C, 50 bar

Pour tous les catalyseurs, la réactivité à 250 °C est très faible. Les conversions de CO_2 et d' H_2 sont inférieures à 10%. Avec l'augmentation de la température de réaction de 250 °C à 350 °C, la conversion de CO_2 a fortement augmenté jusqu'à 30% ou plus, à l'exception de 10CuFeCNT et 30CuFeTUD-1. La conversion d' H_2 est également augmentée, en particulier pour les catalyseurs 30CuFeCNTs, 50CuFeCNTs et 70CuFeCNT, pour lesquels la conversion d' H_2 a été augmentée jusqu'à environ 40%. Le catalyseur 50CuFeCNT présente une conversion des réactifs la plus forte, de 34,1% pour CO_2 et de 43,4% pour H_2, à 350 °C. Les conversions sont similaires pour 30CuFeCNT et 70CuFeCNT : les conversions de CO_2 sont de 19,3% et 20,6% à 300 °C, 33,5% et 33,0% à 350 °C respectivement. Les conversions d' H_2 se situent respectivement à 19,4% et 22,1% à 300 °C et à 39,1% et 40,1% à 350 °C. Pour 10CuFeCNT, en raison du faible taux de charge des phases actives, les conversions de

CO_2 et d' H_2 sont inférieures à 10% même à 350 °C et l'activité de 10CuFeCNT à 250 °C est trop faible pour être quantifiée.

La conversion de CO_2 et d' H_2 de CuFe sur le support CNT est beaucoup plus élevée que celle de CuFe sur le support TUD-1 au même taux de charge de CuFe à 30%. Par exemple, à 350 °C, la conversion de CO_2 est de 33,5% pour 30CuFeCNT comparée à 21,9% pour 30CuFeTUD-1.

Comparé aux résultats obtenus sur le CuFe-precursor-800 (les conversions de CO_2 sont de 10,1%, 22,6%, 29,8% à 250 °C, à 300 °C et 350 °C respectivement et les conversions d' H_2 sont de 8,8%, 23,3%, 31,2 % À 250 °C, à 300 °C et 350 °C respectivement), les conversions obtenues avec le catalyseur 30CuFeTUD-1 sont inférieures à 250 °C, à 300 °C et 350 °C. Pour les catalyseurs CuFeCNT, bien que la conversion de CO_2 et d' H_2 soit inférieure à 250 °C et 300 °C, les conversions obtenues à 350 °C sont légèrement supérieures à celles de CuFe-precursor-800.

Les sélectivités et les productivités les plus élevées des alcools supérieurs ont été obtenues dans la réaction avec 30CuFeCNT en tant que catalyseur à 350 °C, les sélectivités et les productivités sont de 8,7% et 108,9 $g \cdot kg^{-1} \cdot h^{-1}$ respectivement,

Ceci peut être expliqué par la surface sp2-C qui facilite l'adsorption et l'activation de l'hydrogène, ces H-espèces actives adsorbées peuvent être facilement transférées aux métaux actifs via le spillover d'hydrogène CNT-assisté [4], ainsi que par l'augmentation du nombre de sites métalliques actifs sur la surface.

5 Effet de promoteurs

Les alcalins, par leur aptitude à donner des électrons, sont de bons promoteurs pour la synthèse d'alcools et d'hydrocarbures supérieurs. Une teneur de 1,0 % en masse de K, Na, ou Cs et de 0,5% et 1,5% en masse de K a été additionnée à 30CuFeCNTs. Les mêmes conditions de réaction ont été utilisées.
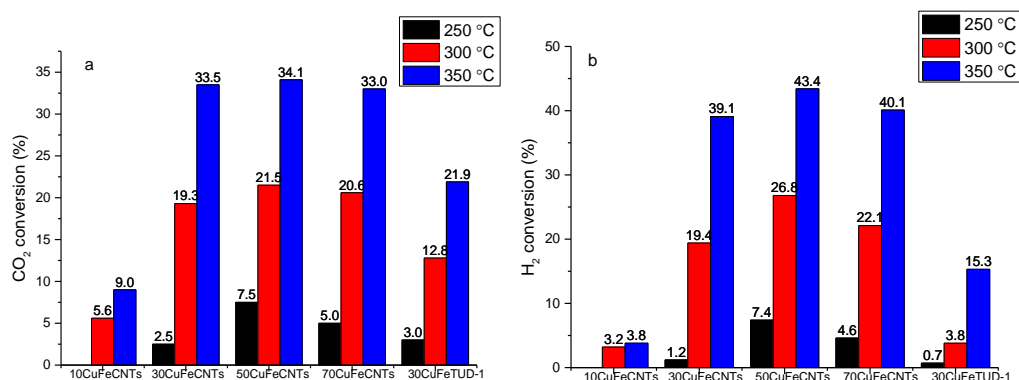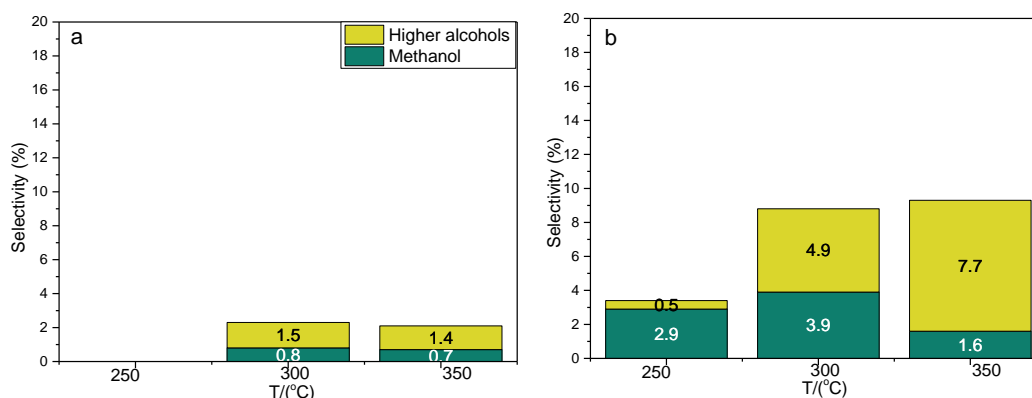
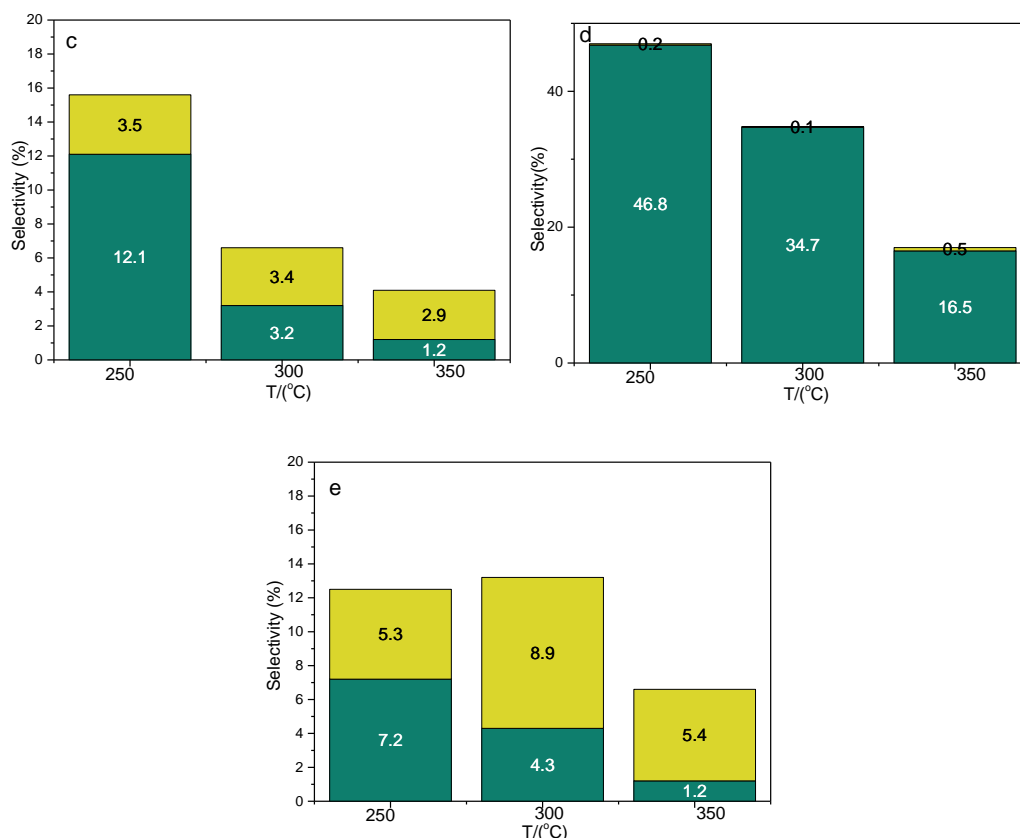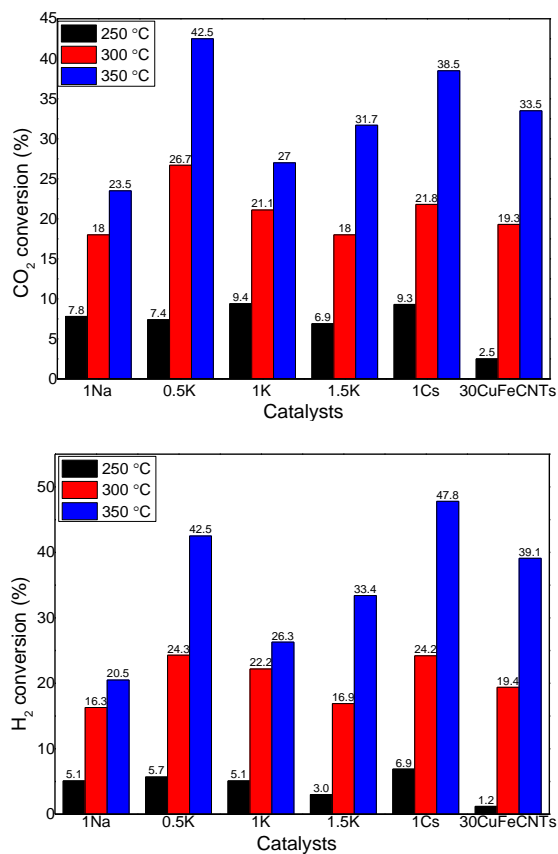Figure 10 Conversions de CO_2 et H_2 à 250 °C, 300 °C, 350 °C, 50 bar
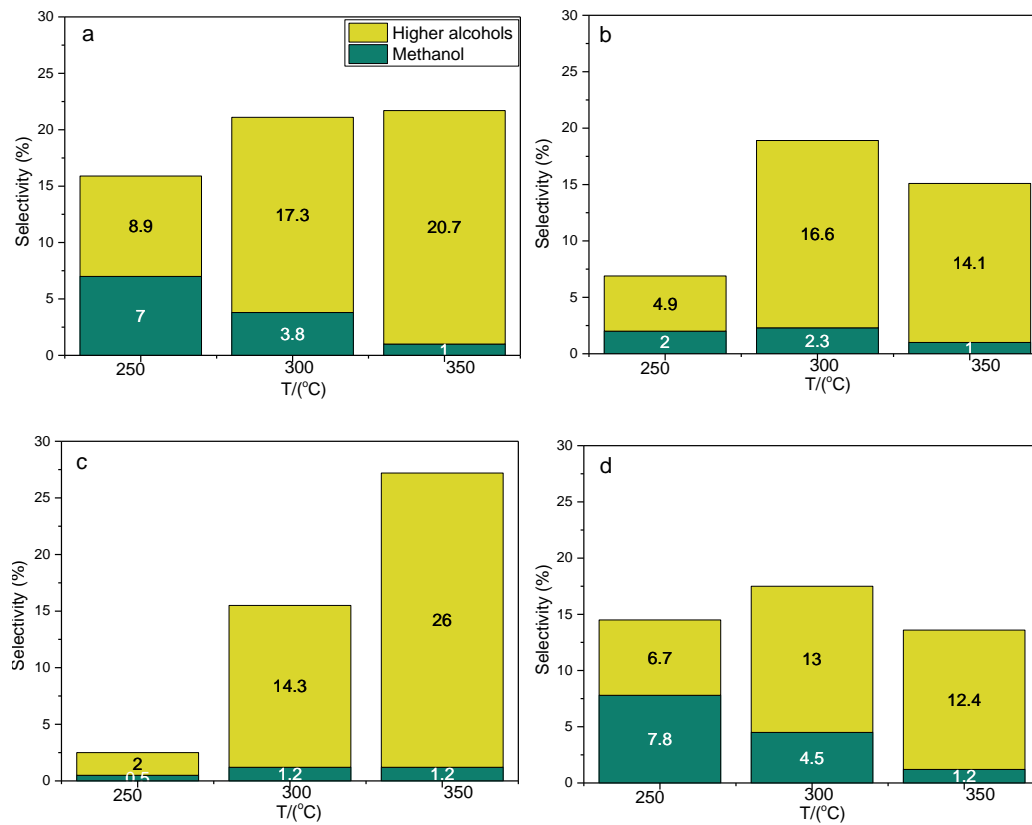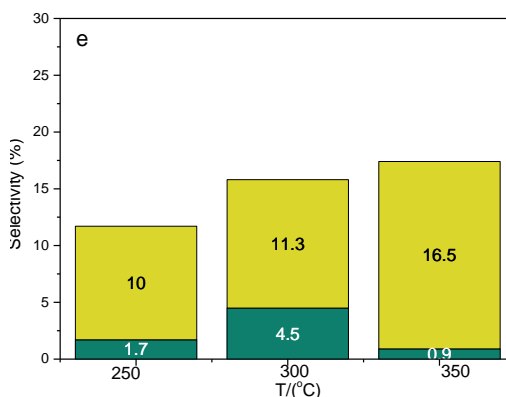
Figure 11 Les sélectivités des produits obtenus pour les catalyseurs a) 0,5K30CuFeCNTs, b) 1K30CuFeCNTs, c) 1,5K30CuFeCNTs, d) 1Na30CuFeCNTs, e) 1Cs30CuFeCNTs à 250 °C, 300 °C et 350 °C, 50 bar

Les conversions en H_2 et en CO_2 sont dans la Figure 10. Les sélectivités des produits obtenus pour les catalyseurs sont dans la

Figure 11.

1K30CuFeCNTs et 1Cs30CuFeCNT présentent une conversion de CO_2 similaire à 250 °C, environ 9,3% et à 300 °C, environ 21%. Néanmoins, à 350 °C, la conversion de CO_2 obtenue sur 1Cs30CuFeCNT est beaucoup plus élevée que sur 1K30CuFeCNT : 38,5% contre 26,3%, respectivement. 1Na30CuFeCNT a une conversion en CO_2 la plus faible par rapport à 1K30CuFeCNTs et 1Cs30CuFeCNT sur toute la gamme de la température de réaction.

Parmi les échantillons promus au potassium, 1K30CuFeCNT présente la plus forte conversion en CO_2 à 250°C. Mais lorsque la température est augmentée, l'activité de 0,5KCuFeCNT est largement meilleure que celle de 1K30CuFeCNTs et 1,5K30CuFeCNTs. La conversion en CO_2 atteint 42,5% à 350 °C, ce qui représente la conversion de CO_2 la plus élevée parmi tous les catalyseurs promus,

Pour H_2 conversions, par rapport à 1K30CuFeCNTs et 1Na30CuFeCNTs, 1Cs30CuFeCNT est plus élevées à 250 °C, 300 °C et 350 °C (6,9%, 24,2% et 47,8% respectivement). La conversion d' H_2 de 1K30CuFeCNT est un peu plus élevée que

celle de 1Na30CuFeCNT à 300 °C et 350 °C.

Pour une concentration de charge différente de K, 0,5K30CuFeCNT a montré une activité en H_2 plus élevée que celle de 1K30CuFeCNT et 1,5K30CuFeCNT, en particulier à haute température comme 300 °C et 350 °C (24,3% et 42,5% respectivement),

Pour la réaction à 250 °C, le matériau promu au césium 1Cs30CuFeCNTs montre les sélectivités et productivités en alcools supérieurs les plus élevées. Pour les catalyseurs au potassium, les sélectivités en alcools supérieurs ont diminué de 8,0% à 2,0% avec un taux de charge de K varié de 0,5% à 1,5% et la productivité en alcools supérieurs de 1,5K30CuFeCNT n'est que de 6,6 g · kg^{-1} · h^{-1}, ce qui est beaucoup plus faible que 30,1 g · kg^{-1} · h^{-1} dans le cas de 0,5K30CuFeCNTs,

A 300 °C, la sélectivité et la productivité en alcools supérieurs les plus élevées ont été obtenues dans la réaction du catalyseur 1K30CuFeCNT, 16,6% et 150,4 g · kg^{-1} · h^{-1} respectivement,

Avec une augmentation de la température de 300 °C à 350 °C, les sélectivités en alcools supérieurs augmentent dans le cas de 1Cs30CuFeCNT en tant que catalyseur, de 10,0% à 16,5%, et les productivités ont augmenté de 107,6 à 253,0 g · kg^{-1} · h^{-1}, Ceci est beaucoup plus élevé que pour 1Na30CuFeCNTs et 1K30CuFeCNT en tant que catalyseurs. 1,5K30CuFeCNTs présente la plus grande sélectivité en alcools supérieurs (26,0%) et 0,5K30CuFeCNTs présente une productivité en alcools supérieurs la plus élevée (370,7 g · kg^{-1} · h^{-1}) à 350 °C.

L'ajout de promoteurs alcalins peut affecter profondément la distribution des produits et peut ainsi augmenter la sélectivité et la productivité en alcools supérieurs de manière efficace. Les dopants peuvent soit agir comme les promoteurs électroniques, soit comme les promoteurs structuraux [5, 6]. L'addition d'alcalins peut favoriser la formation de carbure de fer, qui est une phase active essentielle pour l'activité d'une réaction Fischer-Tropsch, De plus, les alcalins peuvent modifier les propriétés de la surface et augmenter les sites basiques, comme cela a été montré

précédemment. Il peut également réduire la densité électronique des métaux de d-vacant tels que Fe par la donation des électrons, ainsi il peut favoriser l'adsorption dissociative de CO et diminuer l'adsorption de H_2 [5].

6 Conclusions

L'étude de spinelles de différentes compositions a montré que le spinelle $CuFe_2O_4$ est le précurseur de catalyseur le plus adapté à la synthèse d'alcools supérieurs à partir de CO_2/H_2,

Le dépôt de 30% de $CuFe_2O_4$ sur nanotubes de carbone permet d'augmenter les conversions d'H_2 et de CO_2 et la productivité en alcools supérieurs. L'utilisation de CNTs est avantageuse pour la synthèse des alcools supérieurs. L'utilisation de TUD-1 comme support est efficace pour orienter la réactivité vers la synthèse de méthanol,

L'addition de 0,5% de potassium promeut la croissance des chaînes carbonées et permet finalement d'atteindre une productivité en alcools supérieurs de 370,7 $g \cdot kg^{-1} \cdot h^{-1}$, Ce catalyseur promu fait partie des catalyseurs les plus efficaces parmi les plus systèmes référencés dans la littérature [7].

7 Références

[1] C.S. Song, Global challenges and strategies for control, conversion and utilization of CO_2 for sustainable development involving energy, catalysis, adsorption and chemical processing, Catalysis Today, 115 (2006) 2-32,

[2] P. Forzatti, E. Tronconi, I. Pasquon, Higher Alcohol Synthesis, Catal Rev, 33 (1991) 109-168,

[3] J.C. Vargas, S. Libs, A.C. Roger, A. Kiennemann, Study of Ce-Zr-Co fluorite-type oxide as catalysts for hydrogen production by steam reforming of bioethanol, Catalysis Today, 107-08 (2005) 417-425,

[4] J.J. Wang, J.R. Xie, Y.H,. Huang, B.H. Chen, G.D. Lin, H.B. Zhang, An efficient Ni-Mo-K sulfide catalyst doped with CNTs for conversion of syngas to ethanol and higher alcohols, Appl Catal A Gen, 468 (2013) 44-51,

[5] S. Saeidi, N.A.S. Amin, M.R. Rahimpour, Hydrogenation of CO_2 to value-added products-A review and potential future developments, J CO_2 Utilization, 5 (2014) 66-81,

[6] R.W. Dorner, D.R. Hardy, F.W. Williams, H.D. Willauer, Heterogeneous catalytic CO_2 conversion to value-added hydrocarbons, Energ Environ Sci, 3 (2010) 884-890,

[7] S.G. Li, H.J. Guo, C.R. Luo, H.R. Zhang, L. Xiong, X.D. Chen, L.L. Ma, Effect of Iron Promoter on Structure and Performance of K/Cu-Zn Catalyst for Higher Alcohols Synthesis from CO_2 Hydrogenation, Catalysis Letters, 143 (2013) 345-355.

Table of Contents

List of Tables

List of Figures

Chapter I
Introduction

I.1 The background

With the opening of the "Conference Of Parties 2015" at Paris (COP 21), the issue of climate change attached the world's attention again. The climate change, especially the global warming, caused a series of disasters and challenges, which include the desertification (one of the greatest environmental challenges of our times) [1] and floods in the small island countries, countries with low-lying coastal and so on.

"Greenhouse gases" means those gaseous constituents of the atmosphere, both natural and anthropogenic, that adsorb and reemit infrared radiations [2].The "Greenhouse gases" in Figure 12 include carbon dioxide (CO_2), methane (CH_4), nitrous oxide (N_2O), and fluorinated gases [3]. 76% of the greenhouse gas is carbon dioxide.The huge quantity of CO_2 in the atmosphere in Figure 1,which acts as a blanket, trapping heat and warming the planet, is the main cause of global warming. According to the Figure 12, 65% of CO_2 come from the burning and consumption of fossil fuels like coal, oil and natural gas and industrial processes and there are 11% of CO_2 which is casued by the forest and other land use. The cut down of forests cause carbon accumulates and overloads in the atmosphere. Until now fossil fuels still supply more than 85% of the current energy consumption worldwide, and contribute in similar proportions to the anthropogenic CO_2 emissions [4].
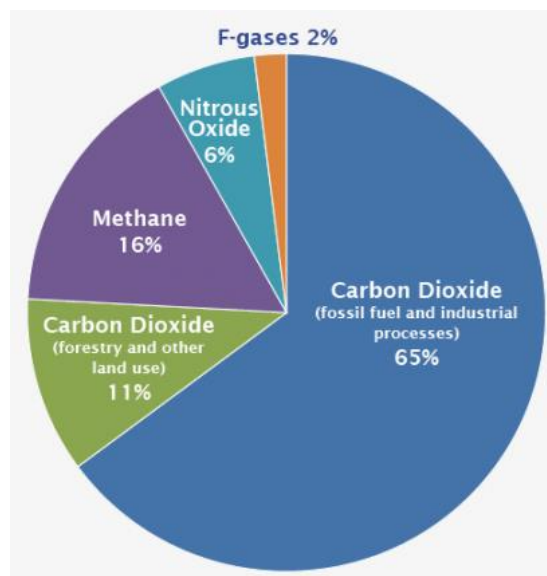
Figure 12 Global greenhouse gas emissions by gas based on global emissions from 2010 [3]

The adoption of the "Paris agreement" that was proposed in the COP 21 suggested that emissions need to be cut down to hold the increase in the global average temperature below 2 °C above preindustrial levels and that efforts have to be pursued to limit the temperature increase to 1.5 °C [5]. It is urgent to reduce the CO_2 emissions and to capture, store and reuse CO_2.

The capture of carbon dioxide from the flue gases of power plants which use coal, oil or gas as fuel and other industrial processes is mature technology [6]. The solvents like alkanolamine (MEA, MDEA..), NaOH, K_2CO_3 and piperazine (PZ) have been extensively studied to capture CO_2 [7]. Since there are still safety problems about the storage of CO_2 underground and ocean and no real economic driver, the utilization of captured CO_2 from power plants becomes more and more recognized worldwide.

Figure 13 shows what could be the place of the utilization of CO_2 in a virtuous cycle of CO_2 recycling. In the past years, CO_2 has been applied in various industries, e.g., soft drink, food, agro-chemistry, welding, foaming, fire-extinguishers, propellant, or as a fluid/solvent in various process like drying-cleaning, separation, water treatment, packaging, etc. The direct use of CO_2 to cultivate microalgae is interesting and extensively investigated because microalgae can not only consume CO_2 but are also feedstock to produce biofuels. The conversion of CO_2 to chemicals and energy products that are currently produced from fossil fuels is also promising due to the high potential market and promising benefits [8].
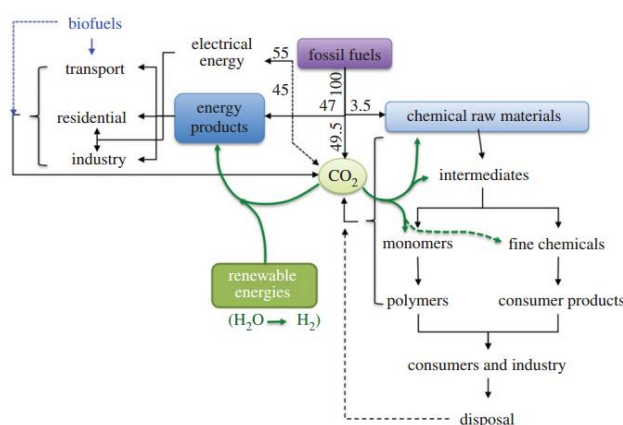
Figure 13 A model of CO_2 circular economy and its impact on the chemical and energy value chains [9]

I.2 The chemical utilization of CO_2

CO_2 is a clean carbon source for the chemical reactions, but CO_2 still has certain disadvantages as a chemical reactant because of the limit of thermodynamics.

The CO_2 hydrogenation has been studied for the synthesis of CO (Reverse Water Gas Shift Reaction), methane (methanation for Power-To-Gas process), hydrocarbons (Fischer-Tropsch-like processes), methanol, higher alcohols, and dimethyl ether. In our research, we will focus on the synthesis of higher alcohols from CO_2 hydrogenation. The higher alcohols (alcohols higher than methanol) can be used as alternative fuels and fuel additives, for example, they can be used as octane booster in automotive fuels instead of lead, aromatics (benzene and toluene) and tert-butyl methyl ether (MTBE) [10, 11]. More, the addition of higher alcohols can help reaching the rate of biofuels in gasoline to respect the 20-20-20 objectives [12].

Most of researchers study the higher alcohols synthesis from CO/H_2 mixtures or syngas $CO/CO_2/H_2$. There are only a few literatures and works about the synthesis of higher alcohols from CO_2 hydrogenation. This reaction was thought in two steps. CO_2 was first converted into CO, then higher alcohols were synthesized from CO hydrogenation.

The HAS reaction from CO hydrogenation needs two types of active sites in good cooperation (dual sites) and high active surface to lead to higher alcohols formation. A simple scheme in Figure 14 shows the works of dual active site. CO and H_2 can dissociate on M1 sites and form alkyl species, meanwhile, M2 site can adsorb CO in a non-dissociative way and insert it to the carbon chain to form the alcohols. The design of catalysts should keep a balance between the two active sites (M1 and M2), and maximize the synergism between propagation and oxygenation sites at the atomic scale [13].

4
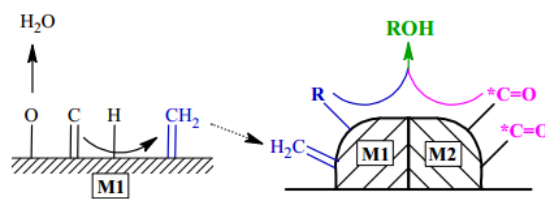
Figure 14 Schematic depiction of the dual site in HAS.
M1: chain growth center; M2: oxygenation center. [13]

I.3 The spinel structure of catalysts

A high selectivity for the linear higher alcohols needs that the catalyst surface owns CO dissociating sites in the vicinity of non-dissociating sites [14, 15]. Therefore, it is suggested that for all alcohol synthesis catalysts, it's better to distribute the metals in crystal structure (e.g., spinel, perovskite) of oxide precursors [16-18]. There are two main reasons: first, they may be very highly dispersed after being reduced under hydrogen atmosphere, and second, part of spinel or perovskites may remain after partial reduction, which can keep the suitable position of different metals and helps the dispersion of the reduced metals. The crystalline structure of spinel is shown in Figure 15. The spinel structure is formulated MM'_2X_4, where M^{+2} and M'^{3+} are tetrahedrally and octahedrally coordinated cations, respectively, and X is an anion (typically O or F). The structure is named from the mineral $MgAl_2O_4$, and oxide spinels have the general formula AB_2O_4 [19]. In inverse spinel, part or A^{+2} cations are located in octahedral sites and replaced by B^{3+} cations in tetrahedral sites.
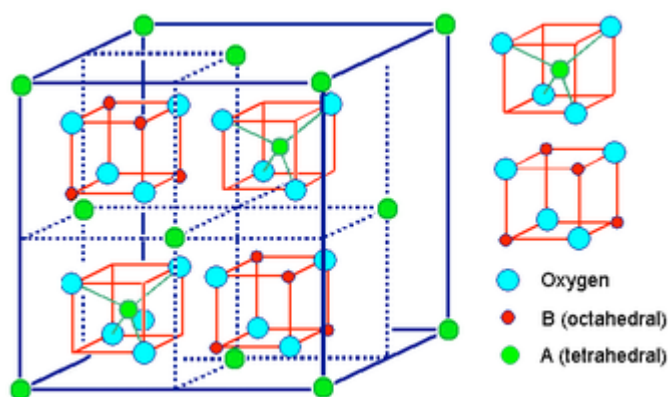
Figure 15 The structure of spinel AB_2O_4 [19]

I.4 The catalysts used for the higher alcohols synthesis

The catalysts for higher alcohols synthesis from the hydrogenation of CO or CO_2 can be broadly grouped into four categories:

a) Modified methanol synthesis catalysts (Cu-ZnO based catalysts)

b) Modified Fischer–Tropsch type catalysts

c) Rh-based catalysts

d) Modified Mo-based catalysts

I.4.1 Modified methanol synthesis catalysts

The CuZn-based catalysts have been well studied for the methanol synthesis. When there is alkali metal in the catalysts, small amount of higher alcohols can be observed, which led the researchers to study the effect of alkali on the synthesis of higher alcohols.

For Cu-based catalyst in CO hydrogenation reaction, the ability of promotion for synthesis of higher alcohols increases with the alkali atomic size, Li<Na<K<Rb<Cs. Two main effects were attributed to alkali doping: the first effect is the suppression of surface acidity, the second effect is to provide basic sites which are necessary for the C-C and C-O bond-forming reactions [20]. More, the optimum loading of alkali needs to be adjusted for each type of supports and preparation methods. Although the presence of alkali can increase the selectivity to higher alcohols at a given loading, further addition can block the Cu/ZnO active sites and thus decrease the reactivity [21]. Smith and Anderson [22] used K_2CO_3 to promote $Cu/ZnO/Al_2O_3$ and found that the maximum selectivity to higher alcohols was obtained at 0.5wt % K_2CO_3 loading. But on a Co/Cu/ZnO catalyst, the highest selectivity to higher alcohols was obtained at a 5 wt% K_2O (4.1 wt% K) promoter concentration [23].

Nevertheless, methanol was still the main product obtained on modified methanol-based catalysts, and the selectivity to higher alcohols was quite low, limited by the reaction mechanism [24]. According to the results of selectivities to alcohols at

a certain range of conditions with Cu-ZnO-0.5%K_2CO_3 as catalyst, J. Smith [25] proposed the mechanism presented in Figure 16 for the formation of higher alcohols from methanol. This mechanism assumed that the formation of higher alcohols occurred by condensation of two lower alcohols, with hydrogen loss at a α-position or β-position carbon atom, the latter being the fastest process. It was also assumed that hydrogen loss from methanol was slower than from a β-carbon and that secondary alcohols react by loss of the hydroxyl group only. According to the assumption, they estimated the alcohols products distribution, and the experimental results fit the estimated values well. This mechanism also explains the existence of branched chain alcohols such as isobutanol. The formation of C_{2+} linear alcohols during CO hydrogenation remains the least understood step and the rate of formation of ethanol appears to limit the overall rate of chain growth.
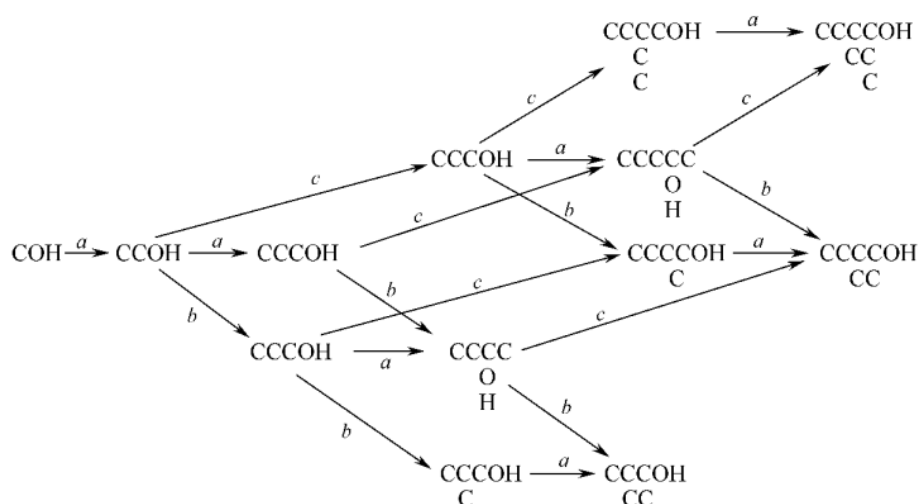
Figure 16 The higher alcohols carbon chain growth mechanism [26]

I.4.2 Modified Fischer-Tropsch catalysts.

Due to the high selectivity to alcohols and higher alcohols and their acceptable price, the Fischer-Tropsch (F-T) based catalysts have been widely studied, especially the Cu-Co based catalysts, the Cu-Fe based catalysts and the Cu-Co-Fe based catalysts. But for these modified F-T catalysts, there are still several problems which

need to be improved, such as the high selectivity to hydrocarbons, the low alcohols productivity, and the large variety of reaction products [26]. In order to obtain uniformly dispersed and well-designed bi- or multi-metallic catalysts and improve the performance of F-T based catalysts, suitable preparation methods, addition of promoters and appropriate supports are really important [27].

I.4.2.1 The mechanism of HAS from CO_2 hydrogenation

For F-T based catalysts, the synthesis of higher alcohols from CO_2 hydrogenation can be regarded as a combination of reversed water-gas shift (RWGS) reaction and then the formation of higher alcohols from gas mixture of H_2 + CO or H_2+CO+CO_2 [28, 29]. The most acceptable mechanism for the HAS reaction from CO hydrogenation is the CO insertion mechanism, which is proposed by Xiaoding [15]. The process is shown in Figure 17. The CO dissociation and carbon chain growth are similar to the Fischer-Tropsch reaction. The alkyl species ($C_nH_x^*$) were formed at the surface and the insertion of alkyl species determines the kinds of products. If the insertion CO through surface acyl species finishes the reaction followed by hydrogenation, the alcohols will be obtained. If the reaction is terminated by direct dehydrogenation or hydrogenation, the olefins or paraffins will be formed. So the formation of alcohols competes with hydrocarbons formation. According to the mechanism, the main products is linear alcohols and hydrocarbons [11].
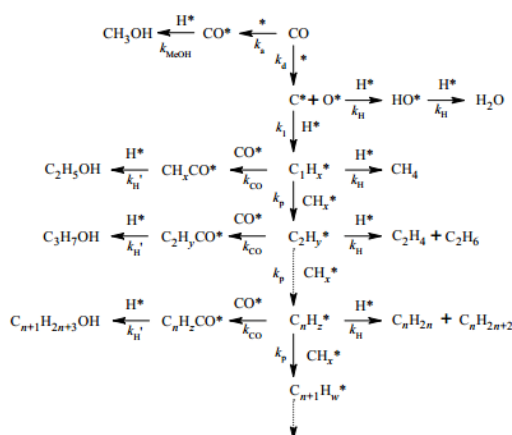
Figure 17 The CO insertion mechanism for higher alcohols synthesis [15]

The route for the synthesis of higher alcohols is clear according to the CO insertion mechanism. For the catalyst design, dual sites are necessary for the HAS reaction [15], and this is accepted by many researchers [30, 31]. For Cu-based catalysts, the main function of copper is enabling the dissociative chemisorption of hydrogen and the un-dissociative adsorption of CO. While Co adsorbs CO and dissociates it, then promotes the growth of C-C chain and hydrogenation [32]. For the function of iron, Riedel *et al*. [33] demonstrated that the steady states of hydrocarbons synthesis with iron oxides could be divided into five episodes of distinct kinetic regimes as illustrated in Figure 18. In episode I, the reactants adsorb on the catalyst surface and carbonization of the catalyst takes place dominantly. In episodes II and III, products from the RWGS reaction dominate during ongoing carbon deposition. In episode IV, the FT activity is beginning created, and the α-Fe was consumed during this step, meanwhile, Fe_5C_2 was formed. The FT activity develops up to the steady state and keeps the state in episode V. At the steady state, the composition of catalyst keeps changing, the Fe_2O_3 phases almost completely disappeared and a new "unknown" phase appeared, which maybe oxalic iron. FT activity begins after the formation of iron carbide (Fe_5C_2) by a reaction of iron with carbon from CO dissociation. For the iron-based catalysts, they are easily deactivated during the reaction because of the high amount of water in the reactor [34, 35].

It is important to add that Co is 3 times more active than Fe in F-T while its price is over 250 times more expensive [36].
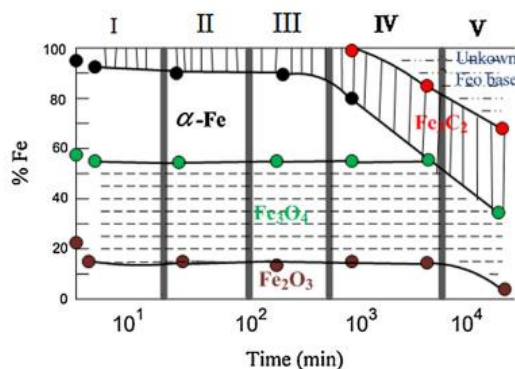
Figure 18 Iron-phase composition as a function of time during hydrocarbon synthesis on Fe/Al/Cu catalyst [33]

Figure 19 shows the mechanism of higher alcohols synthesis on Cu-based catalysts, CO is dissociated on the active F-T metals such as Fe, Co, then is hydrogenated to methylene species, which is the initiation of carbon chain and promote the formation of surface alkyl species. Meanwhile, CO molecularly adsorbs on Cu surface and inserts into the alkyl−metal bond to oxygenate the carbon chain. According to the mechanism in , no matter the CO molecule on Cu surface migrates to F-T metal surface to finish the reaction or the surface alkyl group on the F-T metals migrates to the Cu site to finish the reaction, the cooperation between the Cu and F-T metals is really important for HAS reaction . The catalysts should be designed at atomic level, in order to inhibit the side reaction.
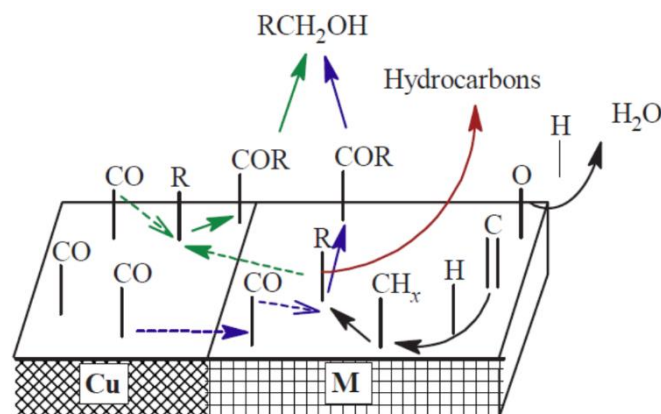
Figure 19 The reaction mechanism and network of higher alcohol synthesis from syngas over modified Cu-M based catalysts [13]

For Cu-Co based catalyst, Bailliard-Letournel *et al.* [37] studied the interaction of Co and Cu in the catalysts for higher alcohols synthesis from syngas. They found that the addition of copper to the Co-based catalysts can significantly decrease total activity, but increases the selectivity to higher alcohols and lighter alkanes. They proposed that the synthesis of higher alcohols needs a dual site: an alloy including copper and cobalt. The carbon chain was formed on cobalt and CO species adsorbed on copper atoms can provide terminal OH group. For this kind of Cu-Co based catalysts, Blanchard *et al.* [14]and Baker *et al.* [38] have proposed another type of dual site. Baker *et al.*[38] found that the bimetallic alloy of copper and cobalt was not

necessary for the synthesis of higher alcohols, but metallic cobalt and unreduced cobalt ions are the key components for higher alcohols synthesis. They thought the dual sites are metallic-oxide Co-pair (Co^0-$Co^{\delta+}$ pair). CO can dissociate on metallic Co and promote the propagation of carbon chain. Meanwhile, molecularly adsorbed CO on $Co^{\delta+}$ can insert into the carbon chain and finish the higher alcohols synthesis. This conclusion was confirmed by Spivey *et al.* [39] and other researchers [40]. The highly dispersed cobalt exhibited high activity for the formation of C_{2+} oxygenates from syngas [40]. The functions of copper are still not clear, it may only eliminate the synthesis of hydrocarbons on cobalt surface [38].

Compared to Cu-Co based catalysts, Cu-Fe based catalysts shows higher HAS activity and higher RWGS activity. It also shows high selectivity to higher alcohols and low selectivity to methane accounting for its capacity to grow carbon chain and direct the selectivity towards alcohols instead of hydrocarbons.

I.4.2.2 The supports

Supports can increase the surface area of active phase and act as a stabilizer to avoid sintering of the catalytically active particles during catalyst testing [41].

The most used supports are SiO_2, Al_2O_3 [42], ZrO_2, La_2O_3 [43], H-ZMS-5 [44], ZnO, activated carbon [45] and carbon nanotubes [46]. Both the textural properties and the chemical properties of the support can affect the performance of catalysts [27].

Ding et al. [47] recently found that the Cu-Fe catalyst supported on SiO_2 of bimodal porosity exhibited high catalytic activity and high selectivity to $C_{2+}OH$, due to the well dispersion of active metal sites and high diffusion efficiency of products inside the bimodal pore structure.

Al_2O_3 can hinder sintering and increase the dispersion of metal by the strong interaction between metal and support [48].

Z. Wang *et al.* [43] have studied the effect of ZrO_2, Al_2O_3 and La_2O_3 as supports of Co-Cu catalysts for higher alcohols synthesis. They found that the selectivity to

higher alcohols obtained on CuCo/La$_2$O$_3$ (34.9%) is far greater than either CuCo/Al$_2$O$_3$ (13.1%) or CuCo/ZrO$_2$ (17.8%). La$_2$O$_3$ appeared to be more reactive, and a higher reactivity is usually linked to stronger basicity [49]. According to the results of ammonia and pyridine adsorption the ranking of Lewis acidity is: CoO, CuO, CaO < Ni$_2$O$_3$ < MgO < ZrO$_2$ < Cr$_2$O$_3$ < ZnO < TiO$_2$ < Al$_2$O$_3$. The Lewis acidity of ZrO$_2$ is similar to that of La$_2$O$_3$ [49], but compared to the medium and strong basic sites of La$_2$O$_3$, there is only negligible amount of weak basic sites on the surface of ZrO$_2$ [50], so the surface basicity is really important for the higher alcohols synthesis.

The carbon nanotubes have been drawing increasing attention, because the carbon nanotubes exhibit unusual mechanical and thermal stability as well as electron conductivity [51], large surface area and excellent performance for adsorption and spillover of hydrogen [52]. The excellent H$_2$ adsorption ability can generate a surface micro-environment with a high concentration of H-species, thus increasing the rate of surface hydrogenation reactions in the HAS [53]. The carbon nanotubes can be used as support or promoter in the reaction.

I.4.2.3 The promoters

The promoters can either act as electronic promoters or as structural promoters, or possibly as both. Structural promoters can influence the dispersion of active sites by avoiding the formation of metal-support compounds, or preventing the agglomeration, which may improve the catalyst activity and stability and tends to yield higher conversion. Because the structural promoters only increase the quantity of active sites, so it will not increase the products selectivity [36].

The electronic promoters may donate or withdraw electron density near the Fermi level in the valence band of the catalyst, resulting in a modification of the local electron density around the surface and thus modifying the active site. Electronic promoters usually not only increase conversion levels, but also impact the product selectivity [41].

The most used promoters are the alkalis metals, which are proven known to

increase the selectivity to higher alcohols. As for alkali in the modified methanol synthesis catalysts, the optimum degree of promotion strongly depends on the type of promoter, concentration and catalyst support [20]. In Fischer–Tropsch synthesis, the relative activity of catalysts containing an equal atomic amount of alkali promoters increases in the order Li<Na($\approx$Cs)<K<Rb [54]. An optimum addition of alkali depends on the property of the supports. The acidic supports (e.g. silica, alumina) require higher amounts of promoters to obtain the desired selectivity, but too much promoters will block the active sites and thus decrease the reactivity. Tien-Thao et al. found that the optimum alkali promoters was in the range 0.1-0.3 wt% for Co-Cu-based perovskites catalysts [54]. The addition of K has been demonstrated to increase CO_2 conversion [55, 56] and decrease CH_4 selectivity. K can increase the chemisorption of CO_2, then enhance the activity for CO formation [57]. It can also change the products distribution and increase alkene/alkane ratio almost 4-fold [55, 58].

Apart from alkalis, there are many metals such as Mn, Pb, Ru, which were used as dopants. Mn has been reported to act as a structural promoter and electronic promoter, and to increase the catalyst's surface basicity [59]. It can also suppress the formation of CH_4 [55]. The dissociative activation of H_2 is more difficult to achieve than the activation of CO [60]. The addition of platinum group metals such as Pb, Ru can efficiently activate H_2 at moderate conditions, so Pb and Ru are often used as promoter for high alcohols synthesis.

I.4.3 Rh-based catalysts

I.4.3.1 CO hydrogenation

By far the most widely studied catalysts for the hydrogenation of CO to oxygenates are based on Rh. In the periodic table, Rh occupies an interesting position between the Fischer-Tropsch metals (e.g., Fe and Co) which works at the dissociation of CO or CO_2 to form higher hydrocarbons and those metals which do not dissociate

CO and produce methanol (e.g., Pd, Pt and Ir) [20]. So suitable supported Rh catalyst particles could simultaneously adsorb CO in both molecular and dissociated states [61]. Rh-based catalysts are usually used under mild conditions [62]. Supported Rh is wildly used to produce two-carbon oxygen-containing compounds such as acetic acid, acetaldehyde, and ethanol. The chemical efficiency is as high as 50%, and there is also lots of unwanted by-products like methane [63].

The activity of Rh-based catalysts strongly depends on the promoters. A variety of promoters have been used in the higher alcohols synthesis reactions, which includes the transition metal oxides (Co, Fe [64, 65]), lanthanides (La [66], Ce [67]), alkalis (Li [68, 69],K,Cs), noble metals (Ag [70]), Mn [71] and vanadium have been studied and found to exhibit significant enhancement of the ethanol yield. Mo *et al.* [70] found that La enhanced total CO adsorption. The addition of V can increase desorption rate and reactivity of the adsorbed CO species, so V can enhance CO dissociation and chain growth [66]. The doubly promoted Rh-La/V/SiO$_2$ catalyst showed only moderate CO adsorption. The addition of Zn or Cu as promoters significantly reduced the desorption rate and reactivity of the adsorbed CO species on Rh/SiO$_2$, leading apparently to a much reduced activity for CO hydrogenation. The addition of Fe can enhance the rate of hydrogenation of acetaldehyde [72] and stabilized the linear carbonyl and gem-dicarbonyl species [64]. Many researchers [68, 69, 73] have found that the alkalis doping of Rh can increase the formation of C$_2$ oxygenates at the expense of C$_1$ species, which may be attributed to the change of electron density of surface Rh, causing a change in the surface population of CO species. There are more bridged CO species than liner CO species, these stable bridged CO species may suppress the active sites for hydrogenation [74]. After testing a series of alkali promoters on Rh/TiO$_2$ catalysts, Chuang *et al.* [73] found that the ability to enhance selectivity to oxygenates increased in the order: unprompted < Li < K = Cs.

In addition to the promoters, the supports are also important to increase the performance of catalysts and many kinds of supports have been well investigated. The structural properties and nature of the supports can affect the particle size and

distribution of the active metals and unique interactions between the active metal components and supports, which influence the catalytic activities for the reaction [75]. The most used supports are SiO_2, Al_2O_3 [65], TiO_2 [76], ZrO_2, V_2O_3, CeO_x, MgO and carbon nanotubes.

I.4.3.2 CO_2 hydrogenation

Fisher *et al.* [77] have investigated the similarities and differences between the CO and CO_2 hydrogenation reactions on a Rh-SiO_2 catalyst. They found that the surface CO species (linearly and bridged-CO) are the same. The only differences are that CO_2 needs first to dissociate and that the rate of methane formation is higher starting from CO_2.

I.4.3.3 The mechanism analysis

The mechanism of higher alcohols synthesis on the Rh-based catalyst in Figure 20 is similar to the one proposed for Fischer-Tropsch reaction [20].
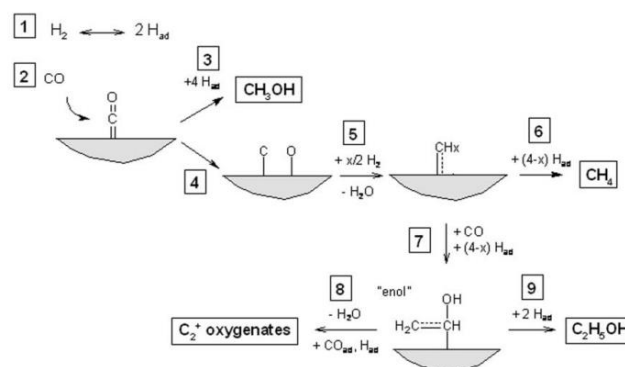
Figure 20 A simplified sequence for ethanol formation by CO hydrogenation
on Rh-based catalysts[20]

For CO_2 hydrogenation, the reaction scheme in Figure 20 would be modified only to take into account the formation of surface C and O from CO_2 rather than from CO, with the remaining steps being the same [20].

However, the application and commercialization of noble metal-based catalysts using Rh based catalysts are limited due to the high cost for large scale utilization.

I.4.4 Modified Mo-based catalysts (Mo$_2$C-based catalysts and Mo$_2$S-based catalysts)

MoS$_2$-based catalysts have been proven to have excellent sulfur resistance and high resistance to deactivation by coking [78]. It also owns good selectivity to ethanol and/or higher alcohols. The harsh reaction conditions of high pressure (ca. 10-12 MPa) limited the industrial applications [62].

Non-promoted MoS$_2$ catalysts display selectivity to methane and other short hydrocarbons [79]. For the Mo-based catalysts, the promoters are necessary in order to obtain higher alcohols. The group VIII metals and alkali are often added to the catalysts. In 1980s, researchers in Dow Chemicals [80] and Union Carbide first discovered that alkali-doped MoS$_2$ (ADM) catalyst could be used to produce alcohols from syngas [81]. For molybdenum carbide, when K$_2$CO$_3$ was added, the selectivity to linear C$_1$-C$_7$ alcohols was greatly enhanced [82]. Some researchers also found that the heavier Cs, Rb, K elements are very much more efficient compared to the lighter Na, Li [83]. Sachtler *et al.* [84] suggested that alkali can affect the kinetics and energetics of the adsorption of hydrogen, carbon monoxide and other reactants on the surface of catalysts, thereby affecting their relative surface coverage during reaction. More specifically, alkali can block the sites on MoS$_2$ surface, so reduce the activity of hydrogen on the MoS$_2$ surface, but increase the non-dissociative adsorption of CO [85].

Group VIII promoters such as nickel or cobalt are often added to the catalyst in order to increase the selectivity to higher alcohols [86]. The highly dispersed Ni can form Ni-Mo-S species, which can promote the electron donation from Ni to Mo, and decrease the Mo-S bond strength to an optimum range, so it can significantly increase the activity of the catalyst [87] and works for the CO insertion [88]. Highly homogeneous modified MoS$_2$-based catalysts with good cooperation of promoter and sulfides were expected to lead to high performance for higher alcohols synthesis (HAS) [89]. Co can also form Co-Mo-S structure [90] and Co-promoted alkali-modified molybdenum sulfide catalysts showed better activity and selectivity to

higher alcohols compared to that of Ni. Because the addition of Co to alkali-modified MoS_2 catalysts enhanced the C_1 to C_2 homologation step, ethanol is the dominant product [90].

For Mo_2C-based catalyst, the dual sites are low valence Mo (Mo-I, $Mo^{(0-2)+}$) and high valence Mo (Mo-II, $Mo^{(4-5)+}$). Low valence Mo works for the CO dissociation and hydrogenation and promote the carbon chain growth. Meanwhile, high valence can associatively adsorb CO and insert into the carbon chain [30].

I.5 The effect of operating conditions on HAS from CO_2/H_2

I.5.1 The temperature

According to the mechanism of HAS, the reaction was a combination of RWGS reaction and subsequent formation of higher alcohols from $H_2/CO/CO_2$ mixture gas. So the conditions should be convenient for both reactions. The RWGS reaction is endothermic and high temperature are beneficial for the conversion of CO_2 and the formation of CO. The hydrogenation of CO/CO_2 to higher alcohols is an exothermic reaction [91]. So suitable reaction temperature or dissipation of the heat in time is important for obtain higher yield of alcohols. Nieskens *et al.* [92] found that the alcohols selectivities is lower and the hydrocarbons selectivity is higher at 340 °C than at310 °C, but higher temperature are beneficial for carbon chain growth. In most literatures the temperature range 250 °C-350 °C was used for HAS reaction [93, 94].

I.5.2 The space velocity

The increase of the reactant feed flow will short the contact time, which will lead to a gradual decline in CO_2 conversion. This may also affect the distribution of alcohols [95]. The yield of alcohols and the selectivity of by-products, including hydrocarbons and dimethyl ether, increased with the increase of the space velocity.

The CO_2 conversion will be higher if the flow rate is slow, but there may be some hot points in the catalysts layer. According to the literature, the best GHSV (Gas

Hourly Space Velocity) is between 5000 h^{-1} and 10000 h^{-1} (STP).

I.5.3 The ratio of CO_2/H_2

The typical ratio for H_2/CO to higher alcohols is 2, but it is different for H_2/CO_2. When the H_2/CO_2 feed ratio is 1, the main product is CO, and the rates of alcohols and alkanes are relative low. When the ratio is 3, the CO_2 conversion is higher, the CO selectivity is lower, and the alcohols and alkanes selectivities are higher compared to feeding a 1/1 mixture of H_2/CO_2 [92].

$$nCO_2 + 3nH_2 \rightarrow C_nH_{2n+1}OH + (2n-1)H_2O \qquad (1\text{-}1)$$
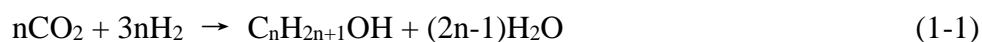
For the alcohol formation reactions, this ratio will always be 3/1, regardless of the length of the alcohol carbon chain. So the ratio for H_2/CO_2 to higher alcohols is better around 3.

I.6 Conclusions

Four kinds of catalysts for HAS reaction are compared in this introduction. Modified methanol synthesis catalyst still works for the synthesis of methanol, there are only a little of higher alcohols. For Rh-based catalyst, the high cost limits the large scale utilization. The harsh reaction conditions of high pressure will also limit the utilization of Mo-based catalyst. The Fischer-Tropsch based catalysts are thus the most promising catalysts, because of the availability of the materials and high activity.

From the analysis of mechanism for HAS, dual sites are the key point for the synthesis of higher alcohols. The design of catalysts should concern the atomic scale.

I.7 Research objectives

In this thesis, we try to develop a catalyst that is capable to produce higher

alcohols with high selectivities and productivities from CO_2 hydrogenation.

The methodology of development will follow the three aspects presented below:

1. F-T based catalysts will be used and Fe, Cu and Co will be chosen as active metals which will be initially atomically mixed in a perovskite.

2. Suitable supports (TUD-1 and carbon nanotubes) will be used to increase the surface area and increase reactivity.

3. Alkalis (Na, K, Cs) will be used as promoters. The quantity of potassium will be optimized to improve the synthesis of higher alcohols.

I.8 Literatures

[1] Climate change and desertification, UNCCD thematic fact sheet series No.1.

[2] United Nations Framework Convention On Climate Change 1992.

[3] Kyoto protocol to the united nations framework convention on climate change 1998.

[4] M.M.F. Hasan, E.L. First, F. Boukouvala, C.A. Floudas, A multi-scale framework for CO_2 capture, utilization, and sequestration: CCUS and CCUM, Comput Chem Eng, 81 (2015) 2-21.

[5] C.o.t. Parties, Adoption of the paris agreement, (2015).

[6] K.M.K. Yu, I. Curcic, J. Gabriel, S.C.E. Tsang, Recent Advances in CO_2 Capture and Utilization, Chemsuschem, 1 (2008) 893-899.

[7] M. Wang, A.S. Joel, C. Ramshaw, D. Eimer, N.M. Musa, Process intensification for post-combustion CO_2 capture with chemical adsorption: A critical review, Applied Energy, 158 (2015) 275-291.

[8] C.H. Huang, C.S. Tan, A Review: CO_2 Utilization, Aerosol Air Qual Res, 14 (2014) 480-499.

[9] C. Ampelli, S. Perathoner, G. Centi, CO_2 utilization: an enabling element to move to a resource- and energy-efficient chemical and fuel production, Philosophical transactions. Series A, Mathematical, physical, and engineering sciences, 373 (2015).

[10] V.R. Surisetty, A.K. Dalai, J. Kozinski, Alcohols as alternative fuels: An overview, Appl Catal A Gen, 404 (2011) 1-11.

[11] Y. Lu, Catalytic conversion of syngas to higher alcohols over Cu-Fe based catalysts, in, MISSISSIPPI STATE UNIVERSITY, 2014.

[12] E.R.E. Network, Directorate general for internal policies. Policy department. A: Economic and scientific policy industry, research and energy European parliament, (2012).

[13] K. Xiao, Z.H. Bao, X.Z. Qi, X.X. Wang, L.S. Zhong, K.G. Fang, M.G. Lin, Y.H. Sun, Advances in bifunctional catalysis for higher alcohol synthesis from syngas, Chinese Journal of Catalysis, 34 (2013) 116-129.

[14] M. Blanchard, H. Derule, P. Canesson, Cobalt Catalysts for the Production of Alcohols in the FT Synthesis, Catalysis Letters, 2 (1989) 319-322.

[15] X. Xiaoding, E. Doesburg, J. Scholten, Synthesis of higher alcohols from syngas: recently patented catalysts and tentative ideas on the mechanism, Catalysis today, 2 (1987) 125-170.

[16] X.D. Xu, J.J.F. Scholten, D. Mausbeck, Stability of Copper Cobalt Catalysts for the Synthesis of Higher Alcohols from Syngas, Appl Catal A Gen, 82 (1992) 91-109.

[17] L. Bedel, A.C. Roger, C. Estournes, A. Kiennemann, Co^0 from partial reduction of $La(Co,Fe)O_{-3}$ perovskites for Fischer-Tropsch synthesis, Catalysis Today, 85 (2003) 207-218.

[18] N. Tien-Thao, M.H. Zahedi-Niaki, H. Alamdari, S. Kaliaguine, Conversion of syngas to higher alcohols over nanosized $LaCo_{0.7}Cu_{0.3}O_3$ perovskite precursors, Appl Catal A Gen, 326 (2007) 152-163.

[19] ChemWiKi, http://chemwiki.ucdavis.edu/Textbook_Maps/Inorganic_Chemistry_Textbook_Maps/ Map%3A_Inorganic_Chemistry_(Wikibook)/Chapter_08%3A_Ionic_and_Covalent_ Solids_-_Structures/8.6%3A_Spinel,_perovskite,_and_rutile_structures.

[20] J.J. Spivey, A. Egbebi, Heterogeneous catalytic synthesis of ethanol from biomass-derived syngas, Chemical Society reviews, 36 (2007) 1514-1528.

[21] J.C. Slaa, J.G. Vanommen, J.R.H. Ross, The Synthesis of Higher Alcohols Using Modified $Cu/Zno/Al_2o_3$ Catalysts, Catalysis Today, 15 (1992) 129-148.

[22] K.J. Smith, R.B. Anderson, The Higher Alcohol Synthesis over Promoted Cu/Zno Catalysts, Can J Chem Eng, 61 (1983) 40-45.

[23] I. Boz, Higher alcohol synthesis over a K-promoted $Co_2O_3/CuO/ZnO/Al_2O_3$ catalyst, Catalysis Letters, 87 (2003) 187-194.

[24] J. Sá, Fuel production with heterogeneous catalysis, CRC Press, 2014.

[25] K.J. Smith, R.B. Anderson, A Chain Growth Scheme for the Higher Alcohols Synthesis, Journal of Catalysis, 85 (1984) 428-436.

[26] W. Gao, Y.F. Zhao, J.M. Liu, Q.W. Huang, S. He, C.M. Li, J.W. Zhao, M. Wei, Catalytic conversion of syngas to mixed alcohols over CuFe-based catalysts derived

from layered double hydroxides, Catalysis Science & Technology, 3 (2013) 1324-1332.

[27] R.L. Lu, D.S. Mao, J. Yu, Q.S. Guo, Enhanced activity of Cu-Fe/SiO$_2$ catalyst for CO hydrogenation to higher alcohols by pretreating the support with ammonia, Journal of Industrial and Engineering Chemistry, 25 (2015) 338-343.

[28] S. Li, H. Guo, C. Luo, H. Zhang, L. Xiong, X. Chen, L. Ma, Effect of Iron Promoter on Structure and Performance of K/Cu-Zn Catalyst for Higher Alcohols Synthesis from CO$_2$ Hydrogenation, Catalysis Letters, 143 (2013) 345-355.

[29] G. Centi, S. Perathoner, Opportunities and prospects in the chemical recycling of carbon dioxide to fuels, Catalysis Today, 148 (2009) 191-205.

[30] K.G. Fang, D.B. Li, M.G. Lin, M.L. Xiang, W. Wei, Y.H. Sun, A short review of heterogeneous catalytic process for mixed alcohols synthesis via syngas, Catalysis Today, 147 (2009) 133-138.

[31] Y.W. Lu, B.B. Cao, F. Yu, J. Liu, Z.H. Bao, J.S. Gao, High Selectivity Higher Alcohols Synthesis from Syngas over Three-Dimensionally Ordered Macroporous Cu-Fe Catalysts, Chemcatchem, 6 (2014) 473-478.

[32] S.Y. Deng, W. Chu, H.Y. Xu, L.M. Shi, L.H. Huang, Effects of impregnation sequence on the microstructure and performances of Cu-Co based catalysts for the synthesis of higher alcohols, Journal of Natural Gas Chemistry, 17 (2008) 369-373.

[33] T. Riedel, H. Schulz, G. Schaub, K.W. Jun, J.S. Hwang, K.W. Lee, Fischer-Tropsch on iron with H$_2$/CO and H$_2$/CO$_2$ as synthesis gases: the episodes of formation of the Fischer-Tropsch regime and construction of the catalyst, Top Catal, 26 (2003) 41-54.

[34] S. Saeidi, N.A.S. Amin, M.R. Rahimpour, Hydrogenation of CO$_2$ to value-added products—A review and potential future developments, Journal of CO$_2$ Utilization, 5 (2014) 66-81.

[35] W. Wang, S. Wang, X. Ma, J. Gong, Recent advances in catalytic hydrogenation of carbon dioxide, Chemical Society reviews, 40 (2011) 3703-3727.

[36] B.M.w. Fernando Morales, Promotion effects in Co-based Fischer-Tropsch catalysis, The royal society of chemistry, 19 (2006) 1-40.

[37] R.M. Bailliardletournel, A.J.G. Cobo, C. Mirodatos, M. Primet, J.A. Dalmon, About the Nature of the Co-Cu Interaction in Co-Based Catalysts for Higher Alcohols Synthesis, Catalysis Letters, 2 (1989) 149-156.

[38] J.E. Baker, R. Burch, S.J. Hibble, P.K. Loader, Properties of Silica-Supported Cu Co Bimetallic Catalysts in the Synthesis of Higher Alcohols, Appl Catal, 65 (1990) 281-292.

[39] M.L. Smith, N. Kumar, J.J. Spivey, CO Adsorption Behavior of Cu/SiO_2, Co/SiO_2, and $CuCo/SiO_2$ Catalysts Studied by in Situ DRIFTS, J Phys Chem C, 116 (2012) 7931-7939.

[40] T. Matsuzaki, T. Hanaoka, K. Takeuchi, H. Arakawa, Y. Sugi, K.M. Wei, T.L. Dong, M. Reinikainen, Oxygenates from syngas over highly dispersed cobalt catalysts, Catalysis Today, 36 (1997) 311-324.

[41] R.W. Dorner, D.R. Hardy, F.W. Williams, H.D. Willauer, Heterogeneous catalytic CO_2 conversion to value-added hydrocarbons, Energ Environ Sci, 3 (2010) 884-890.

[42] A. Le Valant, A. Garron, N. Bion, D. Duprez, F. Epron, Effect of higher alcohols on the performances of a $1\%Rh/MgAl_2O_4/Al_2O_3$ catalyst for hydrogen production by crude bioethanol steam reforming, International Journal of Hydrogen Energy, 36 (2011) 311-318.

[43] Z. Wang, J.J. Spivey, Effect of ZrO_2, Al_2O_3 and La_2O_3 on cobalt-copper catalysts for higher alcohols synthesis, Appl Catal A Gen, 507 (2015) 75-81.

[44] A.C. Gujar, V.K. Guda, M. Nolan, Q.G. Yan, H. Toghiani, M.G. White, Reactions of methanol and higher alcohols over H-ZSM-5, Appl Catal A Gen, 363 (2009) 115-121.

[45] G.P. Jiao, Y.J. Ding, H.J. Zhu, X.M. Li, W.D. Dong, J.W. Li, Y. Lu, Effect of the Reduction Temperature of Co-La-Zr/AC on the Synthesis of Higher Alcohols from Syngas, Chinese Journal of Catalysis, 30 (2009) 92-94.

[46] T. Han, W. Huang, X.D. Wang, Y. Tang, S.Q. Liu, X.X. You, Study of Ce-Cu-Co/CNTs Catalysts for the Synthesis of Higher Alcohols and Ethanol from Syngas, Acta Phys-Chim Sin, 30 (2014) 2127-2133.

[47] M. Ding, J. Liu, Q. Zhang, N. Tsubaki, T. Wang, L. Ma, Preparation of

copper-iron bimodal pore catalyst and its performance for higher alcohols synthesis, Catalysis Communications, 28 (2012) 138-142.

[48] K.W. Jun, S.J. Lee, H. Kim, M.J. Choi, K.W. Lee, Support effects of the promoted and unpromoted iron catalysts in CO_2 hydrogenation, Advances in Chemical Conversions for Mitigating Carbon Dioxide, 114 (1998) 345-350.

[49] O.V. Manoilova, S.G. Podkolzin, B. Tope, J. Lercher, E.E. Stangland, J.M. Goupil, B.M. Weckhuysen, Surface acidity and basicity of La_2O_3, LaOCl, and $LaCl_3$ characterized by IR spectroscopy, TPD, and DFT calculations, Journal of Physical Chemistry B, 108 (2004) 15770-15781.

[50] S. Kus, M. Otremba, M. Taniewski, The catalytic performance in oxidative coupling of methane and the surface basicity of La_2O_3, Nd_2O_3, ZrO_2 and Nb_2O_5, Fuel, 82 (2003) 1331-1338.

[51] X.L. Pan, Z.L. Fan, W. Chen, Y.J. Ding, H.Y. Luo, X.H. Bao, Enhanced ethanol production inside carbon-nanotube reactors containing catalytic particles, Nat Mater, 6 (2007) 507-511.

[52] H.B. Zhang, X. Dong, G.D. Lin, X.L. Liang, H.Y. Li, Carbon nanotube-promoted Co-Cu catalyst for highly efficient synthesis of higher alcohols from syngas, Chemical Communications, (2005) 5094-5096.

[53] X. Dong, X.L. Liang, H.Y. Li, G.D. Lin, P. Zhang, H.B. Zhang, Preparation and characterization of carbon nanotube-promoted Co-Cu catalyst for higher alcohol synthesis from syngas, Catalysis Today, 147 (2009) 158-165.

[54] N. Tien-Thao, M.H. Zahedi-Niaki, H. Alamdari, S. Kaliaguine, Effect of alkali additives over nanocrystalline Co-Cu-based perovskites as catalysts for higher-alcohol synthesis, Journal of Catalysis, 245 (2007) 348-357.

[55] R.W. Dorner, D.R. Hardy, F.W. Williams, H.D. Willauer, K and Mn doped iron-based CO_2 hydrogenation catalysts: Detection of $KAlH_4$ as part of the catalyst's active phase, Appl Catal A Gen, 373 (2010) 112-121.

[56] L.Y. Xu, Q.X. Wang, D.B. Liang, X. Wang, L.W. Lin, W. Cui, Y.D. Xu, The promotions of MnO and K_2O to Fe/silicalite-2 catalyst for the production of light alkenes from CO_2 hydrogenation, Appl Catal A Gen, 173 (1998) 19-25.

[57] P.H. Choi, K.W. Jun, S.J. Lee, M.J. Choi, K.W. Lee, Hydrogenation of carbon dioxide over alumina supported Fe-K catalysts, Catalysis Letters, 40 (1996) 115-118.

[58] D.L. King, J.B. Peri, An Infrared Study of Nitric-Oxide Chemisorption on Alumina-Supported Iron and Alkalized Iron Fischer-Tropsch Catalysts, Journal of Catalysis, 79 (1983) 164-175.

[59] T.Z. Li, Y. Yang, C.H. Zhang, X. An, H.J. Wan, Z.C. Tao, H.W. Xiang, Y.W. Li, F. Yi, B.F. Xu, Effect of manganese on an iron-based Fischer-Tropsch synthesis catalyst prepared from ferrous sulfate, Fuel, 86 (2007) 921-928.

[60] X.M. Yang, X.F. Zhu, R.R. Hou, L.P. Zhou, Y.L. Su, The promotion effects of Pd on Fe-Cu-Co based catalyst for higher alcohols synthesis, Fuel Processing Technology, 92 (2011) 1876-1880.

[61] D.H. Mei, R. Rousseau, S.M. Kathmann, V.A. Glezakou, M.H. Engelhard, W.L. Jiang, C.M. Wang, M.A. Gerber, J.F. White, D.J. Stevens, Ethanol synthesis from syngas over Rh-based/SiO_2 catalysts: A combined experimental and theoretical modeling study, Journal of Catalysis, 271 (2010) 325-342.

[62] W. Mao, J.J. Su, Z.P. Zhang, X.C. Xu, W.W. Dai, D.L. Fu, J. Xu, X.G. Zhou, Y.F. Han, Kinetics study of C_{2+} oxygenates synthesis from syngas over Rh-MnO_x/SiO_2 catalysts, Chem Eng Sci, 135 (2015) 312-322.

[63] M.M. Bhasin, W.J. Bartley, P.C. Ellgen, T.P. Wilson, Synthesis Gas Conversion over Supported Rhodium and Rhodium-Iron Catalysts, Journal of Catalysis, 54 (1978) 120-128.

[64] W.G. Liu, S. Wang, T.J. Sun, S.D. Wang, The Promoting Effect of Fe Doping on Rh/CeO_2 for the Ethanol Synthesis, Catalysis Letters, 145 (2015) 1741-1749.

[65] W.M. Chen, Y.J. Ding, X.G. Song, H.J. Zhu, L. Yan, T. Wang, Performance of Promoted Rh-Fe/Al_2O_3 Catalysts for CO Hydrogenation to Ethanol, Chinese Journal of Catalysis, 33 (2012) 1007-1013.

[66] X.H. Mo, J. Gao, N. Umnajkaseam, J.G. Goodwin, La, V, and Fe promotion of Rh/SiO_2 for CO hydrogenation: Effect on adsorption and reaction, Journal of Catalysis, 267 (2009) 167-176.

[67] C.M. Li, J.M. Liu, W. Gao, Y.F. Zhao, M. Wei, Ce-Promoted Rh/TiO_2

Heterogeneous Catalysts Towards Ethanol Production from Syngas, Catalysis Letters, 143 (2013) 1247-1254.

[68] A. Egbebi, V. Schwartz, S.H. Overbury, J.J. Spivey, Effect of Li Promoter on titania-supported Rh catalyst for ethanol formation from CO hydrogenation, Catalysis Today, 149 (2010) 91-97.

[69] J.W. Li, Y.J. Ding, R.H. Lin, L.F. Gong, X.E. Song, W.M. Chen, T. Wang, H.Y. Luo, Effect of Li Promoter on Catalytic Performance of Rh-Mn/SiO$_2$ for CO Hydrogenation to C$_{2+}$ Oxygenates, Chinese Journal of Catalysis, 31 (2010) 365-369.

[70] X.H. Mo, J. Gao, J.G. Goodwin, Role of promoters on Rh/SiO$_2$ in CO hydrogenation: A comparison using DRIFTS, Catalysis Today, 147 (2009) 139-149.

[71] S.R. Wang, W.W. Guo, H.X. Wang, L.J. Zhu, K.Z. Qiu, Influence of Mn Promotion on CO Hydrogenation over Rh/CNTs Catalyst, Catalysis Letters, 144 (2014) 1305-1312.

[72] R. Burch, M.J. Hayes, The preparation and characterisation of Fe-promoted Al$_2$O$_3$-supported Rh catalysts for the selective production of ethanol from syngas, Journal of Catalysis, 165 (1997) 249-261.

[73] S.C. Chuang, J.G. Goodwin, I. Wender, The Effect of Alkali Promotion on Co Hydrogenation over Rh/TiO$_2$, Journal of Catalysis, 95 (1985) 435-446.

[74] H. Kusama, K. Okabe, K. Sayama, H. Arakawa, CO$_2$ hydrogenation to ethanol over promoted Rh/SiO$_2$ catalysts, Catalysis Today, 28 (1996) 261-266.

[75] F. Li, H.F. Ma, H.T. Zhang, W.Y. Ying, D.Y. Fang, Ethanol synthesis from syngas on Mn- and Fe-promoted Rh/gamma-Al$_2$O$_3$, Cr Chim, 17 (2014) 1109-1115.

[76] L.P. Han, D.S. Mao, J. Yu, Q.S. Guo, G.Z. Lu, C$_{-2}$-oxygenates synthesis through CO hydrogenation on SiO$_2$-ZrO$_2$ supported Rh-based catalyst: The effect of support, Appl Catal A Gen, 454 (2013) 81-87.

[77] I.A. Fisher, A.T. Bell, A comparative study of CO and CO$_2$ hydrogenation over Rh/SiO$_2$, Journal of Catalysis, 162 (1996) 54-65.

[78] V.P. Santos, B. van der Linden, A. Chojecki, G. Budroni, S. Corthals, H. Shibata, G.R. Meima, F. Kapteijn, M. Makkee, J. Gascon, Mechanistic Insight into the Synthesis of Higher Alcohols from Syngas: The Role of K Promotion on MoS$_2$

Catalysts, Acs Catalysis, 3 (2013) 1634-1637.

[79] M. Saito, R.B. Anderson, The Activity of Several Molybdenum Compounds for the Methanation of Co, Journal of Catalysis, 63 (1980) 438-446.

[80] G.C. G.J. Quarderer, Dow Chemical company, European Patent 0119609, (1984).

[81] H.C. Xiao, D.B. Li, W.H. Li, Y.H. Sun, Study of induction period over K_2CO_3/MoS_2 catalyst for higher alcohols synthesis, Fuel Processing Technology, 91 (2010) 383-387.

[82] H.C. Woo, K.Y. Park, Y.G. Kim, I.S. Nam, J.S. Chung, J.S. Lee, Mixed Alcohol Synthesis from Carbon-Monoxide and Dihydrogen over Potassium-Promoted Molybdenum Carbide Catalysts, Appl Catal, 75 (1991) 267-280.

[83] N. Koizumi, K. Murai, T. Ozaki, M. Yamada, Development of sulfur tolerant catalysts for the synthesis of high quality transportation fuels, Catalysis Today, 89 (2004) 465-478.

[84] W.M.H. Sachtler, D.F. Shriver, W.B. Hollenberg, A.F. Lang, Promoter Action in Fischer-Tropsch Catalysis, Journal of Catalysis, 92 (1985) 429-431.

[85] S. Zaman, K.J. Smith, A Review of Molybdenum Catalysts for Synthesis Gas Conversion to Alcohols: Catalysts, Mechanisms and Kinetics, Catal Rev, 54 (2012) 41-132.

[86] R. Andersson, catalytic conversion of syngas to higher alcohols over MoS_2 based catalysts[J], KTH Royal Institute of Technology,2015.

[87] V.R. Surisetty, J. Kozinski, A.K. Dalai, Novel Ni-Co-Mo-K Catalysts Supported on Multiwalled Carbon Nanotubes for Higher Alcohols Synthesis, Journal of Catalysts, 2013 (2013) 1-7.

[88] S.S.C. Chuang, S.I. Pien, Infrared Studies of Reaction of Ethylene with Syngas on Ni/Sio2, Catalysis Letters, 3 (1989) 323-329.

[89] D.B. Li, N. Zhao, H.J. Qi, W.H. Li, Y.H. Sun, B. Zhong, Ultrasonic preparation of Ni modified K_2CO_3/MoS_2 catalyst for higher alcohols synthesis, Catalysis Communications, 6 (2005) 674-678.

[90] A.K.D. Venkateswara Rao Surisetty, and Janusz Kozinski, Alkali-Promoted Trimetallic Co-Rh-Mo Sulfide catalysts for Higher Alcohols Synthesis from

Synthesis Gas: Comparison of MWCNT and

Activated Carbon Supports, Ind. Eng. Chem. Res., 49 (2010) 6956-6963

[91] H.J. Guo, S.G. Li, F. Peng, H.R. Zhang, L. Xiong, C. Huang, C. Wang, X.D. Chen, Roles Investigation of Promoters in K/Cu-Zn Catalyst and Higher Alcohols Synthesis from CO_2 Hydrogenation over a Novel Two-Stage Bed Catalyst Combination System, Catalysis Letters, 145 (2015) 620-630.

[92] D.L.S. Nieskens, D. Ferrari, Y. Liu, R. Kolonko, The conversion of carbon dioxide and hydrogen into methanol and higher alcohols, Catalysis Communications, 14 (2011) 111-113.

[93] T. Inui, T. Yamamoto, M. Inoue, H. Hara, T. Takeguchi, J.B. Kim, Highly effective synthesis of ethanol by CO_2 hydrogenation on well balanced multi-functional FT-type composite catalysts, Appl Catal A Gen, 186 (1999) 395-406.

[94] S.G. Li, H.J. Guo, C.R. Luo, H.R. Zhang, L. Xiong, X.D. Chen, L.L. Ma, Effect of Iron Promoter on Structure and Performance of K/Cu-Zn Catalyst for Higher Alcohols Synthesis from CO_2 Hydrogenation, Catalysis Letters, 143 (2013) 345-355.

[95] X. Yang, X. Zhu, R. Hou, L. Zhou, Y. Su, The promotion effects of Pd on Fe–Cu–Co based catalyst for higher alcohols synthesis, Fuel Processing Technology, 92 (2011) 1876-1880.

Chapter II

Characterization techniques. Reaction
setup and carbon balance

In this chapter, the conditions used for the catalysts characterization will be introduced. The reaction setup including the test equipment and procedure as well as the analysis methods of products and the establishment of carbon balance will be presented.

The higher alcohols synthesis (HAS) most often yields to a complex mixture of oxygenates (alcohols, ketones, esters) and hydrocarbons (alkanes and olefins) in the short carbon chain range. H_2O and CO will also be present in the products. So it is a complex and challenge job to separate and analysis all these products and calculate the carbon balance.

II.1 The characterization techniques

II.1.1 Specific surface areas measurements

The surface areas of catalysts are measured by N_2 adsorption-desorption at -196 °C on a Micromeritics ASAP 2420 apparatus and calculated by Brunauer-Emmet-Teller (BET) method. The pore volume is calculated by the Barrett-Joyner-Halenda (BJH) method. The samples are outgassed at 250 °C for 3h before the measurements to remove the adsorbed moisture.

II.1.2 X-ray diffraction (XRD)

The crystalline structure of the catalysts were determined by XRD in a Brucker AXS-D8 Advanced equipment with Cu-Kα radiation (λ=1.5404 Å). The range scanned was from 10° to 90° with a 0.05° step size at a scan rate of 3 °·min^{-1}. The diffraction spectra have been indexed by comparison with the JCPDS files (Joint Committee on Powder Diffraction Standards). The average particle size was calculated using the Sherrer's equation:

$$D = \frac{K\lambda}{B \cos\theta} \qquad (2\text{-}1)$$

30

D (nm) is the mean size of the ordered (crystalline) domains, K is a dimensionless shape factor whose value is taken at 0.9, the X-ray wave length λ is 0.154056 nm, and B (rad) is the full width half maximum (FWHM), θ (rad) is the Bragg angle.

II.1.3 Temperature programmed techniques

II.1.3.1 The H_2 Temperature-Programed Reduction (H_2-TPR)

The H_2-TPR profiles were carried out at atmospheric pressure on a Micrometrics AutoChem II 2920, with TCD detector, on 50mg of fresh catalysts. The total gas flow rate is 50 mL·min^{-1} of 10 % H_2 in Ar with a heating ramp of 10 °C·min^{-1} to 800 °C.

The hydrogen consumption is deduced from the peak areas with respect to an external calibration.

II.1.3.2 Partial reduction experiment

The reduction, similar to the reduction procedure performed to activate the catalysts before catalytic test, was done in the same equipment as for the H_2-TPR. First, the catalyst was reduced at 400 °C for 60 min with the heating ramp 5 °C·min^{-1} under 50 mL·min^{-1} of 10 % H_2 in Ar atmosphere. Then the temperature was decreased to 50 °C under pure Ar atmosphere. At last the procedure of H_2-TPR was repeated. The objective is to characterize indirectly the extent of the initial reduction.

II.1.3.3 H_2 Temperature-programed Desorption (H_2-TPD)

The H_2-TPD profiles were carried out in the same equipment as for H_2-TPR. Because the concentration of desorbed H_2 was low, the MS detector was used. The fresh catalysts were first reduced at 400 °C for 60 min with heating ramp 5 °C·min^{-1} under a flow of 50 mL· min^{-1} of 5% H_2 in Ar. The temperature was then decreased to

50 °C under Ar atmosphere (50 mL·min^{-1}) and purged for 120 min. The pulse method was used to follow H_2 adsorption until the area of H_2 peaks did not change, accounting for a saturation. After a purge under He for 90 min, the temperature was increased to 800 °C with the heating ramp 10 °C·min^{-1}.

The hydrogen consumption is deduced from the peak areas with respect to an external calibration.

II.1.3.4 NH$_3$ Temperature-programed Desorption (NH$_3$-TPD) and CO$_2$ Temperature-programed Desorption (CO$_2$-TPD)

The process of NH$_3$-TPD is similar to that of H_2-TPD. The fresh catalysts were first reduced at 400 °C for 60 min with heating ramp 5 °C·min^{-1} under a flow of 50 mL·min^{-1} of 5% H_2 in Ar. The temperature was then decreased to 100 °C under Ar atmosphere and the system was purged for 120 min. The 5%NH$_3$/He mixture was used to do the adsorption for at least 8h until the concentration of NH$_3$ is stable. After NH$_3$ adsorption, pure He was used to purge the line for at least 8h, then the temperature was increased to 800 °C for 60 min with the heating ramp 10 °C·min^{-1}. The MS detector was used.

The procedure of CO$_2$-TPD was similar to that of NH$_3$-TPD, except that a 5%CO$_2$/He mixture was used during the adsorption step.

The molar quantity desorbed (NH$_3$ or CO$_2$) was calculated from the area of the desorption peaks compared to external calibrations.

II.1.4 X-ray photoelectron spectroscopy (XPS)

X-ray photoelectron spectroscopy (XPS) measurements of the support were performed on a MULTILAB 2000 (THERMO VG) spectrometer equipped with Al Kα anode (hv = 1486.6 eV) with 10 min of acquisition.

II.1.5 Transmission Electron Microscopy (TEM)

TEM observations were carried out by TOPCONEM-002B apparatus (accelerating voltage 200 kv) with an EDS KEVEX Deltapro Quantum for EDXS measurement.

II.1.6 Scanning Electron Microscope (SEM)

The SEM observations were done with a microscope JEOL FEG 6700F equipment at an accelerating voltage between 3 and 9 kV.

II.1.7 Mössbauer spectroscopy

The Mössbauer spectra measurement was done in the transmission mode with ^{57}Co diffused into a Rh matrix as the source moving with constant acceleration. The spectrometer was calibrated by means of a standard α-Fe foil and the isomer shift was expressed with respect to this standard at 293 K. The samples were measured at the temperature of 293 K. The fitting of the spectra was performed with the help of the NORMOS program. The experiments have been performed in the University Karlova of Prague (Czech Republic) by Dr. Daniel Nižňanský.

II.2 The reaction set up and analysis method

II.2.1 The reaction equipment

The catalysts are tested under a high-pressure equipment which is displayed in Figure 21. The maximum pressure can reach as high as 80bar. We used gas bottles containing 31.5% of CO_2, 63.5% of H_2 and 5% of N_2 (internal standard). Pure H_2 bottle was needed for the adjustment to the desired ratio of CO_2 and H_2.

The flow rate of gases are controlled by mass flow controllers Brooks SLA

5850S which are given signal by the electric Brooks0254. Then the gases enter a 1/4" tube and mix uniformly before the reactor. There is a three-way valve between the mixer and the reactor, which can be used to measure the volume flow rate and do the calibration before every reaction. The real volume flow rate of gases are measured accurately by the Agilent 3000 flow meter. There is a pressure indicator before the reactor which gives the real pressure in the equipment.

The reactions are performed in the fixed bed reactor with a 1/2" tube of 21cm length and 10.1 mm of inner diameter. The catalysts are put between two layers of silica wool. The fixed bed is supported by a quartz tube which can keep the catalyst bed stable. The reactor is heated by electrical resistance connected to a thermocouple just below the catalyst bed. The temperature is controlled by a PID regulator with an error ± 1 °C. After the reactor, there are two traps, the gas first passes the first trap cooled by air and   then passes the second trap cooled by cold water around 14 °C. The liquid phase in the fixed traps can be collected by two removable traps. The two removable traps are filled with N_2 until a pressure of about 0.5bar less than the pressure in reactor. After the pressure is stable, the valve between the fixed trap and removable trap is opened for 25 minutes. The liquid needs to be collected one trap by one trap.

At last, the gas phase passes the pressure controller Brooks 5866 and a heated 1/8" tube to the micro chromatograph.
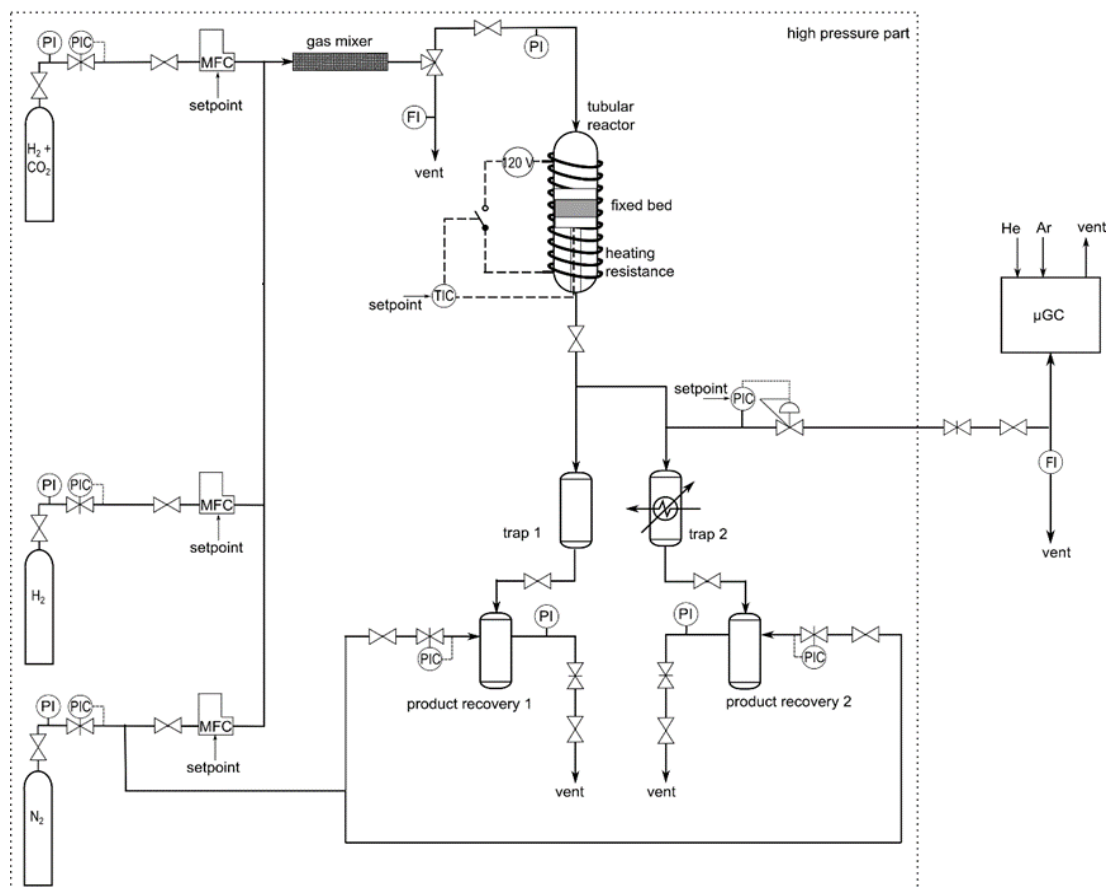
Figure 21 The scheme of the reaction setup

For all the reactions the catalysts were first reduced at 400 °C and 50 bar under pure H_2（11.8 mL·min^{-1}）for 60 min. Because of the low flow rate of H_2 and the small volume of catalyst bed, the effect of H_2 concentration is negligible. After reduction, the catalysts were cooled to 100 °C, and then the gas was changed to the mixture gas (H_2/CO_2=3), the total flow rate is 50 mL·min^{-1} of $H_2/CO_2/N_2$. N_2 (1.9 mL·min^{-1}) was used as internal standard. The reaction was performed between 250 °C to 350 °C with a Gas Hourly Space Velocity (GHSV) of 5000 h^{-1} (STP). The flows were kept constant and the catalyst mass was adjusted depending on the apparent density of the materials.

II.2.2 The analysis method

After separating the gas phase and liquid phase in the reaction equipment, the

products in the two phases will be analyzed respectively in a micro chromatograph (on line analysis) SRA3000 with TCD detector and in a chromatograph (off line analysis) Agilent 6890N with FID detector.

II.2.3.3 The analysis of gas phase

The gas phase was analyzed on line by a micro chromatograph SRA3000 with TCD detector. There are four columns (A to D) in the micro chromatograph which are detailed in Table 1 and analytical conditions are shown in Table 2. Because all the products can be detected on the columns A, B and C, the column D (stabilwax) will not be used.

The first step has been to inject and identify every possible reaction products in the chromatograph. The second step has been to develop adequate method to separate all the peaks to be sure that the areas will be integrated correctly and the product quantified correctly. In order to obtain correct separations, the carrier gas pressure and temperature of the column have been modified.

The retention time and response factor of products in gas phase are presented in Table 3, Table 4, and

Table 5 for the three columns. The relative response factors of H_2, N_2, CH_4 and CO in column A were calculated by ourselves. We assumed that the response factor of CH_4 is 1, and a gas mixture containing 20% of CH_4, 20% of CO, 20% of H_2, 20% of CO, and 20% of N_2 was used to calculate the relative response factors. Because the flow rate of hydrogen is not very stable, the response factor of H_2 can change a little with different reaction equipment and time, but this change doesn't effect a lot to the carbon balance compared to the effect of all the other alkylating agents.

The calculation of N_2 relative response factor is given for example:

$$\frac{A_{CH_4}}{A_{N_2}} = \frac{R_{CH_4}}{R_{N_2}} \qquad (2-2)$$

A_{CH_4}:The area of CH_4 in column A; A_{N_2}:The area of N_2 in column A

R_{CH_4}:Response factor of CH_4 in column A; R_{N_2}: Response factor of N_2 in column A

The relative response factors of products in columns B and C are those reported by Dietz [1].

Table 1 The columns and functions in the micro chromatograph SRA3000

Column	Type	Carrier gas	Function
A	MS5A	Ar	H_2, N_2, CH_4, CO
B	PoraplotU	He	CH_4 , CO_2 , C_2H_4 ,C_2H_6
C	OV-1	He	Hydrocarbons(C_{2+}) and alcohols

Table 2 Conditions of MicroGC for the analysis of gas phases

Conditions/columns	Column A	Column B	Column C	Column D
Injection temperature (°C)	90	90	90	90
Analysis temperature (°C)	70	45	45	50
Analysis pressure (psi)	30	18	35	23

Table 3 The retention times and relative response factors in column A

of micro chromatograph SRA3000

Column A		
Gas	Retention time (s)	Response factor
H_2	62.74	×0.1993
N_2	107.68	×2.2371
CH_4	140.75	×1
CO	230.82	×2.3378

Table 4 The retention times and relative response factors in column B

of micro chromatograph SRA3000

Column B		
Gas	Retention time (s)	Response factor
CH_4	14.87	/35.7
CO_2	37.14	/48
C_2H_4	39.97	/48
C_2H_6	64.53	/51.2

Table 5 The retention times and relative response factors in column C micro chromatograph

SRA3000

Column C		
Gas	Retention time (s)	Response factor
CH_4	33.37	/35.7
C_2H_4	34.21	/48
CO_2	34.45	/48
C_2H_6	36.92	/51.2
C_3H_6	40.21	/64.5
C_3H_8	40.81	/64.5
H_2O	44.15	/33
CH_3OH	54.35	/55
$1-C_4H_8$	56.04	/81
C_4H_{10}	58.52	/85
Trans $2-C_4H_8$	61.33	/85
Cis $2-C_4H_8$	66.17	/87
C_2H_5OH	75.54	/72
acetone	94.56	/86
HCOOH	99.06	

C_5H_{10}	102.91	/98.5
C_5H_{12}	110.29	/105
Cis+trans C_5H_{10}	115.28	/104
Cis+trans C_5H_{10}	121.36	/98.5
C_3H_7OH	148.00	/83
2-C_4H_9OH	199.13	/96
C_6H_{12}	203.93	
C_6H_{14}	227.68	/123
Cis+trans C_6H_{12}	229.00	
C_4H_9OH	201.64	/95
C_7H_{16}	484.76	/143

II.2.3.4 The analysis of liquid phase

The products in the liquid phase are collected during a certain reaction time during which the micro chromatograph will analyze the gas phase every 1 h. A chromatograph Agilent 6890N with a Solgelwax (60 m×250 μm×0.25 μm) column and a flame ionization detector is used to analyze the liquid phase. A certain quantity of sample is mixed with a known amount of 2-pentanone as internal standard. The amount of 2-pentanone has to be less than 10% of the weight of samples in order to avoid the insolubilization. 1μL of this mixture is injected into the chromatograph and separated.

The chromatographic method was the following:

Carrier gas: He, flow rate: 1.3 mL·min^{-1}

Oven program: 40 °C for 3 min

5 °C·min^{-1} from 40 °C to 140 °C hold 1 min

8 °C·min^{-1} from 140 °C to 250 °C hold 30 min

Detector: FID 250 °C, 40 mL·min^{-1} H_2

The response factors were measured under the same conditions. First, all the possible reaction products were injected into the chromatograph and the retention time was obtained. Second, a mixture of possible products with a known amount of 2-pentanone and water was analyzed. For every products, three samples with different amounts of product, 2-pentanone and water were prepared and the analysis for every samples repeated three times. The average relative response factors (with respect to 1 for 2-pentanone) and the error of all the possible products are presented in the Table 6.

Table 6 The retention times and relative response factors of the possible products in liquid phase

Alcohols		Retention time	Response factor	Error
pentane	C_5H_{12}	4.317	×0.6907	0.0171
1-pentene	C_5H_{10}	4.358	-	-
n-hexane	C_6H_{14}	4.435	×0.6943	0.0067
1-hexene	C_6H_{12}	4.526	-	
octane	C_8H_{18}	5.266	×0.6501	0.0124
1-octene	C_8H_{16}	5.657	-	
acetone	C_3H_6O		×1.1700	
methanol	CH_3OH	6.477	×0.0823	0.0208
2-propanol	C_3H_7OH	6.933	×1.3229	
ethanol	C_2H_5OH	7.051	×1.4227	0.0084
2-butanol*	C_4H_9OH	9.143	×1.1157	
1-propanol	C_3H_7OH	9.118	×1.1099	0.0035
1-butanol	C_4H_9OH	11.837	×1.0240	0.0073
dodecane	$C_{12}H_{26}$	13.813	×0.7282	0.0311
1-octanol	$C_8H_{17}OH$	22.856	×0.7827	0.0642
1-nonanol	$C_9H_{19}OH$	25.375	×0.7074	0.0457
1-decanol	$C_{10}H_{21}OH$	27.553	×0.6914	0.0249

* 2-butanol is between 1-propanol and 1-butanol and overlap 1-propanol, so sometimes it is a little difficult to be separated from 1-propanol.

II.2.3 The calculation method

II.2.3.1 The calculation of data from micro chromatograph

Because there are three columns that were used to analyze the products, it is important to find a link between these columns. In our calculation, the column A and B are linked by CH_4, the column B and C are linked by C_2H_6.

First, the blank was did. After reduction under pure H_2 atmosphere, the mixture of CO_2 and H_2 was added to the equipment, in order to make sure that the ratio of CO_2 and H_2 is the desired one, the blank was did before the reaction. According to the data obtained from micro chromatograph, the real ratio of CO_2/H_2 is calculated. As columns A and B need to be linked by CH_4, the temperature of 220 °C was chosen as temperature for the blank analysis. The reaction just begins at this temperature and a very small amount of methane is formed which allows to link the two columns.

Second, the areas of all the products are corrected by response factors.

Third, the corrected areas of peaks in column B and C are linked to column A.

Fourth, the molar flow rate and total mole of all products are calculated by the internal standard N_2.

The molar flow rate of N_2 (F_{N_2}) can be calculated by equation $(2-3)$

$$F_{N_2} = \frac{Q_{N_2} \; mL \cdot min^{-1} \cdot 60 \; min \cdot h^{-1}}{24000 \; mL \cdot mol^{-1}} \qquad (2-3)$$

$$F_{CO_2} = F_{N_2} \cdot \frac{A_{CO_2}}{A_{N_2}} \qquad (2-4)$$

$$F_{H_2} = F_{N_2} \cdot \frac{A_{H_2}}{A_{N_2}} \qquad (2-5)$$

$$F_i = F_{N_2} \cdot \frac{A_i}{A_{N_2}} \qquad (2-6)$$

i is one of the products

The F_{N_2}, F_{CO_2}, F_{H_2} and F_i are molar flow rates of N_2, CO_2, H_2 and the products, the unit is mol·h^{-1}. Q_{N_2} (mL·min^{-1}) is the volume flow rate of N_2. The A_{N_2}, A_{CO_2}, A_{H_2} and A_i are the areas after correction by the response factor and link between columns.

$$n_{CO_2} = \sum_{t=t_0}^{t_{end}} F_{CO_2}(t_i) \cdot \Delta t_i \qquad (2-7)$$

$$n_{H_2} = \sum_{t=t_0}^{t_{end}} F_{H_2}(t_i) \cdot \Delta t_i \qquad (2-8)$$

$$n_{g,i} = \sum_{t=t_0}^{t_{end}} F_i(t_i) \cdot \Delta t_i \qquad (2-9)$$

The n_{CO_2}, n_{H_2} and $n_{g,i}$ are the total moles in the gas phase leaving the reactor during the reaction time, the unit is mol.

II.2.3.2 The calculation of data from chromatograph for liquid phase

The quantity of products in mixture are calculated according to the mass of 2-pentanone m$_{2\text{-pentanone}}$ (g), the area of products A$_i$ and A$_{2\text{-pentanone}}$ and the relative response factor R$_i$.

$$m_{l,i} = m_{2-pentanone} \cdot \frac{A_i}{A_{2-pentanone}} \cdot R_i \qquad (2-10)$$

The mole of products ($n_{l,I}$ (mol)) in liquid phase were calculated according to the $m_{l,i}$ and molar mass M_i:

$$n_{l,i} = \frac{m_{l,i}}{M_i} \qquad (2-11)$$

At last, the total mole $n_{t,i}$ (mol) of one products was calculated:

$$n_{t,i} = n_{g,i} + n_{l,i} \qquad (2-12)$$

The selectivity of one of products S_i can be calculated by the following formula.

$$S_i = 100\% \cdot \frac{(number\ of\ C\ in\ i).n_{t,i}}{\Sigma(number\ of\ C\ in\ i).n_{t,i}} \qquad (2-13)$$

The productivity of one products P_i is calculated by formula $(2-14)$

$$P_i(g_i\ g_{cata}^{-1}\ h^{-1}) = \frac{m_i}{m_{cata} \cdot t} \qquad (2-14)$$

The conversion of CO_2 (X_{CO_2}) and H_2 (X_{H_2}) are calculated by three methods to compare if the calculation is correct.

$$X_{CO_2} = 100\% \cdot \frac{\Sigma(number\ of\ C\ in\ i).n_{t,i}}{n_{in,CO_2}} \qquad (2-15)$$

$$X_{CO_2} = 100\% \cdot \frac{\Sigma(number\ of\ C\ in\ i).n_{t,i}}{\Sigma(number\ of\ C\ in\ i).n_{t,i} + n_{out,CO_2}} \qquad (2-16)$$

$$X_{CO_2} = 100\% \cdot \frac{n_{in,CO_2} - n_{out,CO_2}}{n_{in,CO_2}} \qquad (2-17)$$

$$X_{H_2} = 100\% \cdot \frac{\Sigma(number\ of\ H\ in\ i).n_{t,i}}{n_{in,H_2}} \qquad (2-18)$$

$$X_{H_2} = 100\% \cdot \frac{\Sigma(number\ of\ H\ in\ i).n_{t,i}}{\Sigma(number\ of\ H\ in\ i).n_{t,i} + n_{out,H_2}} \qquad (2-19)$$

$$X_{H_2} = 100\% \cdot \frac{n_{in,H_2} - n_{out,H_2}}{n_{in,H_2}} \qquad (2-20)$$

The results calculated by the second method (according equations $(2-16)$ and $(2-19)$ will be presented in this thesis. Because the blank was done at 220 °C when the reaction already started, the inlet moles of H_2 and CO_2 are not very accurate.

II.3 References

[1] W. Dietz, Response factors for gas chromatographic analyses, J Chromato Sci, 5 (1967) 68-71.

Chapter III

The reactivity of Cu, Co, Fe mixed oxides/spinel-based catalysts for the CO$_2$ hydrogenation

III.1 Introduction

In this chapter, in the first part, Co, Cu and Fe elements have been chosen as active metals, and the $CoFe_2O_4$, $CuFe_2O_4$, $CuCo_2O_4$ and $Cu_{0.5}Co_{0.5}Fe_2O_4$ spinel structure materials as catalysts precursors will be presented. The corresponding four materials are named CoFe-precursor, CuFe-precursor, CuCo-precursor and CuCoFe-precursor.

In order to obtain the spinel structure, the precursor will be calcined under different temperatures and characterized by XRD and H_2-TPR. As discussed in the introduction, the cooperation of the two or three active metals is really important for the higher alcohols synthesis. It is better to control the position of active site in atoms rank, part of spinel or alloy will be expected after reduction, so the results of H_2-TPR will be used to find suitable reduction temperature.

In the second part, the CoFe-precursor, CuFe-precursor, CuCo-precursor and CuCoFe-precursor calcined at 800 °C will be characterized with several techniques and discussed in details.

Finally, their performance in CO_2/H_2 reaction will be presented.

III.2 Preparation of spinel precursor materials

The spinel-based materials were synthesized by a pseudo sol-gel method, which is based on the thermal decomposition of propionate mixed precursors. The process is shown in Figure 22. Cobalt (II) acetate, iron (II) acetate and copper (II) acetate were used as starting materials. The starting salts, in adequate amounts to form $CoFe_2O_4$, $CuFe_2O_4$, $CuCo_2O_4$ and $Cu_{0.5}Co_{0.5}Fe_2O_4$, were dissolved in propionic acid in a concentration of 0.12 mol·L^{-1} in cation. All these starting salts led to propionate precursors in propionic acid. Then the two or three solutions were mixed together and

maintained under reflux for 90 min at about 141 °C. The solvent was evaporated until a solid resin was obtained [1, 2]. The obtained resins were calcined at different temperatures for 6h (heating rate of 2 °C·min^{-1}) under air. The catalysts were crushed and sieved to 100-200 μm for the reaction.
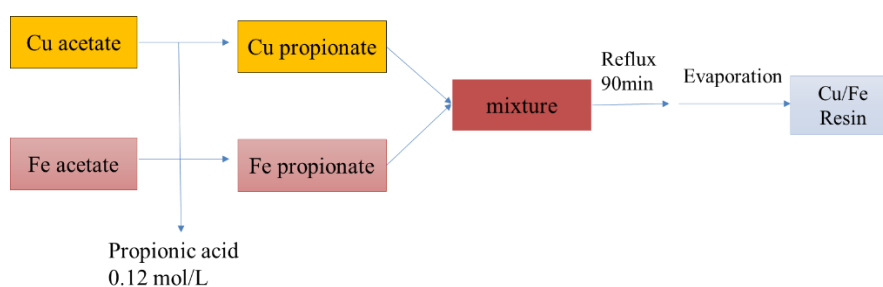
Figure 22 The pseudo sol-gel method for the synthesis

III.3 Effect of the calcination temperature on spinel formation

III.3.1 CoFe-precursor

According to the XRD profiles in Figure 23, the $CoFe_2O_4$ spinel can be obtained at calcination temperature of 450 °C as unique detected crystalline structure. Nevertheless, higher calcination temperature largely improves the crystallinity of the spinel. The size of crystals (Table 9) increased from 16 nm to 35 nm with the calcination temperature increase from 450 °C to 800 °C.
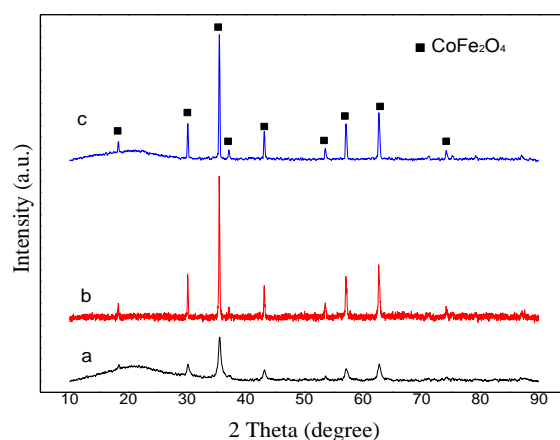
Figure 23 Room temperature XRD patterns of CoFe-precursor after calcination at different temperatures: (a) 450 °C, (b) 700 °C, (c) 800 °C

Table 7 The crystallite size of CoFe$_2$O$_4$ spinel of CoFe-precursor

after being calcined under different temperature

Calcination temperature (°C)	450	700	800
Crystallite size (nm) CoFe$_2$O$_4$	16	33	35

The profiles H$_2$-TPR of CoFe-precursor calcined at different temperatures are shown in Figure 24. There are three reduction peaks (344 °C, 481 °C and ~550 °C) in the H$_2$-TPR profile of CoFe-precursor calcined at 450 °C. There is only one reduction peak at around 500 °C in the profile of CoFe-precursor calcined at 800 °C. The maximum reduction temperature increased from ~550 °C to ~600 °C with calcination temperature from 450 °C to 700 °C, but deceased to ~502 °C when calcination temperature increased to 800 °C.

The small peak at 344 °C was assigned to the reduction of Fe$_2$O$_3$ to Fe$_3$O$_4$ [3], and it disappeared when calcination temperature increased, in accordance to the better crystallization of the spinel evidenced by XRD. The three biggest peaks at 481 °C, 533 °C and 502 °C can be attributed to the reduction of Fe^{3+}→Fe^{2+} and Co^{2+}→Co [4], the shoulder peak was the reduction of Fe^{2+}→Fe^{o} [4]. The shoulder peak disappeared when the CoFe-precursor was calcined under 800 °C, which indicates that the Co^{2+} and Fe^{3+} may be reduced to metallic Co and Fe at the similar temperature.

The easily reducible Co^{2+} can promote the reduction of iron cations [5], because of the H$_2$ can dissociatively adsorb on reduced Co particles, then the spillover of hydrogen atoms from cobalt to iron can lower the reduction temperature of nearby iron oxides [6], so the CoFe$_2$O$_4$ spinel should be reduced as easily as or more easily than metal oxides such as Co$_3$O$_4$ or Fe$_2$O$_3$/Fe$_3$O$_4$. The decreasing maximum reduction temperature indicates the formation of perfect CoFe$_2$O$_4$ spinel structure, which is also corresponding to the results of XRD.
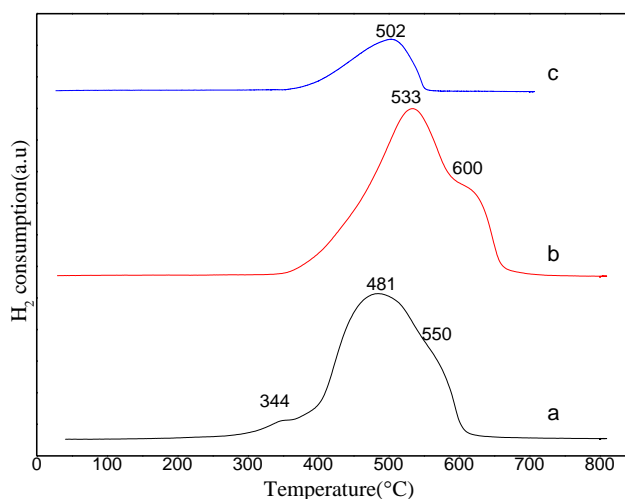
Figure 24 The H_2-TPR profiles of CoFe-precursor after calcination at different temperatures:

(a) 450 °C, (b) 700 °C, (c) 800 °C

Combining the results of XRD and H_2-TPR, the best calcination temperature is 800 °C, and 400 °C was chosen as reduction temperature.

III.3.2 CuFe-precursor

The XRD profiles of materials calcined under different temperature are shown in Figure 25. After calcination at 600 °C, the diffractions lines of $CuFe_2O_4$ together with those of Fe_2O_3 and CuO appeared. When calcination temperature increased to 700 °C, there was still minor amounts of Fe_2O_3 and CuO. The reflections of Fe_2O_3 disappeared at calcination temperature at 800 °C, but CuO still existed in the material even after calcination at 1000 °C, which indicates that the crystallized $CuFe_2O_4$ is a copper deficient spinel phase. This phenomenon was also found by many other researchers [7, 8]. The distribution of Cu ions is deeply affected by calcination temperature and the phase transition tetragonal $CuFe_2O_4$ and cubic $CuFe_2O_4$. At high temperature, Cu^{2+} can be thermally partially reduced to Cu^+, then re-oxidized, which leads to the segregation of CuO [8, 9].
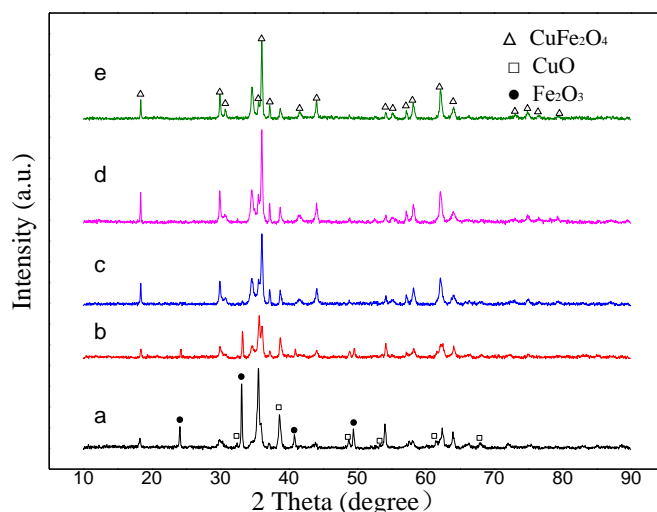
Figure 25 Room temperature XRD patterns of CuFe-precursor after calcination at different temperatures: (a) 600 °C, (b) 700 °C, (c) 800 °C, (d) 900 °C, (e) 1000 °C

Figure 26 shows the profiles of H_2-TPR of CuFe-precursors which were calcined at different temperatures. Except for the broad reduction peak above 400 °C, there are four reduction peaks in H_2-TPR profiles of CuFe-precursor calcined at 600 °C. When calcination temperature increased to 700 °C, there is only two peaks. The H_2 reduction profiles are similar between CuFe-precursor after calcination at 800 °C and 900 °C, three reduction peaks appeared below 400 °C.

There is a broad peak between 400 °C and 700 °C in all the H_2-TPR profiles, these peaks can be attributed to the reduction of Fe_3O_4 to Fe^0 [10, 11]. From the results of XRD, it is known that $CuFe_2O_4$ along with CuO and Fe_2O_3 phases coexist in the CuFe-precursor calcined at 600 °C. The small reduction peak at 162 °C in Figure 26 (a), can be attributed to the reduction of highly dispersed CuO, easily reducible [12]. The peaks at 223 °C with two shoulder peaks are attributed the reduction of $CuFe_2O_4$ to Cu and Fe_2O_3, and Fe_2O_3 to Fe_3O_4 [13]. As for H_2-TPR profiles of CuFe-precursor calcined at 700 °C, the peak at 297 °C with a shoulder peak can also be attributed to the reduction of $CuFe_2O_4$ to metallic Cu and Fe_2O_3, and Fe_2O_3 to Fe_3O_4. Although there are diffractions lines of CuO and Fe_2O_3 in XRD patterns, it was difficult to evidence the reduction of CuO in H_2-TPR profile.

The reduction peak at 239 °C in H_2-TPR profile of CuFe-precursor calcined at

800 °C may be caused by the reduction of re-oxidized CuO, the peak at around 298 °C is caused by the reduction of $CuFe_2O_4$ to Cu and Fe_2O_3, and this peak is much smaller than the reduction peak of Fe_2O_3 (324 °C). This may be due to the segregation of CuO from $CuFe_2O_4$ at high calcination temperature. The CuFe-precursor calcined at 900 °C presents the same reduction profile than CuFe-precursor calcined at 800 °C.
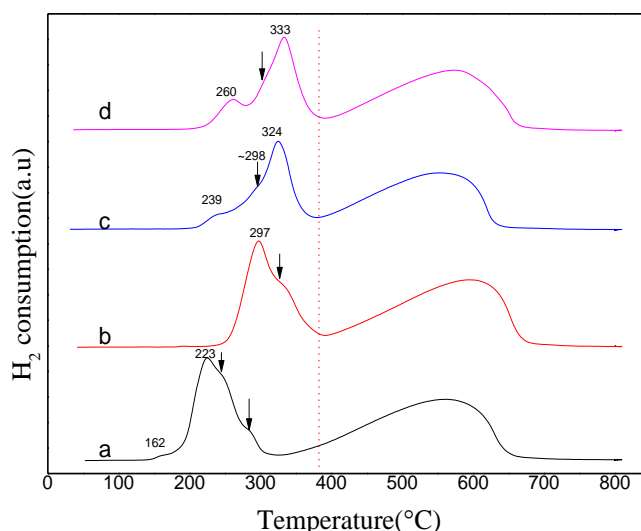
Figure 26 The H₂-TPR profiles of CuFe-precursor after calcination at different temperatures: (a) 600 °C, (b) 700 °C, (c) 800 °C, (d) 900 °C

As for CuFe-precursor, the temperature of 800 °C is chosen as calcination temperature in order to obtain the spinel structure, and the reduction temperature is fixed at 400 °C.

III.3.3 CuCo-precursor

The XRD patterns of CuCo-precursors which were calcined at different temperatures are shown in Figure 27. A crystallized structure is obtained after calcination at 600 °C. CuO always existed in the catalyst, even when the calcination temperature increased to 1000 °C. As the diffraction patterns of spinels Co_3O_4 and $Cu_{0.86}Co_{2.14}O_4$ are similar, it is difficult to detect the exact phase in the structure.

According to the research of A.J. Marchi [14] the spinel phase could be mainly Co_3O_4.

The particle sizes of spinel and CuO phases are shown in Table 8. The particle sizes were different at different calcination temperature. The sizes of CuO, estimated by the reflection of (111) plane, increased from 28 nm to 33 nm with calcination temperature increase from 600 °C to 900 °C，but decreased to 30 nm at calcination temperature of 1000 °C. The crystal sizes of spinel (Co_3O_4 or $Cu_{0.86}Co_{2.14}O_4$), estimated by (311) plane, also displayed the same tendency.
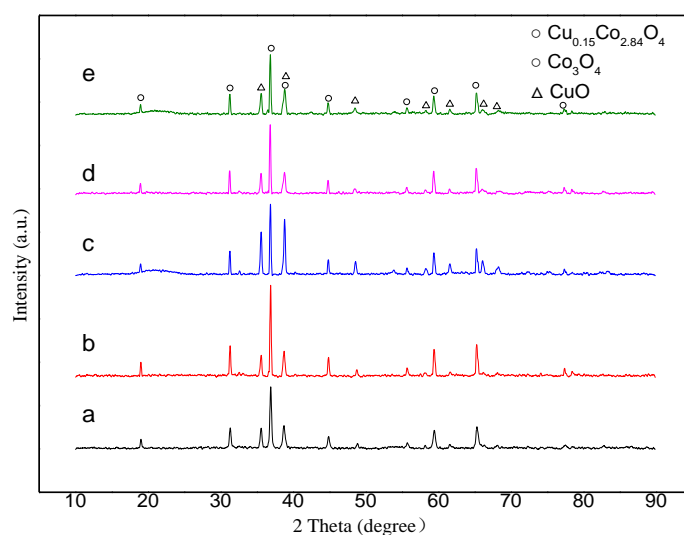
Figure 27 Room temperature XRD patterns of CuCo-precursor after calcination at different temperatures: (a) 600 °C, (b) 700 °C, (c) 800 °C, (d) 900 °C, (e) 1000 °C

Table 8 The crystallite sizes of spinel and CuO phases of CuCo-precursor

after calcination at different temperatures

Calcination temperature (°C)	600	700	800	900	1000
Crystallite size (nm)					
Spinel	31	39	39	41	39
CuO	28	33	33	33	30

The H$_2$ reduction profiles of CuCo-precursor after calcination at 600 °C，800 °C and 900 °C are shown in Figure 28. There are three reduction peaks in the H$_2$ reduction profiles of CuCo-precursor after calcination at 600 °C. With calcination temperature increase to 800 °C, there are still three reduction peaks, but the relative area between three peaks is largely different from CuCo-precursor after calcination at 600 °C. The H$_2$ reduction profile of CuCo-precursor after calcination at 900 °C is totally different, there are at least four reduction peaks.

In the H$_2$-TPR profile of CuCo-precursor after calcination at 600 °C, the reduction peak at 218 °C is due to the reduction of highly dispersed CuO. The reduction peaks at around 280 °C and 348 °C may be attributed to the reduction of CuCo$_2$O$_4$ to Cu and Co$_3$O$_4$ and two steps reduction of Co$_3$O$_4$: Co$_3$O$_4$ → CoO → Co^0 [15-17].

Many researchs showed that the Cu-Co spinel is very difficult to synthesize and suffers from low thermal stability [18, 19]. It's not enough to form the CuCo spinel at low temperature, but when tempreture is too high, the CuCo spinel will not be stable. The stability of CuCo$_2$O$_4$ was measured to be 400 to 450 °C and the increase of the Cu/Co ratio could lead to a decrease of the thermal stability of the Co-Cu spinel [19]. The results of Tian *et al.* [19] showed that the diffraction lines of Co-Cu oxides were very intense between 205 to 650 °C. When temperature increases to 655 °C, the diffraction gets weaker, and the spinel structure had partial decomposition in temperature range 830 °C - 860 °C according to the research of Paknahad *et al.* [20]. So, during the calcination of CuCo-precursor at 800 °C, CuCo$_2$O$_4$ may be first formed at low temperature and then partially decomposed at high temperature, leadind to CuO. The area of reduction peak of CuO (245 °C) is relatively larger than the reduction peak of CuCo$_2$O$_4$ (269 °C) compared to the H$_2$ reduction profile of CuCo-precursor after calcination at 600 °C. When the calcination temperature increased to 900 °C, most of spinel structure may be decomposed, and it is not a mixture of CuO and Co$_3$O$_4$ or CuO and Co$_2$O$_3$ but a complexity [21], so the H$_2$

reduction profile of CuCo-precursor after calcination at 900 °C is more complex than after calcination at 600 °C and 800 °C. This may also explain the change of particles sizes of spinel and CuO with calcination temperature.
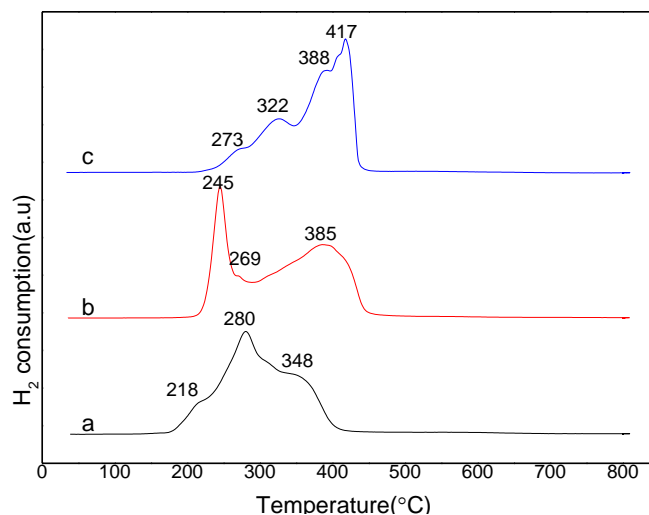
Figure 28 The H_2-TPR profiles of CuCo-precursor after calcination at different temperatures: (a) 600 °C, (b) 800 °C, (c) 900 °C

From the results of XRD and H_2-TPR, we found that the pure $CuCo_2O_4$ spinel was very difficult to form, this is consistent with the results of Gautier *et al.* [22], and $CuCo_2O_4$ also shows low thermal stability. In order to keep consistent with CoFe-precursor and CuFe-precursor, we also choose 800 °C as calcination temperature.

III.3.4 CuCoFe-precursor

According to the XRD patterns in Figure 29, there are $CoFe_2O_4$, $CuFe_2O_4$ spinel phases, iron oxides phase (Fe_3O_4, Fe_2O_3) and CuO in the CuCoFe-precursor after calcination at from 400 °C to 1000 °C. It is difficult to detect the Cu, Co and Fe mixed spinel.
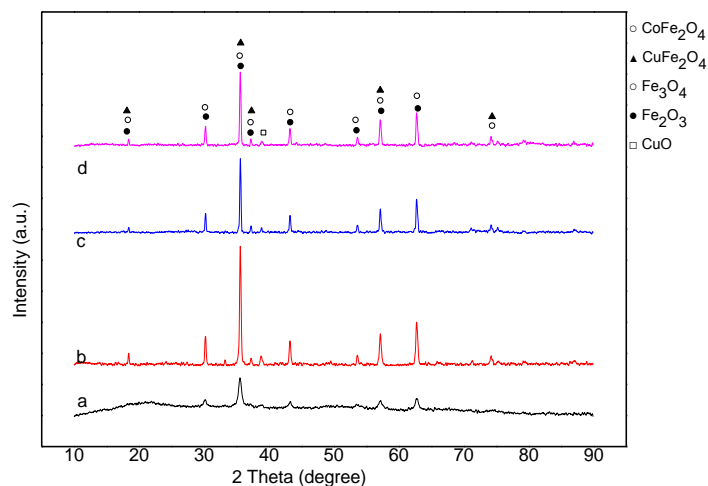
Figure 29 Room temperature XRD patterns of CuCoFe-precursor after calcination at different temperatures: (a) 400 °C, (b) 600 °C, (c) 800 °C, (d) 1000 °C

Figure 30 shows the H_2-TPR profiles of CuCoFe-precursor after calcination at different temperatures. The broad peaks above 400 °C correspond to the two steps reduction of Fe_3O_4 to Fe^0 through FeO and the reduction of Co_3O_4. The peaks at low temperature can be attributed to the reduction of $Cu^{2+} \rightarrow Cu^0$ and $Co^{2+} \rightarrow Co^0$.
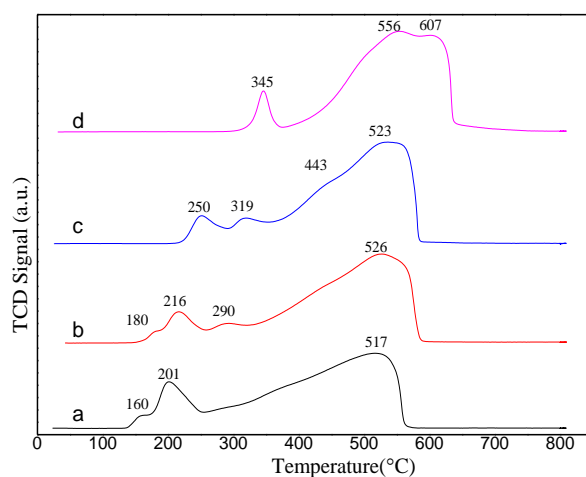
Figure 30 The profiles H_2-TPR of CuCoFe-precursor calcined at different temperatures: (a) 400 °C, (b) 600 °C, (c) 800 °C, (d) 1000 °C

III.3.5 Conclusions for the synthesis

In this part, the CoFe-precursor, CuFe-precursor, CuCo-precursor and

CuCoFe-precursor were prepared as spinel-based precursor catalysts. For all the four precursors, there exist spinel phases, even not always as unique crystalline phases. The temperature of 400 °C will be chosen as reduction temperature for the catalysts, so that spinel phases may already exist in the structure after reduction to support the metallic phases formed by reduction (except for Cu-Co mixed oxides).

> ➢ The CoFe$_2$O$_4$ spinel can be easily synthesized and high calcination temperature increase crystallinity of spinel phase.
>
> ➢ The CuFe$_2$O$_4$ spinel is always formed along with CuO, high calcination temperature can lead to Cu-deficiency copper iron spinel.
>
> ➢ CuCo$_2$O$_4$ spinel is difficult to be synthesized, because of the low thermal stability, there are mainly CuO and Co$_3$O$_4$ in the CuCo-precursor after calcination at high temperature.
>
> ➢ There are may be CuFe-spinel and CoFe-spinel in the material of CoCuFe-precursor after calcination, but the CuCoFe mixed spinel was not evidenced by XRD.

III.4 Characterizations of the catalysts calcined at 800 °C

In this part, we will detail the characterization and performance of CoFe-precursor, CuFe-precursor, CuCo-precursor and CuCoFe-precursor after calcination at 800 °C. The four materials are named CoFe-precursor-800, CuFe-precursor-800，CuCo-precursor-800 and CuCoFe-precursor-800.

III.4.1 Textural and structural properties of catalysts

The Table 9 displays the surface areas, porosity and density of the four spinel-based materials. Because of the high calcination temperature (800 °C), the surface area of the four kinds of materials is very small: between 1 and 3 $m^2 \cdot g^{-1}$. The density of four materials is similar, between 1.3 $g \cdot cm^{-3}$ and 1.9 $g \cdot cm^{-3}$.

Table 9 Structure and textural properties of the precursors

Catalyst	S_{BET} ($m^2 \cdot g^{-1}$)	Density ($g \cdot cm^{-3}$)
CoFe-precursor-800	2	1.8
CuFe-precursor-800	1	1.3
CuCo-precursor-800	1	1.9
CuCoFe-precursor-800	3	1.5

III.4.2 X-ray photoelectron spectroscopy (XPS)

III.4.2.1 The XPS analysis of CoFe-precursor-800

In order to obtain the oxidation state and the surface chemical composition of CoFe-precursor-800 raw material, the X-ray photoelectron spectroscopy (XPS) measurements in the Co 2p , Fe 2p and O 1s region are shown in Figure 31 (a) , (b) and (c).
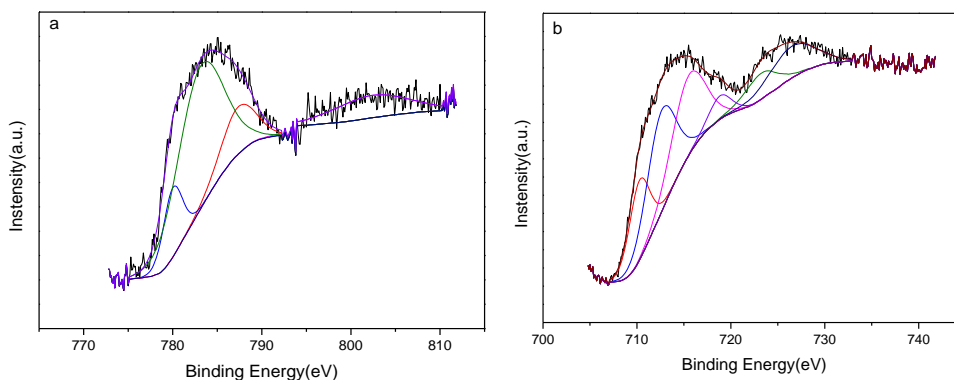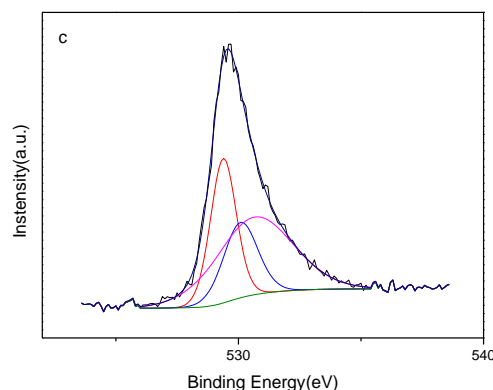
Figure 31 XPS of (a) Co 2p, (b) Fe 2p, (c) O 1s of CoFe-precursor-800

The two peaks with binding energy at 780.0 and 783.1 eV are ascribed to Co^{2+} ions in octahedral sites and tetrahedral sites respectively [23]. The peak with binding energy at 787.4 eV is a typical shake-up satellite of peak of Co^{2+} at 780.0 eV [24-26].

The main peak of Fe 2p spectra is at a binding energy around 710.3 eV, which is accompanied by a satellite peak at a binding energy around 718.3 eV. This indicates the presence of Fe^{3+} ions [27]. The doublets of Fe $2p_{3/2}$ binding energy at 710.3 eV and Fe $2p_{1/2}$ binding energy at 723.2 eV are due to Fe^{3+} ions in octahedral sites, while the doublets of Fe $2p_{3/2}$ binding energy at 712.6 eV [28] and Fe $2p_{1/2}$ binding energy at 726.5 eV are due to Fe^{3+} ions in tetrahedral sites [23]. The peak at binding energy 715.5 eV is satellite peak of peak at a binding energy at around 710.3 eV, which may indicate the presence of Fe^{2+} [29]. Nappini *et al.* also found that a small amount of unexpected Fe^{2+} replaced the Co^{2+} ions in the $CoFe_2O_4$ structure, which may come from the preservation of the overall neutral charge balance of the unit cell [30].

The O 1s region is fitted to three peaks of binding energies at 529.7 eV, 531.2 eV and 534.3 eV. The main peak at 529.7 eV is attributed to the contribution of the crystal lattice oxygen. The exact assignment of the higher binding energy peaks is rather complex and controversial, which may be attributed to chemisorbed oxygen species [31].

The surface Fe/Co ratio that is calculated according to the results of XPS is 1.48. The percentage of Co^{2+} in octahedral and tetrahedral sites is 83% and 17%

respectively. The surface ions distribution calculated according to the results of XPS is $(Co_{0.17}Fe_{0.83})_{tetra}[Co_{0.83}Fe_{1.27}]_{octa}O_4$ corresponding to a mostly inverse spinel (83% of inversion).

According to the calculation, in CoFe-precursor-800, the Co^{2+} cations prefer to occupy octahedral sites. The OSPE (octahedral site preference energy) of Co^{2+} is -31.0 kJ/mol is larger than OSPE of Fe^{3+} (0 kJ/mol). The OSPE shows the affinity of a transition metal ion for octahedral site in spinel structure, so the structure of $CoFe_2O_4$ spinel is clearly expected to be an inverse spinel [32]. Since the surrounding oxygen atoms exert a week field environment, the degenerate d-orbitals of Co^{2+} splits to give the resultant high spin electronic configuration of $t_{2g}^5 e_g^2$. With this electronic configuration, the crystal field stabilization energy of octahedral sites is -0.8 Δ_o, so the Co^{2+} ions prefer occupy the octahedral site [33].

III.4.2.2 The XPS analysis of CuFe-precursor-800

The X-ray photoelectron spectroscopy (XPS) measurements for the composite of CuFe-precursor-800 in the Cu 2p, Fe 2p and O 1s region are shown in Figure 32 (a) , (b) and (c).
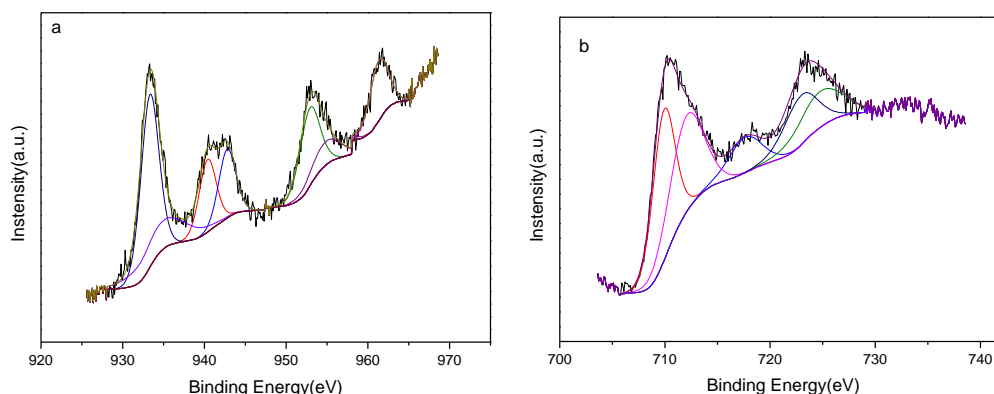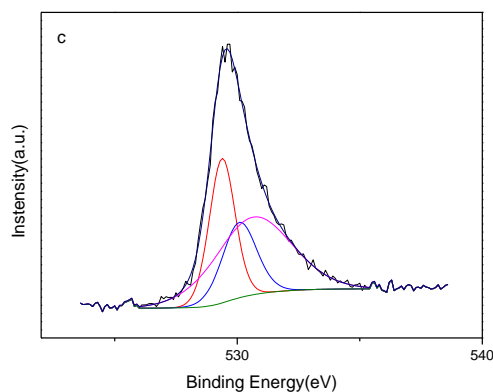
Figure 32 XPS of (a) Cu 2p, (b) Fe 2p, (c) O 1s of CuFe-precursor-800

The main peaks at binding energies of 933.3 eV for Cu $2p_{3/2}$ and 952.9 eV for Cu $2p_{1/2}$ are assign to Cu^{2+} on octahedral sites, while the minor ones at 934.9 eV for Cu $2p_{3/2}$ line and 954.9 eV for Cu $2p_{1/2}$ are Cu^{2+} on tetrahedral coordination sites [34]. The peaks of binding energies at 940.4 eV and 942.8 eV are the satellite peaks of Cu $2p_{3/2}$ and the peak at 961.4 eV is the satellite peaks of Cu $2p_{1/2}$ [35].

The gap between Cu $2p_{3/2}$ (binding energy 934.9 eV) and Cu $2p_{1/2}$ (954.9 eV) levels is 20.0 eV, which is the same value as for the standard spectra of CuO, so this may indicate the presence of CuO. There is a strong dependence of the core-level photoemission spectrum on the type of Cu-O network forming the structure of the compound according to many experimental and theoretical studies [36]. If Cu^{2+} is located in different sites such as octahedral and tetrahedral sites, the types of Cu-O networks are different, for example, it is surrounded by four oxygen atoms in tetrahedral sites and six oxygen atoms in octahedral sites. For Cu-containing compounds, the satellite peaks are quite sensitive to changes in the coordination environment of Cu^{2+} ions [37]. In particular, the ratio of the intensity of the shake-up satellite (I_{sat}) to the intensity of the main Cu $2p_{3/2}$ peak (I_m) is a good indicator of the presence of Cu^{2+} in these samples [38]. Generally, the I_{sat}/I_m ratio decreases as the number of oxygen ions coordinated to a Cu^{2+} ion increases [38]. The I_{sat}/I_m ratio calculated for this sample is 0.54 which is very close to that for the bulk CuO standard (0.56). This leads to the conclusion that there may be a large amount of CuO on the

surface of the catalyst [37], which is consistent with the XRD studies (Figure 25 (b)), where a CuO phase has been already evidenced.

The peak of binding energy of 709.9 eV with a satellite peak at 717.6 eV shows the existence of Fe^{3+}. The doublet peaks of binding energy at 709.9 eV for Fe $2p_{3/2}$ and 722.9 eV for Fe $2p_{1/2}$ are due to Fe^{3+} ions in octahedral sites, the doublet of binding energy of 712.1 eV and for Fe $2p_{3/2}$ and 724.8 eV for Fe $2p_{1/2}$ are due to the Fe^{3+} ions in tetrahedral sites. Compared to the binding energy of peaks of Fe 2p in CoFe-precursor-800，all the binding energies of peaks in CuFe-precursor-800 moved to lower position, which may indicate that the interaction of Cu and Fe is worse than Co and Fe.

There are three peaks of O 1s with binding energy at 529.4 eV, 530.1 and 530.7 eV. The main peak at 529.4 eV is attributed to the contribution of the crystal lattice oxygen.

The percentage of Fe^{3+} in tetrahedral and octahedral sites are calculated according to the results of XPS, 49% and 51% respectively. The ratio of Fe/Cu is 2.16 at the surface of CuFe-precursor-800. The OSPE (octahedral site preference energy) of Cu^{2+} is -63.7 kJ/mol is larger than OSPE of Fe^{3+} (0 kJ/mol), so the Cu^{2+} ions are preferred in octahedral sites, and the $CuFe_2O_4$ spinel is an inverse spinel. It is tetrahedrally distorted [32] because of the effect of large radius of Cu^{2+} (73pm) [39].

III.4.2.3 The XPS analysis of CuCo-precursor-800

The X-ray photoelectron spectroscopy (XPS) measurements for the composite of CuCo-precursor-800 in the Cu 2p, Co 2p and O 1s region are shown in Figure 33.
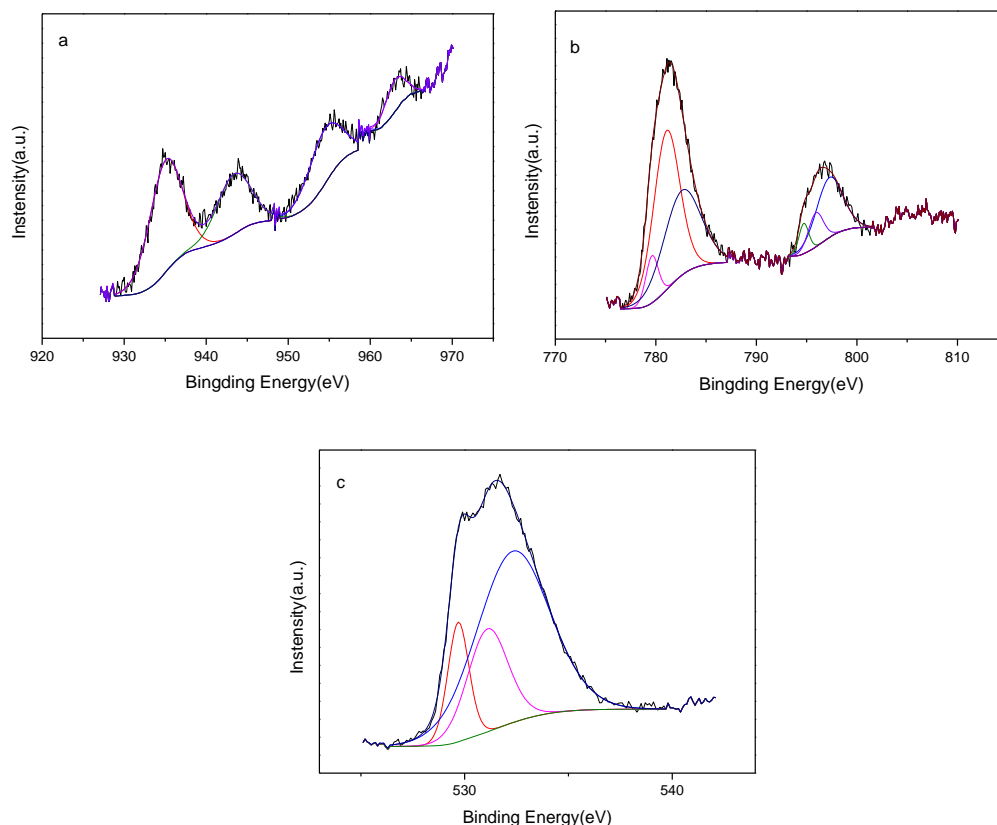
Figure 33 XPS of (a) Cu 2p, (b) Co 2p, (c) O 1s of CuCo-precursor-800

The main Cu $2p_{3/2}$ peak in Figure 33 (a) is the peak of binding energy at 935.1 eV [40], with a typical satellite peak at binding energy 943.4 eV. The I_{sat}/I_m ratio is 0.56 which is similar to the standard bulk CuO. The peak of Cu $2p_{1/2}$ locates at binding energy at 954.5 eV. The width of approximately 19.3 eV between Cu $2p_{3/2}$ and Cu $2p_{1/2}$ peaks is similar to that of the standard spectrum of Cu (20.0 eV) in CuO. This may indicate the existence of CuO in the catalyst and the diffraction lines of CuO have also been observed by XRD. The binding energy at 935.1 eV of Cu 2p may also be ascribed to $Cu(OH)_2$.

The Co 2p spectrum is shown in Figure 33 (b). The Co $2p_{3/2}$ can be fitted into three peaks with binding energy at 779.6 eV, 781.1 eV, and 782.6 eV, with the corresponding Co $2p_{1/2}$ peaks with binding energy at 794.7 eV, and 797.3 eV and 810.1 eV. The two main spin-orbital lines Co $2p_{3/2}$ and Co $2p_{1/2}$, at around 779.6 eV and 794.7 eV with a width of 15.1 eV indicates cobalt ions in Co_3O_4 or $CuCo_2O_4$

spinel as reported in literature [19, 41]. The fitting of Co2p was similar to the results of Biesinger *et al.* [42], in good agreement with the Co_3O_4 reference spectra.

The calculated ratio of Co/Cu is 3.15. The surface is enriched in Co.

The O 1s spectra in Figure 33 (c) can be fitted into three peaks of binding energy at 529.7 eV, 531.1 eV and532.3 eV. The peak at 529.6 eV was referred to the oxide and the peaks at 531.1 eV and 532.2 eV were attributed to the presence either of hydroxyl or of carbonate species [43] or of coordinative unsaturated oxygen [44].

III.4.2.4 The XPS analysis of CuCoFe-precursor-800

The fitting of spectra in the Cu 2p, Co 2p and Fe 2p and O 1s region for CuCoFe-precursor-800 are shown in Figure 34.
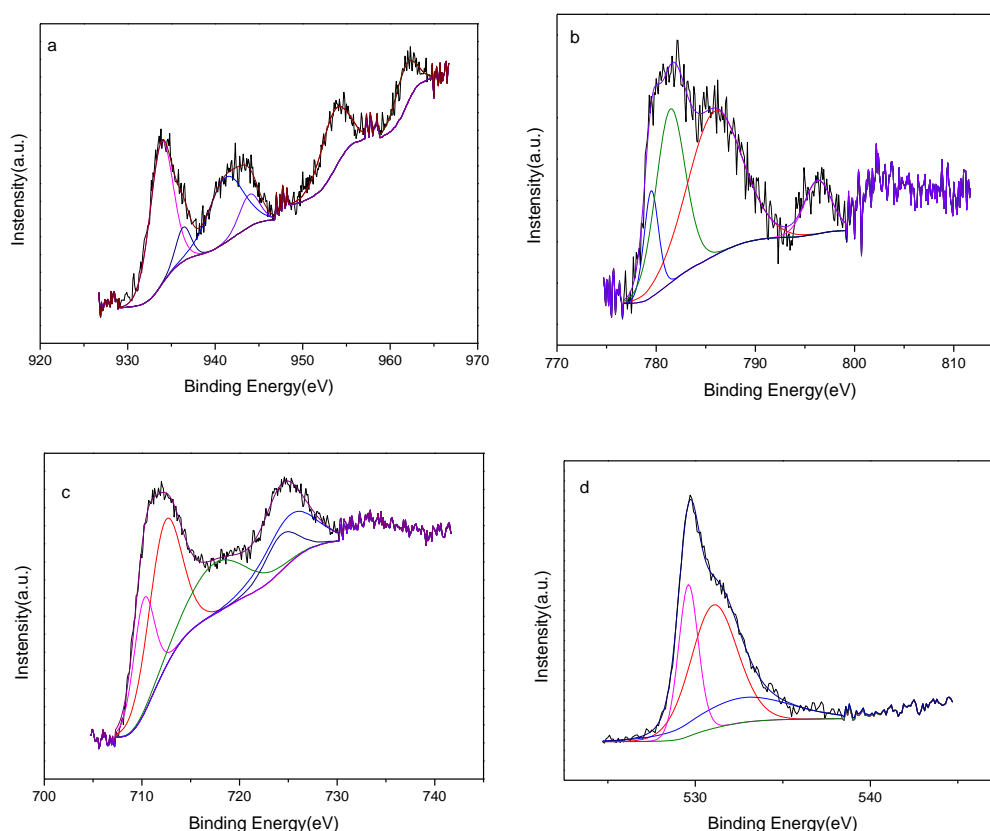
Figure 34 XPS of (a) Cu 2p, (b) Co 2p, (c) Fe 2p, (d) O 1s of CuCoFe-precursor-800

The Figure 34 (a) shows the fitting of Cu 2p, the binding energy of Cu $2p_{3/2}$ at 933.8 eV indicates Cu ions in the $CuFe_2O_4$ structure [45]. The binding energy of Cu

$2p_{3/2}$ at 936.4 eV is corresponding to Cu^{2+} [46], probably in single oxide CuO [47].

For the Co $2p_{3/2}$ in Figure 34 (b), the fitting of the Co $2p_{3/2}$ is also similar to the results of Biesinger *et al.* [42], which indicates the Co ions in spinel phase. The peak of binding energy at 785.9 eV is a satellite peak of binding energy at 781.4 eV [27].

Spectrum of Fe $2p_{3/2}$ is shown in Figure 34 (c), the doublets of Fe $2p_{3/2}$ binding energy at 710.2 eV and Fe $2p_{1/2}$ binding energy at 724.2 eV are due to the Fe^{3+} ions in octahedral sites, while the doublets of Fe $2p_{3/2}$ binding energy at 712.4 eV [28] and Fe $2p_{1/2}$ binding energy at 725.1 eV are due to the Fe^{3+} ions in tetrahedral sites [23]. The ratio of surface Cu/Co/Fe is 1/1.46/3.57, iron ions apparently enrich the surface of the material.

III.4.3 Mössbauer spectroscopy

To calculate more precisely the distribution of iron ions in iron-containing materials, the Mössbauer analysis of CoFe-precursor-800, CuFe-precursor-800 and CoCuFe-precursor-800 (raw materials) were measured at 293K.

III.4.3.1   Mössbauer analysis of CoFe-precursor-800

Figure 35 shows the Mössbauer spectrum of CoFe-precursor-800, and the fit parameters are shown in Table 10. The spectrum is fitted by two sextets with isomer shifts of 0.39 and 0.29 mm/s, the corresponding values of hyperfine magnetic field (H_{hf}) for the two sextets are 51.1 and 48.5 T, respectively. This indicates Fe^{3+} in octahedral (0.3<isomer shift<0.4) and tetrahedral (isomer shift<0.3) sites. The ratio of tetrahedral and octahedral is 4.88. According to this result, the formula is $[Co_{-0.66}Fe_{1.66}]_{tetra}[Co_{1.66}Fe_{0.34}]_{octa}O_4$. The amount of cobalt in tetrahedral sites is negative according to the calculation of Mössbauer results. That is impossible and may be explained by the overestimation of the sextet with isomer shift of 0.29 mm/s

due to strong overlap. The results of XPS showed that there are only a little of cobalt in tetrahedral sites. We can thus propose that the $CoFe_2O_4$ spinel is almost a completely inverse spinel.
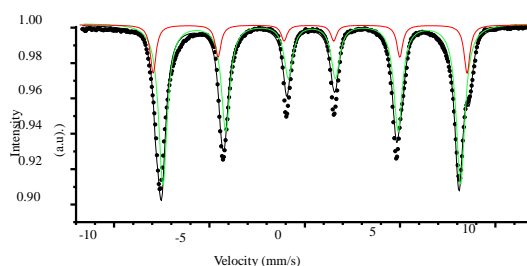
Figure 35 Room-temperature Mössbauer spectrum of CoFe-precursor-800 particles

Table 10 Mössbauer fit parameters for CoFe-precursor-800

Isomer shift δ (mm/s)	Quadrupole splitting ΔE_Q (mm/s)	Hyperfine field B_{Hf} (T)	Relative area (%)	Interpretation
0.39	0.06	51.1	17	Fe^{3+} in spinel, octahedral sites
0.29	-0.01	48.5	83	Fe^{3+} in spinel, tetrahedral sites

III.4.3.2   Mössbauer analysis of CuFe-precursor-800

The overlapped sextets of CuFe-precursor-800 are shown in Figure 36, and the fit parameters are presented in Table 11. The isomer shift values are observed at 0.36 and 0.26 mm/s, which are ascribed to Fe^{3+} ions located at octahedral and tetrahedral sites respectively [48]. The percentage of Fe^{3+} in tetrahedral sites and octahedral sites are 48% and 52% respectively, which is similar to the results calculated by XPS. According to the results of Mössbauer and XPS, it can be sure that the $CuFe_2O_4$ spinel is an inverse spinel. Let's note that the value of the quadrupole splitting of -0.30 is

very different from that obtained for octahedral Fe^{3+} in $CoFe_2O_4$ (Table 4) but is typical of hematite, which is consistent with what was deduced from XRD.
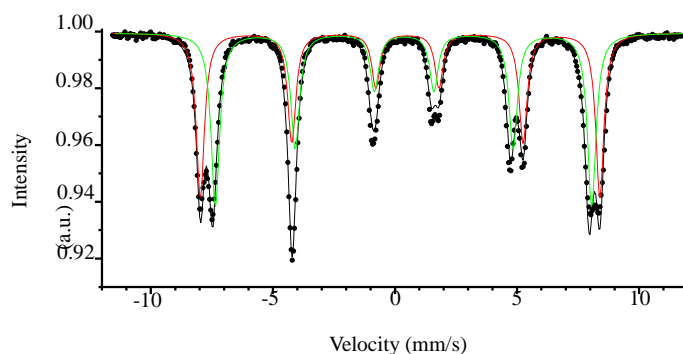
Figure 36 Room-temperature Mössbauer spectrum of CuFe-precursor-800

Table 11 Mössbauer fit parameter for CuFe-precursor-800 particles

Isomer shift δ (mm/s)	Quadruple splitting ΔE_Q (mm/s)	Hyperfine field B_{Hf} (T)	Relative area (%)	Interpretation
0.36	-0.30	50.8	48	Fe^{3+} in octahedral site
0.26	-0.02	47.9	52	Fe^{3+} in tetrahedral site

III.4.3.3 Mössbauer analysis of CuCoFe-precursor-800

The Mössbauer analysis of CuCoFe-precursor-800 was fitted into two sextets in Figure 37, the parameters for the two sextets are shown in Table 12. The isomer shift value at 0.37 and 0.28 mm/s with hyperfine field at 51.2 and 48.5 T is due to Fe^{3+} in octahedral sites and tetrahedral sites, the percentage is 29% and 71% respectively.
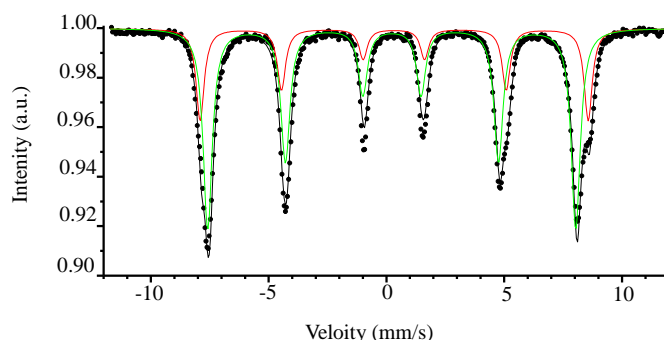
Figure 37 Room-temperature Mössbauer spectrum of CuCoFe-precursor-800 particles

Table 12 Mössbauer fit parameter for CuCoFe-precursor-800 particles

Isomer shift δ (mm/s)	Quadrupole splitting ΔE_Q (mm/s)	Hyperfine field B_{Hf} (T)	Relative area (%)	Interpretation
0.37	0.01	51.2	29	Fe³⁺ in spinel, octahedral sites
0.28	-0.01	48.5	71	Fe³⁺ in spinel, tetrahedral sites

III.4.3.4 Discussion for the results of Mössbauer

The isomer shift (δ) value (between 0.20 to 0.40 mm/s) for both tetrahedral δ_{tet} and octahedral δ_{oct} sites indicate that Fe^{3+} is in high spin state [49]. The values of isomer shift are a little different between the three materials. Isomer shift can be affected by surrounded oxygen. When the distance of the ligand oxygen to iron is shorter in the oxygen polyhedra, the s-electron density at the Fe-nucleus is greater, which results in lowering of isomer shift and *vice versa* [50]. From the results of XRD in Figure 25 (b), the copper iron spinel phase in material CuFe-precursor-800 is a Cu-deficiency spinel, the relative lower isomer shift value of CuFe-precursor-800 may be caused by the distortion of spinel phase. The hyperfine field (H_{hf}) is proportional to magnetization. The magnetic properties can be affected by the particle size, valence

state of the metal ions and the distribution of metal ions in both the tetrahedral and octahedral sites [33]. The low quadruple splitting (ΔE_Q) values for all the three materials are very low, which indicate the overall presence of cubic symmetry [48].

III.4.4 The characterization of materials after partial reduction

In order to detect the properties of these materials before reaction, the characterizations of H_2-TPR, XRD and Mössbauer spectroscopy were performed. All the materials are reduced at 400 °C for 60 min under 10% H_2 in helium.

III.4.4.1 The partial reduction H_2-TPR

After reduction at 400 °C for 60 min, the materials were submitted to a conventional TPR analysis. The consumption of H_2 is shown in Table 13 and compared to the H_2 consumption of raw materials in TPR and theoretical H_2 consumption.

The CoFe-precursor-800 is the most difficult to be reduced, only 36% of spinel was reduced after partial reduction. For CuFe-precursor-800, CuCo-precursor-800 and CuCoFe-precursor-800, the materials were almost totally reduced after 1h at 400 °C.

Table 13 The H_2 consumption of materials after partial reduction compared to the H_2 consumption after total reduction and theoretical H_2 consumption

Materials	Consumption of H_2 (mmol · g^{-1})		Ratio (mmol · $mmol^{-1}$)	
	After partial reduction	After total reduction	Partial H_2/H_2 theoretical	Total H_2/H_2 theoretical
CoFe-precursor-800	6.1	11.6	0.36	0.68
CuFe-precursor-800	16.7	16.9	0.98	1.01
CuCo-precursor-800	16.3	16.6	1.00	1.02
CuCoFe-precursor-800	18.1	18.1	1.07	1.07

Partial reduction: Materials were reduced at 400 °C for 60 min under 10% H_2 in helium

Total reduction: Materials were reduced at 800 °C for 60 min under 10% H_2 in helium

III.4.4.2 The XRD patterns of materials after partial reduction

The XRD patterns of partially reduced materials are presented in Figure 38. There are CoFe alloy and part of $CoFe_2O_4$ spinel in the material of CoFe-precursor-800 after partial reduction. It is consistent with the calculated consumptions of hydrogen presented above: a spinel phase is still present after partial reduction.

For the CuFe-precursor-800 after partial reduction, there are also part of copper iron spinel that exist in the material, even in much lower proportion. There is also metallic iron in the material. Because of the similar diffraction lines of metallic Cu with $FeCu_4$ alloy, it cannot be established clearly if there are metallic copper or alloy in the material after reduction.

There are only metallic Cu and Co after partial reduction of CuCo-precursor-800, which is consistent with partial reduction results. CuCo-precursor-800 can be totally reduced at 400 °C. But the separate metallic phases may not be beneficial for the reaction, the cooperation of two kinds of metals being really important.

For the CuCoFe-precursor-800, there may be CoFe alloy or metallic iron in the material after partial reduction. The metallic Cu or $FeCu_4$ may also be present in the material after reduction. No remaining oxide is detected, as expected from the results of Table 7.
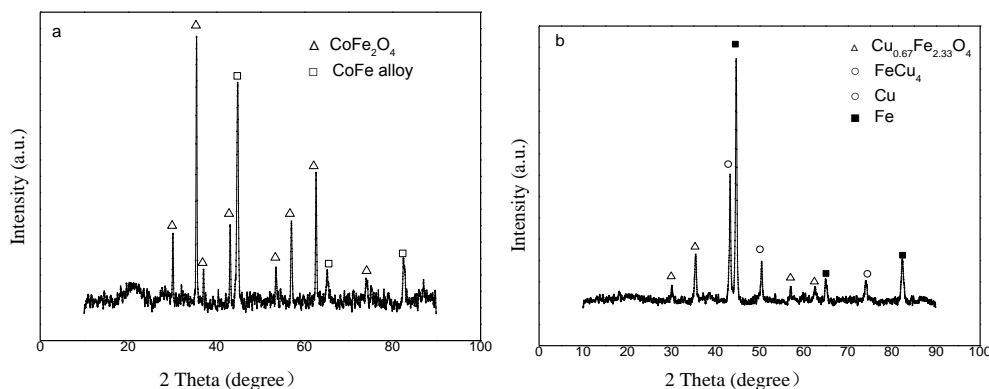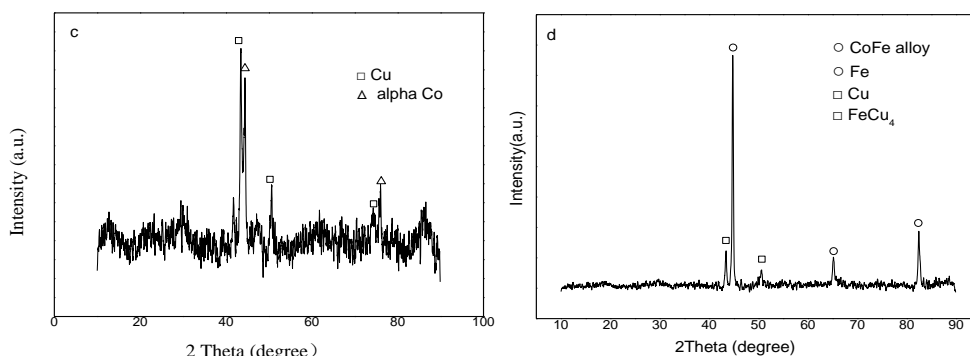
Figure 38 XRD patterns of partial reduction of (a) CoFe-precursor-800, (b) CuFe-precursor-800, (c) CuCo-precursor-800, (d) CuCoFe-precursor-800

III.4.4.3 The Mössbauer spectroscopy of materials after partial reduction

In order to precisely detect the phases that exist in the materials before reaction, the Mössbauer analysis of materials after reduction was performed.

III.4.4.3.1 Mössbauer analysis of CuFe-precursor-800 after partial reduction

The Mössbauer adsorption spectra of CuFe-precursor-800 after partial reduction is fitted into three six lines spectrum in Figure 39. The parameters are shown in Table 14. The values of isomer shift at 0.31 and 0.62 mm/s with magnetic hyperfine field at 49.4 and 45.6 T are attributed to Fe^{3+} in octahedral sites and Fe^{3+} or Fe^{2+} in tetrahedral sites. Metallic Fe can also be detected in the Mössbauer analysis with isomer shift value at 0.00 mm/s and very low magnetic hyperfine field at 33.0 T. The similar magnetic hyperfine field (Hhf) values of iron in A and B sites is because of the A and B subsites magnetically coupled, so the spins at these sites fluctuate in unison [50]. According to the results of Mössbauer analysis, there isn't copper iron alloy.

Combining the results of XRD and Mössbauer analysis, there are part of copper iron spinel and metallic Cu and Fe in the material after reduction.
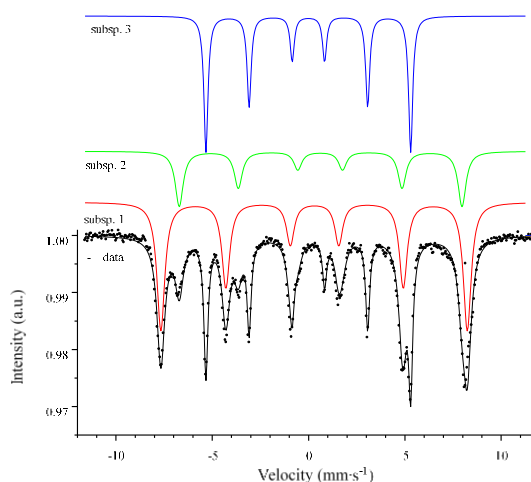
Figure 39 ^{57}Fe Mössbauer adsorption spectra of CuFe-precursor-800 after partial reduction

Table 14 The analysis of Room-temperature Mössbauer spectrum of CuFe-precursor-800 particles after partial reduction

	Isomer shift δ (mm/s)	Quadrupole splitting ΔE_Q (mm/s)	Hyperfine field B_{Hf} (T)	Relative area (%)	Interpretation
Subsp. 1	0.31	-0.03	49.4	50	Fe^{3+} in octahedral sites magnetite
Subsp. 2	0.62	0.02	45.6	22	Fe^{3+} Fe^{2+} in tetrahedral sites magnetite
Subsp. 3	0.00	0.00	33.0	28	Fe in metallic α-iron (ferromagnetic)

III.4.4.3.2 Mössbauer analysis of CuCoFe-precursor-800 after partial reduction

The Mössbauer adsorption spectra of CuCoFe-precursor-800 after reduction is shown in Figure 40 and the results are presented in Table 15. According to the results of Mössbauer analysis, there are still part of spinel in the material, but the amount (26%) is small. Most of iron ions exist in metallic iron and alloy.
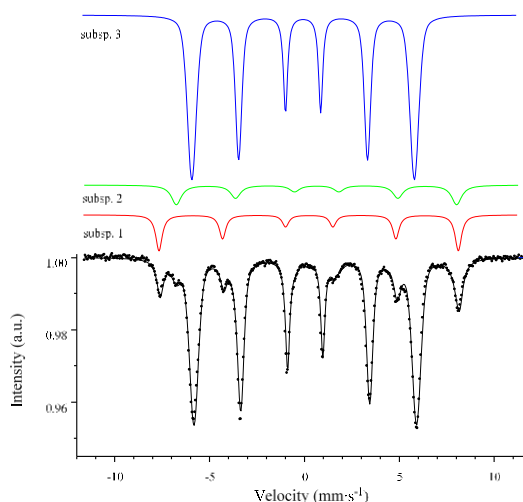
Figure 40 ^{57}Fe Mössbauer adsorption spectra of CuCoFe-precursor-800 after partial reduction

Table 15 The analysis of Room-temperature Mössbauer spectrum of CuCoFe-precursor-800

particles after partial reduction

	Isomer shift δ	Quadrupole splitting $\varDelta E_Q$	Hyperfine field B_{Hf} (T)	Relative area (%)	Interpretation
Subsp. 1	0.29	-0.03	49.0	14	Fe^{3+} in octahedral sites magnetite
Subsp. 2	0.65	0.01	45.9	12	Fe^{3+} Fe^{2+} in tetrahedral sites magnetite
Subsp. 3	0.03	0.00	36.4	74	Fe in metallic α-iron alloy Fe-Co(ferromagnetic)

III.4.4.4 Conclusions for the characterizations of materials after partial reduction

➤ The CoFe-precursor-800 was difficult to be reduced, and there are spinel phase and CoFe alloy in the materials after reduction.

➤ Most of CuFe-precursor-800 can be reduced according to the

calculation of H_2-TPR, and there are copper iron spinel along with metallic copper and iron in the material after reduction.

➢ The CuCo-precursor-800 can be totally reduced at 400 °C for 60 min, and there are only metallic copper and cobalt in the materials after reduction.

➢ From the results of H_2-TPR and XRD, the CuCoFe-precursor-800 can be totally reduced to CoFe alloy or metallic Fe and CuFe alloy or metallic Cu, but it can found a little of spinel phase from the results of Mössbauer analysis.

Because the surface areas of the oxides precursors were very low (only below 3 $m^2.g^{-1}$), the measurement of the metal surface area available after reduction has not been performed

III.5 Catalytic Performance

The four materials are reduced at 400 °C for 60 min before reactions. SiC was used to dilute the catalysts, and its mass is the same as that of catalyst. The catalytic reactions were performed from 250 °C to 350 °C at a total pressure of 50 bar, with a ratio of H_2/CO_2 kept at 3 and the GHSV was 5000 h^{-1} (STP).

The CO_2 and H_2 conversions are presented in Figure 41 (a) and (b). All the four catalysts own good CO_2 and H_2 activities. The CO_2 conversion of catalysts CoFe-precursor-800, CuFe-precursor-800 and CuCo-precursor-800 kept increasing with reaction temperature increase, from 5.5% to 41.9%, 10.1% to 29.8% and 3.8% to 37.6% respectively. The CO_2 conversion of CuCoFe-precursor-800 increased from 3.8% to 26.9% with temperature increased from 250 °C to 300 °C，but the CO_2 conversion (27.1%) almost didn't change when temperature increased to 350 °C. CuFe-precursor-800 has the highest CO_2 conversion at 250 °C, and CuCoFe-precursor-800 owns the highest CO_2 conversion at 300 °C, while the highest

CO_2 conversion at 350 °C is obtained with CoFe-precursor-800.

High reaction temperature also can promote the conversion of H_2. H_2 conversions of all the four catalysts increased a lot (44.4%, 22.4%, 41.8% and 28.9% respectively) with reaction temperature increase from 250 °C to 350 °C. CuFe-precursor-800 owns the highest H_2 conversion (8.8%) at 250 °C, and the H_2 conversions of CoFe-precursor-800, CuCo-precursor-800, and CuCoFe-precursor-800 are similar, around 2%. H_2 conversions of all the four catalysts at 300 °C are around 22%. With temperature increase to 350 °C, H_2 conversions of CoFe-precursor-800 and CuCo-precursor-800 fast increased to 46.4% and 45.3% respectively, meanwhile, H_2 conversions of CuFe-precursor-800 and CuCoFe-precursor-800 only increased to 31.3% and 30.7%.
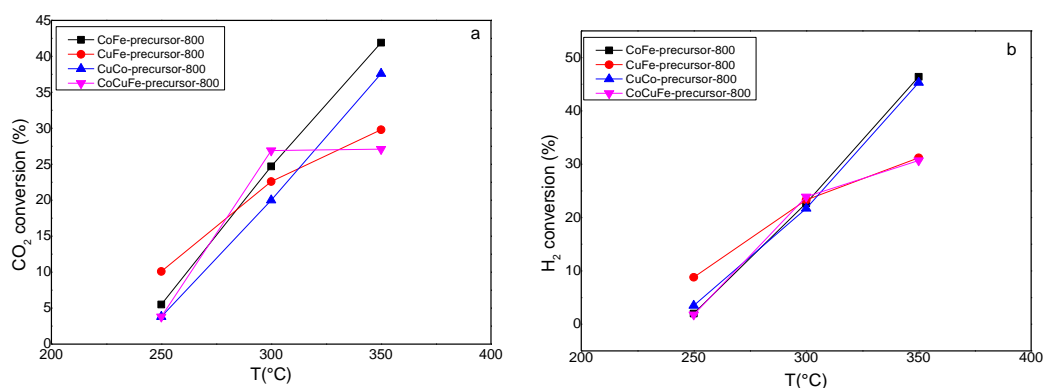
Figure 41 The CO_2 (a) and H_2 (b) conversion of CoFe-precursor-800, CuFe-precursor-800, CuCo-precursor-800 and CuCoFe-precursor-800 at 250 °C, 300 °C and 350 °C

The selectivities are presented in Table 16. The active metals and temperature deeply affect the distribution of products. The effect of temperature on the selectivities and productivities of products (Table 16) are a little different for the four catalysts.

For the alcohols, the selectivities of total alcohols and methanol decreased a lot when reaction temperature increased. CoFe-precursor-800 owns the highest selectivities of total alcohols (25.1%) and methanol (24.3%) at 250 °C, but the selectivities decreased to 2.8% (total alcohols) and 2.0% (methanol) at 350 °C. This

also happened to catalyst CuFe-precursor-800 and CuCo-precursor-800, the selectivities of total alcohols decreased from 15.0% to 4.8% and 19.4% to 0.9% respectively with temperature increased from 250 °C to 350 °C. CuCoFe-precursor-800 is a little different, although the selectivities of total alcohols and methanol decreased from 250 °C to 300 °C (23.2% to 6.7% and 21.7% to 4.7%)，they increased a little when temperature increased to 350 °C. The highest productivities of total alcohols and methanol happened at 300 °C except for CuCoFe-precursor-800, for which it happened at 350 °C.

The tendency of selectivities and productivities of higher alcohols is the same between catalysts CoFe-precursor-800 and CuCo-precursor-800. The highest selectivities is at 300 °C, 1.6% and 0.5% respectively. The behavior of CuFe-precursor-800 and CuCoFe-precursor-800 is similar, the highest selectivities of higher alcohols are at 350 °C, 2.6% and 2.8% respectively. The CuFe-precursor-800 owns the highest higher alcohols productivities (11.2 $g \cdot g_{cata}^{-1} \cdot h^{-1}$) at 350 °C. It can also be found that at iso temperature the selectivities and productivities of higher alcohols are higher in the reactions with copper in the catalysts.

The tendency of CO selectivity with temperature was different for the four kinds of catalysts. For CuFe-precursor-800, the selectivity of CO kept increasing from 250 °C to 350 °C (from 13.9% to 18.8%). For CuCo-precursor-800, selectivity of CO also increased from 10.0% to 12.8%, but for CoFe-precursor-800, the selectivity of CO kept decreasing from 46.1% to 5.6%, when there are Cu, Co and Fe in the catalyst at the same time, the tendency was not changed with temperature.

The change of selectivity to methane with temperature is similar between catalyst CoFe-precursor-800 and CuCoFe-precursor-800. The highest selectivity happened at 300 °C, 60.8% and 45.6% respectively, but for CoFe-precursor-800, the highest productivity (209.6 $g \cdot g_{cata}^{-1} \cdot h^{-1}$) of methane is at 350 °C, and for CuCoFe-precursor-800, the productivity at 300 °C (110.8 $g \cdot g_{cata}^{-1} \cdot h^{-1}$) is the highest. The tendency of methane formation in the reaction with CuFe-precursor-800 and

CuCo-precursor-800 is totally opposite, the highest selectivity of methane happened at 250 °C with CuFe-precursor-800 as catalyst (40.4%) and at 350 °C with CuCo-precursor-800 as catalyst (84.4%).

For the C$_{2+}$ hydrocarbons, when CoFe-precursor-800 and CuCoFe-precursor-800 was used in the reacions, the selectivities increased to 28.7% and 15.4% respectively with temperature increase from 250 °C to 350 °C. The selectivities to C$_{2+}$ hydrocarbons are very low (less than 3.0%) with CoCu-precursor-800 as catalyst, and it decreased when temperature increased. For the CoCuFe-precursor-800, 300 °C is the best temperature for the synthesis of C$_{2+}$ hydrocarbons, which is different from all the others catalysts.

Comparing the four catalysts, for CuCo-precursor-800, more than 95% of products is C$_1$ products (methanol, methane and CO). CuFe-precursor-800 has the highest selectivities to C$_{2+}$ hydrocarbons at all the three temperature, and it also has relative high selectivities to higher alcohols.

The selectivities to hydrocarbons and CO can directly affect the conversions of CO$_2$ and H$_2$. For example catalyst CuCoFe-precursor-800, the selectivities to hydrocarbons decreased a lot when temperature increased from 300 °C to 350 °C and selectivity to CO increased a little, so the conversion of CO$_2$ almost doesn't change, and conversion of H$_2$ only increased a little from 300 °C to 350 °C. To the contrary, for catalyst CoFe-precursor-800 and CuCo-precursor-800, the selectivities to hydrocarbons kept increasing from 250 °C to 350 °C, the conversions of CO$_2$ and H$_2$ also sharply increased.

Table 16 The selectivities to alcohols, methanol, higher alcohols, hydrocarbons, methane, hydrocarbon C_{2-5}, hydrocarbon C_{5+}, CO and other oxygen for the

CoFe-precursor-800, CoFe-precursor-800, CuCo-precursor-800, and CuCoFe-precursor-800 at 250 °C, 300 °C and 350 °C under 50bar

Catalysts	T (°C)	CO_2 Conversion (%)	Selectivities (%)								
			Alcohols (Total)	Methanol	Higher alcohols	Hydrocarbons (Total)	CH_4	Hydrocarbons C_{2-5}	Hydrocarbons C_{5+}	CO	Other oxygenates
CoFe-precursor-800	250 °C	5.5	25.1	24.3	0.8	28.8	20.6	8.2	0.0	46.1	0.0
	300 °C	22.7	9.6	8.0	1.6	75.0	60.8	13.9	0.2	15.5	0.0
	350 °C	41.9	2.8	2.0	0.8	91.7	54.0	36.9	0.4	5.6	0.0
CuFe-precursor-800	250 °C	10.1	15.0	13.1	1.9	71.1	40.2	30.1	0.8	13.9	0.0
	300 °C	22.6	9.2	6.8	2.4	76.2	35.0	39.3	1.3	14.6	0.2
	350 °C	29.8	4.8	2.2	2.6	75.7	30.0	43.6	1.7	18.8	0.3
CuCo-precursor-800	250 °C	3.8	19.4	19.1	0.3	70.6	67.6	3.0	0.0	10.0	0.0
	300 °C	20.0	10.4	9.9	0.5	78.1	76.1	2.0	0.0	11.5	0.0
	350 °C	37.6	0.9	0.8	0.1	86.3	84.4	1.9	0.0	12.8	0.0
CoCuFe-precursor-800	250 °C	3.8	23.2	21.7	1.5	27.8	17.7	10.1	0.0	48.9	0.0
	300 °C	26.9	6.7	4.7	2.0	82.5	45.6	35.9	0.7	10.8	0.1
	350 °C	27.1	7.6	4.8	2.8	69.4	43.4	25.5	0.3	22.8	0.1

Table 17 The productivities of alcohols, methanol , higher alcohols, hydrocarbons, methane, hydrocarbon C_{2-5}, hydrocarbon C_{5+},CO and other oxygen for the CoFe-precursor-800, CoFe-precursor-800, CuCo-precursor-800, and CuCoFe-precursor-800 at 250 °C, 300 °C and 350 °C

Catalysts	T (°C)	CO₂ Conversion (%)	Productivities (g·g$_{cata}^{-1}$·h^{-1})								
			Alcohols (Total)	Methanol	Higher alcohols	Hydrocarbons (Total)	CH₄	Hydrocarbons C_{2-5}	Hydrocarbons C_{5+}	CO	Other oxygenates
CoFe-precursor-800	250 °C	5.5	43.6	43.0	0.6	14.2	10.4	3.8	0.0	40.7	0.0
	300 °C	22.7	68.5	63.4	5.2	168.0	138.2	29.4	0.4	61.3	0.0
	350 °C	41.9	31.4	27.0	4.4	344.5	209.6	133.2	1.6	37.7	0.3
CuFe-precursor-800	250 °C	10.1	51.0	48.2	2.8	72.2	42.2	29.2	0.8	25.4	0.2
	300 °C	22.6	62.7	54.8	7.9	167.5	80.5	83.7	3.3	58.7	0.7
	350 °C	29.8	34.5	23.3	11.2	217.4	90.0	121.2	6.2	98.3	0.1
CuCo-precursor-800	250 °C	3.8	19.7	19.5	0.1	20.6	19.8	0.8	0.0	5.1	0.0
	300 °C	20.0	53.5	52.4	1.1	118.5	115.7	2.8	0.0	30.6	0.0
	350 °C	37.6	7.8	7.6	0.2	215.5	211.0	4.5	0.0	55.8	0.0
CoCuFe-precursor-800	250 °C	3.8	28.0	27.2	0.8	9.7	6.4	3.4	0.0	30.6	0.0
	300 °C	26.9	47.5	40.7	6.8	193.5	110.8	80.9	1.9	45.7	0.5
	350 °C	27.1	52.2	42.2	10.0	168.0	107.9	59.1	0.9	99.2	0.3

III.6 The XRD patterns of catalysts after reaction

The XRD patterns of the different catalysts after reaction are shown in Figure 42.
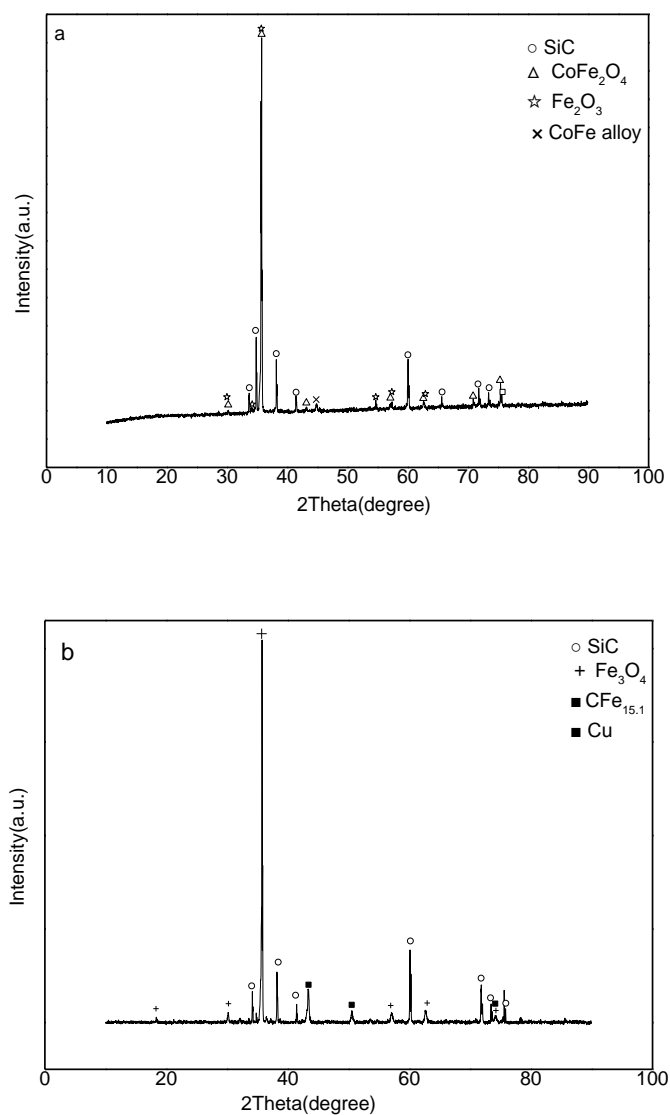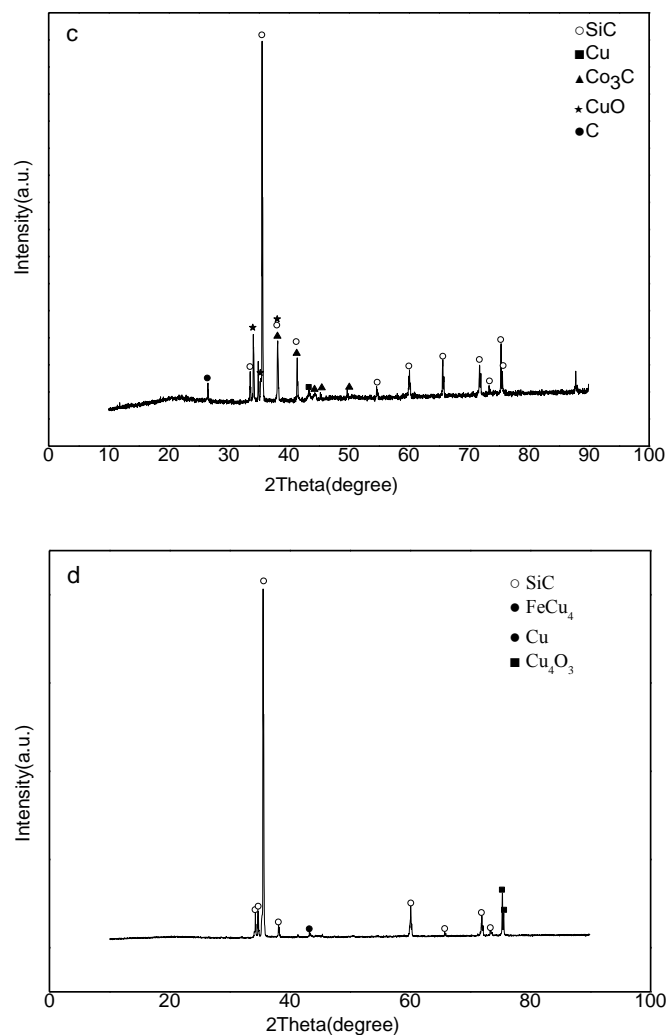
Figure 42 The XRD profiles of catalysts (a) CoFe-precursor-800 (b) CuFe-precursor-800 (c) CuCo-precursor-800 (d) CoCuFe--precursor-800 after reactions

Compared to the XRD patterns of CoFe-precursor-800 before reaction and after reaction, except for part of spinel $CoFe_2O_4$ and CoFe alloy, only Fe_2O_3 appeared in the catalyst, iron carbide and cobalt carbide were not formed.

Iron carbide was formed in the catalyst CuFe-precursor-800 after reaction. Fe_3O_4 instead of copper iron spinel phase appeared and metallic copper was still present in the catalyst.

For catalyst CuCo-precursor-800, coke deposition apparently appeared on the surface. Cobalt carbide was formed in this catalyst after reaction.

Compared to the XRD patterns of CuCoFe-precursor-800 before reaction and after reaction, only metallic copper was oxidized.

III.7 Discussions

For catalyst CoFe-precursor-800, the conversion of CO_2 and H_2 kept increasing with temperature. The selectivities to C_{2+} hydrocarbons also increased with increasing reaction temperature. From the results of XRD patterns in Figure 38 (a), there are part of cobalt iron spinel and alloy in the catalyst after partial reduction. The remaining spinel oxide can helps the metal dispersion. More, the oxygen ions in the vacancies of partially reduced ferrite can promote the decomposition of CO_2 and generate carbon. The carbon can react with hydrogen and produce methane and hydrocarbons [62]. The calculation of Liu [63] found that the activation of CO_2 involved a charge transfer from metal surface to the CO_2 moiety. The CO_2 is preferred to adsorb on Fe surface, and the Co also showed low CO_2 decomposition barriers for CO_2 dissociation. So catalyst CoFe-precursor-800 owns high CO_2 and H_2 conversions.

The main products of CuCo-precursor-800 as catalyst precursor were C1 products: methanol, CO and methane. The large amount of methanol and methane may be caused by the slow CO_2 adsorption rate and the bad cooperation between the two active sites (Co and Cu). From the results of XRD patterns in Figure 38 (c), only metallic Co and Cu existed in the catalyst after reduction. Co is able to break -C-O bond and CH_4 will be obtained, while Cu doesn't dissociate -C-O and insert it into the carbon chain and methanol will be obtained. The highest selectivity to methane may also cause the coke deposition on the surface of catalyst in Figure 42 (c).

When Cu and Fe exist together in the structure, the selectivities to long-chain hydrocarbons (C_{2+} hydrocarbons) and higher alcohols were apparently higher than for CoFe-precursor-800 and CuCo-precursor-800 as catalysts. More, the selectivities to long-chain hydrocarbons (C_{2+}), higher alcohols and CO apparently increased with temperature increased, and the formation of methane and methanol is decreased. According to the mechanism of high alcohols synthesis (HAS) reaction, the CO_2 first needs to be converted into CO by RWGS reaction, then according to the CO insertion mechanism [64], the carbon chain increases then insert -CO to obtain alcohols. The good cooperation of CuFe alloy (Figure 38 (b)) is really important for the cooperation

of two active sites and the HAS synthesis, the CuFe-precursor-800 is the most potential catalyst which can be used to enhance the selectivity to higher alcohols.

According to the XRD profiles in Figure 42(b) of CuFe$_2$O$_4$ after reaction, there are Fe$_3$O$_4$, FeC$_{15.1}$ and metallic Cu in the catalyst. There was no Cu oxide in the catalyst, because the oxygen atoms produced on copper surface can spillover to iron surface, especially on the surface of metal/oxide mixture catalyst, resulting in the extensive oxidation and protected itself from oxides during the reaction [65].

There are same amounts of Cu and Co in the CoCuFe-precursor-800 structure, and the tendency towards hydrocarbons and CO with temperature was totally inversed. As for the alcohols, high temperature is beneficial for the synthesis of higher alcohols.

For all the reactions, methane is a main product, the maximum selectivity to methane is even as high as 84.4%. The methanation of CO$_2$ is the thermodynamically most favorable reaction, so there is a lot of methane in the products. In order to obtain the C$_{2+}$ hydrocarbons or alcohols, the most important property of catalyst is to inhibit the synthesis of methane. Comparing the four catalyst, CuFe-precursor-800 owns the smallest selectivity to methane at high temperature. Catalysts with cobalt are widely used in FT synthesis, owing to the high performance to cost ratio. When the feeding gas shifts from synthesis gas to the gas mixture of CO$_2$ and H$_2$, cobalt performs as a methanation catalyst rather than acting as an FT catalyst [66-69]. Mixed Fe/Co catalysts have also exhibited low selectivity to the desired hydrocarbons [70]. Akin *et al.* also have the similar results when the Co/Al$_2$O$_3$ catalyst was used for CO$_2$ hydrogenation, over 70 mol% of products is methane [69]. They proposed that the conversion of CO and CO$_2$ occurs via different reaction pathways: the former involving mainly species of C-H and O-H produced from hydrogenation, the latter involving surface-bound intermediates of H-C-O and O-H [71]. The slow CO$_2$ adsorption rate on the surface because of stability of CO$_2$ molecules thermodynamically and chemically may also lead to methane formation and a decrease in chain growth. This favors the hydrogenation of surface-adsorbed intermediates. So in order to inhibit the produce of methane, it's better to choose

catalysts without cobalt.

For all the results, when temperature increased, the selectivities to methanol and higher alcohols decreased. This is similar to the research of Fink *et al.* [72, 73], he also found that the equilibrium concentration of methanol in the reaction mixture decreases with increasing temperature and the selectivity to higher alcohols is therefore enhanced at higher temperatures (280-300 °C) in CO hydrogenation to synthesis higher alcohols over Cu/ZnO catalyst. The rate of reaction to linear higher alcohols is independent on the methanol concentration in the reaction mixture, whereas the rate of formation of branched higher alcohols increases with the methanol concentration.

The CO was produced by RWGS reaction. There are two models to explain this mechanism: redox mechanism and formate decomposition mechanism. The concept of oxidation and reduction cycle was suggested in the redox mechanism. CO_2 oxidized metallic Cu and generated CO. Cu (I) was reduced to metallic Cu by H_2 and formed H_2O [65]. The formate decomposition mechanism suggested that CO arose from the decomposition of formate intermediate ($HCOO^*$) which were formed by H_2 association with CO_2, and then $HCOO^*$ decomposed to CO and OH^* and copper could be oxidized by OH^* species [65, 74]. The formate intermediate is the dominant intermediate to form CO in this process [74]. When temperature increases, the surface functional groups are not stable, so the selectivity to CO increased with temperature.

Comparing the results of CoFe-precursor-800, CuFe-precursor-800 and CoCuFe-precursor-800 with CuCo-precursor-800, it can be found that Fe irons are really important for the conversion of CO_2, and Cu worked well to promote the selectivity to long-chain hydrocarbons and higher alcohols. The more Cu in the structure, the more long-chain hydrocarbons and higher alcohols at the same temperature.

Combined the selectivities and productivities of all the products in Table 16 and Table 17, it can be found that low reaction temperature is beneficial for the synthesis of methanol and high reaction temperature is good for the synthesis of higher alcohols. The synthesis of C_{2+} hydrocarbons depends on both the property of catalysts and

reaction temperature.

CuFe-precursor 800 is the most suitable catalyst for the synthesis of higher alcohols, because of the higher selectivity and productivity to higher alcohols. It also can inhibit the selectivity to methane. CoFe-precursor-800 can be used as hydrocarbons synthesis catalyst. CuCo-precursor-800 is beneficial for the synthesis of single-carbon products.

III.8 Conclusions

In this part, the four kinds of catalysts (CoFe-precursor-800, CuFe-precursor-800, CuCo-precursor-800 and CuCoFe-precursor-800) were synthesized and characterized.

The Cu, Co and Fe elements work differently in different environment. CoFe-precursor-800 catalyst is more suitable for the synthesis of hydrocarbons especially C$_{2+}$ hydrocarbons. CuCo-precursor-800 is better to be used for the synthesis of methane and methanol, which may be caused by the separation of metallic Cu and Co (there is no alloy in the CuCo-precursor-800 after reduction). CuFe-precursor is beneficial for the synthesis of C$_{2+}$ hydrocarbons and higher alcohols. In the CO$_2$ hydrogenation, Co acts as a methanation catalyst rather than acting as a FT catalyst, because of the different reaction mechanism between CO hydrogenation and CO$_2$ hydrogenation. In order to inhibit the formation of methane, it is better to choose catalysts without Co in the CO$_2$ hydrogenation reaction.

III.9 References

[1] J.C. Vargas, S. Libs, A.C. Roger, A. Kiennemann, Study of Ce-Zr-Co fluorite-type oxide as catalysts for hydrogen production by steam reforming of bioethanol, Catalysis Today, 107-08 (2005) 417-425.

[2] N. Sahli, C. Petit, A.C. Roger, A. Kiennemann, S. Libs, M.M. Bettahar, Ni catalysts from $NiAl_2O_4$ spinel for CO_2 reforming of methane, Catalysis Today, 113 (2006) 187-193.

[3] D.W. Jeong, W.J. Jang, A. Jha, W.B. Han, K.W. Jeon, S.H. Kim, H.S. Roh, The Effect of Metal on Catalytic Performance Over MFe_2O_4 Catalysts for High Temperature Water-Gas Shift Reaction, Journal of Nanoelectronics and Optoelectronics, 10 (2015) 530-534.

[4] T.P. Braga, B.M.C. Sales, A.N. Pinheiro, W.T. Herrera, E. Baggio-Saitovitch, A. Valentini, Catalytic properties of cobalt and nickel ferrites dispersed in mesoporous silicon oxide for ethylbenzene dehydrogenation with CO_2, Catalysis Science & Technology, 1 (2011) 1383-1392.

[5] E. Manova, D. Paneva, B. Kunev, C. Estournes, E. Riviere, K. Tenchev, A. Leaustic, I. Mitov, Mechanochemical synthesis and characterization of nanodimensional iron-cobalt spinel oxides, Journal of Alloys and Compounds, 485 (2009) 356-361.

[6] E. Manova, T. Tsoncheva, C. Estournes, D. Paneva, K. Tenchev, I. Mitov, L. Petrov, Nanosized iron and iron-cobalt spinel oxides as catalysts for methanol decomposition, Appl Catal A Gen, 300 (2006) 170-180.

[7] F. Kenfack, H. Langbein, Influence of the temperature and the oxygen partial pressure on the phase formation in the system Cu-Fe-O, Crystal Research and Technology, 39 (2004) 1070-1079.

[8] R. Koferstein, T. Walther, D. Hesse, S.G. Ebbinghaus, Crystallite-growth, phase transition, magnetic properties, and sintering behaviour of nano-$CuFe_2O_4$ powders prepared by a combustion-like process, Journal of Solid State Chemistry, 213 (2014) 57-64.

[9] V.A.M.B.a. J.Klerk, Dilatometric investigation of the phase transition in copper ferrite, Thermochim Acta, 18 (1977) 287-294.

[10] Q. Yang, H. Choi, S.R. Al-Abed, D.D. Dionysiou, Iron-cobalt mixed oxide nanocatalysts: Heterogeneous peroxymonosulfate activation, cobalt leaching, and ferromagnetic properties for environmental applications, Appl Catal B-Environ, 88 (2009) 462-469.

[11] E. Amini, M. Rezaei, M. Sadeghinia, Low temperature CO oxidation over mesoporous $CuFe_2O_4$ nanopowders synthesized by a novel sol-gel method, Chinese Journal of Catalysis, 34 (2013) 1762-1767.

[12] J.H. Lee, K.H. Reddy, J.S. Jung, E.-H. Yang, D.J. Moon, Role of support on higher alcohol synthesis from syngas, Applied Catalysis A: General, 480 (2014) 128-133.

[13] L.Y. Dolgykh, I.L. Stolyarchuk, L.A. Staraya, I.V. Vasylenko, Y.I. Pyatnitsky, P.E. Strizhak, Catalytic Properties of $CuFe_2O_4$ in Steam Reforming of Ethanol, Theoretical and Experimental Chemistry, 51 (2015) 230-235.

[14] A.J. Marchi, J.I. Dicosimo, C.R. Apesteguia, Effect of the Preparation Conditions on the Reducibility of Cu-Co Based Oxides, Catalysis Today, 15 (1992) 383-394.

[15] B. Tomic-Tucakovic, D. Majstorovic, D. Jelic, S. Mentus, Thermogravimetric study of the kinetics of Co_3O_4 reduction by hydrogen, Thermochim Acta, 541 (2012) 15-24.

[16] D. Potoczna-Petru, L. Kepinski, Reduction study of Co_3O_4 model catalyst by electron microscopy, Catalysis Letters, 73 (2001) 41-46.

[17] H.Y. Lin, Y.W. Chen, The mechanism of reduction of cobalt by hydrogen, Materials Chemistry and Physics, 85 (2004) 171-175.

[18] N.M. Bertero, A.F. Trasarti, B. Moraweck, A. Borgna, A.J. Marchi, Selective liquid-phase hydrogenation of citral over supported bimetallic Pt-Co catalysts, Appl Catal A Gen, 358 (2009) 32-41.

[19] Z.Y. Tian, H. Vieker, P.M. Kouotou, A. Beyer, In situ characterization of Cu-Co oxides for catalytic application, Faraday Discuss, 177 (2015) 249-262.

[20] P. Paknahad, M. Askari, M. Ghorbanzadeh, Characterization of nanocrystalline $CuCo_2O_4$ spinel prepared by sol-gel technique applicable to the SOFC interconnect coating, Appl Phys A-Mater, 119 (2015) 727-734.

[21] E. Alizadeh-Gheshlaghi, B. Shaabani, A. Khodayari, Y. Azizian-Kalandaragh, R. Rahimi, Investigation of the catalytic activity of nano-sized CuO, Co_3O_4 and $CuCo_2O_4$ powders on thermal decomposition of ammonium perchlorate, Powder Technology, 217 (2012) 330-339.

[22] J.L. Gautier, E. Trollund, E. Rios, P. Nkeng, G. Poillerat, Characterization of thin $CuCo_2O_4$ films prepared by chemical spray pyrolysis. Study of their electrochemical stability by ex situ spectroscopic analysis, Journal of Electroanalytical Chemistry, 428 (1997) 47-56.

[23] Z.P. Zhou, Y. Zhang, Z.Y. Wang, W. Wei, W.F. Tang, J. Shi, R. Xiong, Electronic structure studies of the spinel $CoFe_2O_4$ by X-ray photoelectron spectroscopy, Applied Surface Science, 254 (2008) 6972-6975.

[24] B.B. Tope, R.J. Balasamy, A. Khurshid, L.A. Atanda, H. Yahiro, T. Shishido, K. Takehira, S.S. Al-Khattaf, Catalytic mechanism of the dehydrogenation of ethylbenzene over Fe-Co/Mg(Al)O derived from hydrotalcites, Appl Catal A Gen, 407 (2011) 118-126.

[25] A. Stoyanova, G. Borisov, E. Lefterova, E. Slavcheva, Oxygen evolution on Ebonex-supported Pt-based binary compounds in PEM water electrolysis, International Journal of Hydrogen Energy, 37 (2012) 16515-16521.

[26] R.R. Rajaram, P.A. Sermon, Adsorption and Catalytic Properties of $Co_xFe_{3-X}O_4$ Spinels .1. Preparation and Characterization of Precursors to Ammonia-Synthesis Catalysts, J Chem Soc Farad T 1, 81 (1985) 2577-2591.

[27] H.L. Yuan, Y.Q. Wang, S.M. Zhou, L.S. Liu, X.L. Chen, S.Y. Lou, R.J. Yuan, Y.M. Hao, N. Li, Low-Temperature Preparation of Superparamagnetic $CoFe_2O_4$ Microspheres with High Saturation Magnetization, Nanoscale Res Lett, 5 (2010) 1817-1821.

[28] R.S. Yadav, J. Havlica, J. Masilko, L. Kalina, M. Hajduchova, V. Enev, J. Wasserbauer, I. Kuritka, Z. Kozakova, Structural, Cation Distribution, and Magnetic

Properties of $CoFe_2O_4$ Spinel Ferrite Nanoparticles Synthesized Using a Starch-Assisted Sol-Gel Auto-Combustion Method, J Supercond Nov Magn, 28 (2015) 1851-1861.

[29] P.N. Anantharamaiah, P.A. Joy, Enhancing the strain sensitivity of $CoFe_2O_4$ at low magnetic fields without affecting the magnetostriction coefficient by substitution of small amounts of Mg for Fe, Physical Chemistry Chemical Physics, 18 (2016) 10516-10527.

[30] S. Nappini, E. Magnano, F. Bondino, I. Pis, A. Barla, E. Fantechi, F. Pineider, C. Sangregorio, L. Vaccari, L. Venturelli, P. Baglioni, Surface Charge and Coating of $CoFe_2O_4$ Nanoparticles: Evidence of Preserved Magnetic and Electronic Properties, J Phys Chem C, 119 (2015) 25529-25541.

[31] W.P. Wang, H. Yang, T. Xian, J.L. Jiang, XPS and Magnetic Properties of $CoFe_2O_4$ Nanoparticles Synthesized by a Polyacrylamide Gel Route, Mater Trans, 53 (2012) 1586-1589.

[32] R.G. Burns, Mineralogical applications of crystal field theory, Cambridge University Press, 1993.

[33] S.R. Naik, A.V. Salker, S.M. Yusuf, S.S. Meena, Influence of Co^{2+} distribution and spin-orbit coupling on the resultant magnetic properties of spinel cobalt ferrite nanocrystals, Journal of Alloys and Compounds, 566 (2013) 54-61.

[34] C. Reitz, C. Suchomski, J. Haetge, T. Leichtweiss, Z. Jaglicic, I. Djerdj, T. Brezesinski, Soft-templating synthesis of mesoporous magnetic $CuFe_2O_4$ thin films with ordered 3D honeycomb structure and partially inverted nanocrystalline spinel domains, Chemical Communications, 48 (2012) 4471-4473.

[35] W. Gao, Y.F. Zhao, J.M. Liu, Q.W. Huang, S. He, C.M. Li, J.W. Zhao, M. Wei, Catalytic conversion of syngas to mixed alcohols over CuFe-based catalysts derived from layered double hydroxides, Catalysis Science & Technology, 3 (2013) 1324-1332.

[36] T. Boske, K. Maiti, O. Knauff, K. Ruck, M.S. Golden, G. Krabbes, J. Fink, T. Osafune, N. Motoyama, H. Eisaki, S. Uchida, Cu-O network-dependent core-hole screening in low-dimensional cuprate systems: A high-resolution x-ray photoemission

study, Phys Rev B, 57 (1998) 138-141.

[37] I. Nedkov, R.E. Vandenberghe, T. Marinova, P. Thailhades, T. Merodiiska, I. Avramova, Magnetic structure and collective Jahn-Teller distortions in nanostructured particles of $CuFe_2O_4$, Applied Surface Science, 253 (2006) 2589-2596.

[38] B.E. Goodby, J.E. Pemberton, XPS Characterization of a Commercial $Cu/Zno/Al_2O_3$ Catalyst - Effects of Oxidation, Reduction, and the Steam Reformation of Methanol, Appl Spectrosc, 42 (1988) 754-760.

[39] J. Wang, S. Kirihara, R. Narayan, P. Colombo, Advances in Bioceramics and Porous Ceramics VIII: Ceramic Engineering and Science Proceedings, Volume 36, John Wiley & Sons, 2015.

[40] P.P. Xu, J.J. Liu, T. Liu, K. Ye, K. Cheng, J.L. Yin, D.X. Cao, G.L. Wang, Q. Li, Preparation of binder-free $CuO/Cu_2O/Cu$ composites: a novel electrode material for supercapacitor applications, Rsc Adv, 6 (2016) 28270-28278.

[41] W.F. Wei, W.X. Chen, D.G. Ivey, Rock salt-spinel structural transformation in anodically electrodeposited Mn-Co-O nanocrystals, Chemistry of Materials, 20 (2008) 1941-1947.

[42] M.C. Biesinger, B.P. Payne, A.P. Grosvenor, L.W.M. Lau, A.R. Gerson, R.S. Smart, Resolving surface chemical states in XPS analysis of first row transition metals, oxides and hydroxides: Cr, Mn, Fe, Co and Ni, Applied Surface Science, 257 (2011) 2717-2730.

[43] A.R. Gonzalezelipe, J.P. Espinos, A. Fernandez, G. Munuera, Xps Study of the Surface Carbonation Hydroxylation State of Metal-Oxides, Applied Surface Science, 45 (1990) 103-108.

[44] D. Barreca, C. Massignan, S. Daolio, M. Fabrizio, C. Piccirillo, L. Armelao, E. Tondello, Composition and microstructure of cobalt oxide thin films obtained from a novel cobalt(II) precursor by chemical vapor deposition, Chemistry of Materials, 13 (2001) 588-593.

[45] T. Suponik, A. Winiarski, J. Szade, Species Formed on Iron Surface during Removal of Copper Ions from Aqueous Solutions, Physicochem Probl Mi, 51 (2015) 731-743.

[46] F. Alonso, Y. Moglie, G. Radivoy, M. Yus, Click chemistry from organic halides, diazonium salts and anilines in water catalysed by copper nanoparticles on activated carbon, Org Biomol Chem, 9 (2011) 6385-6395.

[47] F.W. Chang, H.C. Yang, L.S. Roselin, W.Y. Kuo, Ethanol dehydrogenation over copper catalysts on rice husk ash prepared by ion exchange, Appl Catal A Gen, 304 (2006) 30-39.

[48] N.S. Gajbhiye, G. Balaji, S. Bhattacharyya, M. Ghafari, Mossbauer studies of nanosize CuFe2O4 particles, Hyperfine Interact, 156 (2004) 57-61.

[49] M. Liu, M. Lu, L. Wang, S.C. Xu, J.L. Zhao, H.B. Li, Mossbauer study on the magnetic properties and cation distribution of $CoFe_2O_4$ nanoparticles synthesized by hydrothermal method, J Mater Sci, 51 (2016) 5487-5492.

[50] N.S. Gajbhiye, S. Bhattacharyya, G. Balaji, R.S. Ningthoujam, R.K. Das, S. Basak, J. Weissmuller, Mossbauer and magnetic studies of MFe_2O_4 (M=Co, Ni) nanoparticles, Hyperfine Interact, 165 (2005) 153-159.

[51] T. Ishihara, K. Eguchi, H. Arai, Hydrogenation of Carbon-Monoxide over SiO_2-Supported Fe-Co, Co-Ni and Ni-Fe Bimetallic Catalysts, Appl Catal, 30 (1987) 225-238.

[52] T.M. Salama, H.K. Ebitani, H. Hattori, H. Kita, Electron-Paramagnetic-Resonance Studies of Reduced Platinum Supported on Titanium-Oxide - Effect of Hydrogen Adsorption-Desorption on Paramagnetic Platinum(I) and Titanium(Iii) Species, Chemistry of Materials, 6 (1994) 21-26.

[53] M.Y. Ding, Y. Yang, B.S. Wu, Y.W. Li, T.J. Wang, L.L. Ma, Study on reduction and carburization behaviors of iron phases for iron-based Fischer-Tropsch synthesis catalyst, Applied Energy, 160 (2015) 982-989.

[54] C.H. Zhang, G.Y. Zhao, K.K. Liu, Y. Yang, H.W. Xiang, Y.W. Li, Adsorption and reaction of CO and hydrogen on iron-based Fischer-Tropsch synthesis catalysts, J Mol Catal A-Chem, 328 (2010) 35-43.

[55] X.M. Yang, Y. Wei, Y.L. Su, L.P. Zhou, Characterization of fused Fe-Cu based catalyst for higher alcohols synthesis and DRIFTS investigation of TPSR, Fuel Processing Technology, 91 (2010) 1168-1173.

[56] M.Y. Ding, J.L. Tu, M.H. Qiu, T.J. Wang, L.L. Ma, Y.P. Li, Impact of potassium promoter on Cu-Fe based mixed alcohols synthesis catalyst, Applied Energy, 138 (2015) 584-589.

[57] H.Z. Weixin Qian, Hongfang Ma, Yongdi Liu, Weiyong Ying, Dingye Fang, Adsorption of H_2 and CO on iron based catalysts for Fischer-Tropsch Synthesis, International Journal of Chemical, Molecular, Nuclear, Materials and Metallurgical Engineering, 6 (2012) 581-585.

[58] F. Bozso, G. Ertl, M. Grunze, M. Weiss, Chemisorption of Hydrogen on Iron Surfaces, Appl Surf Sc, 1 (1977) 103-119.

[59] C.H. Bartholomew, Hydrogen Adsorption on Supported Cobalt, Iron, and Nickel, Catalysis Letters, 7 (1991) 27-51.

[60] M.B. Fichtl, O. Hinrichsen, On the Temperature Programmed Desorption of Hydrogen from Polycrystalline Copper, Catalysis Letters, 144 (2014) 2114-2120.

[61] J.W. Evans, P.S. Casey, M.S. Wainwright, D.L. Trimm, N.W. Cant, Hydrogenolysis of Alkyl Formates over a Copper Chromite Catalyst, Appl Catal, 7 (1983) 31-41.

[62] S. Komarneni, M. Tsuji, Y. Wada, Y. Tamaura, Nanophase ferrites for CO_2 greenhouse gas decomposition, Journal of Materials Chemistry, 7 (1997) 2339-2340.

[63] C. Liu, T.R. Cundari, A.K. Wilson, CO_2 Reduction on Transition Metal (Fe, Co, Ni, and Cu) Surfaces: In Comparison with Homogeneous Catalysis, J Phys Chem C, 116 (2012) 5681-5688.

[64] E.B.M.D. Xu Xiaoding, J.J.F. Scholten, synthesis of higher alcohols from syngas- recently patented catalysts and tentative ideas in the mechanism, catalysis today, 2 (1987) 125-170.

[65] C.S. Chen, W.H. Cheng, S.S. Lin, Study of iron-promoted Cu/SiO_2 catalyst on high temperature reverse water gas shift reaction, Appl Catal A Gen, 257 (2004) 97-106.

[66] Y.Q. Zhang, G. Jacobs, D.E. Sparks, M.E. Dry, B.H. Davis, CO and CO_2 hydrogenation study on supported cobalt Fischer-Tropsch synthesis catalysts, Catalysis Today, 71 (2002) 411-418.

[67] T. Riedel, M. Claeys, H. Schulz, G. Schaub, S.S. Nam, K.W. Jun, M.J. Choi, G. Kishan, K.W. Lee, Comparative study of Fischer-Tropsch synthesis with H_2/CO and H_2/CO_2 syngas using Fe- and Co-based catalysts, Appl Catal A Gen, 186 (1999) 201-213.

[68] R.W. Dorner, D.R. Hardy, F.W. Williams, B.H. Davis, H.D. Willauer, Influence of Gas Feed Composition and Pressure on the Catalytic Conversion of CO_2 to Hydrocarbons Using a Traditional Cobalt-Based Fischer-Tropsch Catalyst, Energy & Fuels, 23 (2009) 4190-4195.

[69] A.N. Akin, M. Ataman, A.E. Aksoylu, Z.I. Onsan, CO_2 fixation by hydrogenation over coprecipitated Co/Al_2O_3, React Kinet Catal L, 76 (2002) 265-270.

[70] F. Tihay, A.C. Roger, G. Pourroy, A. Kiennemann, Role of the alloy and spinel in the catalytic behavior of Fe-Co/cobalt magnetite composites under CO and CO_2 hydrogenation, Energy & Fuels, 16 (2002) 1271-1276.

[71] S. Saeidi, N.A.S. Amin, M.R. Rahimpour, Hydrogenation of CO_2 to value-added products—A review and potential future developments, Journal of CO_2 Utilization, 5 (2014) 66-81.

[72] J.C. Slaa, J.G. Vanommen, J.R.H. Ross, The Synthesis of Higher Alcohols Using Modified Cu/Zno/Al_2O_3 Catalysts, Catalysis Today, 15 (1992) 129-148.

[73] H. Fink, Untersuchungen zur hcoholsynthese an einem Cu-ZnO-Katalysator im Differentialkreislaufreaktor, T.H. Aachen, Germany, Ph.D. Thesis,, (1988).

[74] C.S. Chen, W.H. Cheng, S.S. Lin, Mechanism of CO formation in reverse water-gas shift reaction over Cu/Al_2O_3 catalyst, Catalysis Letters, 68 (2000) 45-48.

Chapter IV

The synthesis of higher alcohols from CO_2 hydrogenation with CuFe metal/oxides catalysts on CNTs and TUD-1 supports

IV.1 Introduction

In chapter III, four kinds of catalysts (CoFe-pressure-800, CuFe-precursor-800, CuCo-precursor-800 and CoCuFe-precursor) were characterized and their performance in the CO_2 hydrogenation reaction was evaluated. According to the results, catalyst CuFe-precursor-800 owns higher selectivities and productivities to C_{2+} hydrocarbons and higher alcohols. So in this chapter, we will try to improve the activity to higher alcohols of CuFe-based material. Suitable supports will be chosen to increase the surface area of Cu and Fe mixed oxide catalyst and generate more active surface by reduction. A good support should own large surface area for loading the active phases, suitable pore structure for the mass transfer, and should stabilize the active phases and promoters [1].

TUD-1 material can be easily synthesized with a surfactant-free method, which is environmentally friendly and cost-effective. Particularly, its high thermal stability, three-dimensional sponge-like silicate framework with high surface area and substrate accessibility make it more advantageous than other microporous and mesoporous materials [2].

The carbon nanotubes (CNTs) possess several unique features, such as graphitized tube-wall, nanometer-sized channel and sp^2-C constructed surface. They display exceptionally high mechanical strength, high thermal/electrical conductivity, medium to high specific surface areas, and excellent performance for adsorption activation and spillover of hydrogen, all of which render this kind of nano-structured carbon materials full of promise to be a novel catalyst support and/or promoter [3].

So in this chapter, the carbon nanotubes and TUD-1 were chosen as supports for CuFe-based new catalysts.

IV.1.1 The purification of carbon nanotubes

The raw CNTs (Sigma-Aldrich, ≥98% carbon basis, O.D. $\times$ I.D. $\times$ L 10 nm ± 1 nm $\times$ 4.5 nm ± 0.5 nm $\times$ 3-6 μm, TEM) are purified in concentrated HNO$_3$ (68 vol %) for 10h at 120 °C in a roundflask with oil bath while stirring. Then the CNTs were washed with deionized water until a pH around 7, and dried at 80 °C for 8h [4]. After drying, the CNTs were crushed and sieved to particles (75-300 μm) before being impregnated.

IV.1.2 The synthesis of TUD-1

The pure TUD-1 was synthesized using triethylamine (TEA) as template in a one-pot surfactant-free procedure based on the sol-gel technique [5]. 23.01 g of TEA were mixed with 17.30 g of H$_2$O and stirred until the TEA was dissolved. The solution was then added to 31.84 g of tetraethyl orthosilicate (TEOS) drop by drop slowly and stirred for about 30 min. 32.85 g of tetraethyl ammonium hydroxide (TEAOH) were finally added to the mixture. The solution changed to gel after around three days at room temperature. The gel was dried at 95 °C for 10 h and calcined at 800 °C for 6 h. The TUD-1 was sieved to particles (75-300 μm) before being impregnated.

IV.1.3 The preparation of CuFeCNTs and CuFeTUD-1

Five catalysts will be prepared, which are named 10CuFeCNTs, 30CuFeCNTs, 50CuFeCNTs, 70CuFeCNTs and 30CuFeTUD-1. According to the XRD patterns of CuFe-precursor-800 in chapter III, there are CuFe$_2$O$_4$, CuO and a little of Fe$_2$O$_3$ in the catalyst. So the Cu and Fe mixed oxides were also expected in the catalyst with supports. The percentage of loading of CuFe-precursor on supports were calculated assuming CuFe$_2$O$_4$. For example 10CuFeCNTs is supposed to be composed of 10 wt% of CuFe$_2$O$_4$ and 90 wt% of CNTs.

First, the resin of propionic precursor was prepared by the pseudo sol-gel method

as described in chapter III. The resin was then dissolved in a calculated volume of propionic acid again until a concentration of cations 0.63 mol·L^{-1} is obtained. The impregnation method was used to deposit the metal phases on the supports. The quantities of concentrated solution of mixte propionate resin and supports are presented in Table 18. The carbon nanotubes (0.5 g) or TUD-1 (0.5 g) were added to the solution of resin and put under ultra sound for 1h, then dried at 120 °C for 10 h. Contrary to what have been done in the previous chapter for the calcination of CuFe-precursor-800, and in order to avoid the CNTs to be oxidized into CO_2 at high calcination temperature under air, the CuFe-precursor with CNTs were annealed under N_2 at 800 °C for 6 h with a ramp of temperature 2 °C·min^{-1}. The CuFe-precursor with TUD-1 was calcined under air at same conditions of temperature.

Table 18 The preparation of CuFe-precursor with supports

Samples	Weight of supports (g)	Volume of solution at 0.63 M (mL)
10CuFeCNTs	0.5	1.1
30CuFeCNTs	0.5	4.3
50CuFeCNTs	0.5	10.0
70CuFeCNTs	0.5	23.3
30CuFeTUD-1	0.5	4.3

IV.2 Catalysts characterization

IV.2.1 Elemental analysis

The elemental analysis is presented in Table 19. The experimental results are rather close to the expected theoretical contents except for 50CuFeCNTs where much higher amounts of Cu and Fe are obtained. Let's note that the experimental Fe/Cu

ratio in mole is around 1.8 whereas a ratio of 2.0 was expected. All the materials are enriched in copper.

Table 19 The elemental analysis of CuFe-based supported catalysts

Catalysts	Theoretical (wt%)		Experimental (wt%)		Experimental (mmol·g⁻¹)		Fe/Cu ratio
	Fe	Cu	Fe	Cu	Fe	Cu	
10CuFeCNTs	4.7	2.7	3.7 ± 0.1	2.7 ± 0.1	0.7	0.4	1.8
30CuFeCNTs	14.0	8.0	14.4 ± 0.3	9.1 ± 0.2	2.6	1.4	1.9
50CuFeCNTs	23.3	13.3	27 ± 1	17.9 ± 0.7	4.8	2.8	1.7
70CuFeCNTs	32.7	18.7	30 ± 1	19.6 ± 0.7	5.4	3.1	1.7
30CuFeTUD-1	14.0	8.0	11.0 ± 0.3	7.1 ± 0.2	2.0	1.1	1.8

IV.2.2 Textural and structural properties of catalysts

The BET surface area, pore volume and apparent density of supported catalysts and supports are shown in Table 20. The BET surface area of CNTs is 238 $m^2 \cdot g^{-1}$. The BET surface areas of materials with low loading CuFe-precursor (10CuFeCNTs and 30CuFeCNTs) were apparently higher, 361 and 276 $m^2 \cdot g^{-1}$ respectively, than that of CNTs (238 $m^2 \cdot g^{-1}$). With increasing loading of CuFe-precursor, the surface area largely decreased, and the surface areas of 50CuFeCNTs and 70CuFeCNTs, 200 and 101 $m^2 \cdot g^{-1}$ respectively, were much lower than that of CNTs. The pore volume logically follows the same tendency and takes values between 1.6 $cm^3 \cdot g^{-1}$ for 10CuFeCNTs and 0.3 $cm^3 \cdot g^{-1}$ for 70CuFeCNTs. This results in apparent density which vary inversely. The apparent density increased with the increasing CuFe-precursor loading. The apparent densities of 10CuFeCNTs (0.16 g·cm⁻³) and 30CuFeCNTs (0.20 g·cm⁻³) were much lower than that of CNTs (0.31 g·cm⁻³). Meanwhile, the apparent density of

70CuFeCNTs (0.43 g·cm^{-3}) was much higher than that of CNTs.

The characteristic N$_2$ sorption isotherm of CuFe-based CNTs supports catalysts and CNTs are shown in Figure 43. The adsorption value of 10CuFeCNTs was apparently higher than the others at the P/P$_o$ range of 0.05 to 0.35, so there were smaller pores in the catalyst 10CuFeCNTs, which explains the higher surface area [6]. This may be because of the highly dispersed CuFe-precursor on the surface of CNTs and formed small particles after calcination. With increasing loading, there are maybe larger particles which can mobilize the pore volume of CNTs.

For CuFe-material with TUD-1 as support, the loading by CuFe-precursor decreased the BET surface area (from 303 m^2·g^{-1} to 199 m^2·g^{-1}) and pore volume (from 0.4 cm^3·g^{-1} to 0.3 cm^3·g^{-1}). To the contrary, the apparent density increased a little (from 0.65 g·cm^{-3} to 0.71 g·cm^{-3}).

Table 20 The BET surface area, pore volume and apparent density of CuFe-based supported catalysis and supports

Samples	S$_{BET}$ (m^2·g^{-1})	V$_{total}$ (cm^3·g^{-1})	Density (g·cm^{-3})
10CuFeCNTs	361	1.6	0.16
30CuFeCNTs	276	1.1	0.20
50CuFeCNTs	200	0.7	0.30
70CuFeCNTs	101	0.3	0.43
pure CNTs [a]	238	1.0	0.31
30CuFeTUD-1	199	0.3	0.71
pure TUD-1	303	0.4	0.65

a: The surface area and density of CNTs after purification by concentrated nitric acid and calcination at 800 °C under N$_2$
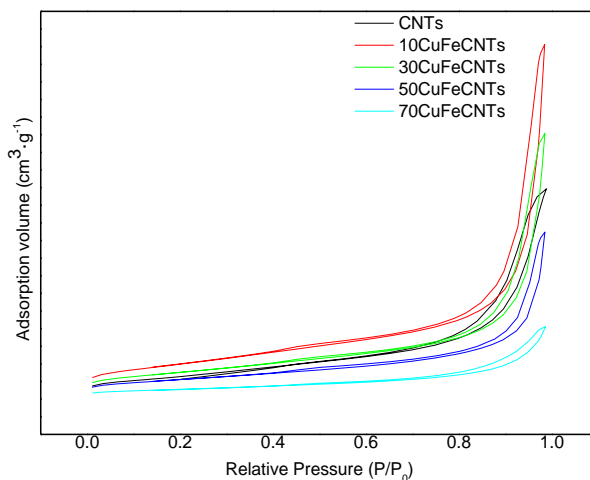
Figure 43 Characteristic N_2 sorption isotherm of CuFe-based supported catalysts and CNTs

At similar content of 30 wt% of CuFe precursors, the material supported on CNTs presents larger BET surface area, much higher pore volume and much lower density than the material with TUD-1 support.

Compared to catalyst CuFe-precursor-800 in chapter III, all the supported catalysts exhibit much larger surfaces and pore volumes.

IV.2.3 X-Ray Diffraction (XRD)

The XRD patterns of CNTs, 10CuFeCNTs, 30CuFeCNTs, 50CuFeCNTs and 70CuFeCNTs are presented in Figure 44. For comparison, we prepared a pure CuFe sample from annealing of the CuFe resin under N_2 at 800 °C. This sample was named CuFe-precursor-N_2. Its diffraction pattern is also shown in Figure 44.

Compared to the CuFe-precursor-800 in chapter III, the phases detected were only metallic Cu (JCPDS01-070-3039) and Fe (JCPDS 03-065-4899 in the catalysts after calcination under N_2. No $CuFe_2O_4$ spinel phase is evidenced, even for CuFe-precursor-N_2. Gaseous O_2 is needed to crystallize $CuFe_2O_4$, the O^{2-} anions of the propionate resin are not sufficient.

Diffraction lines of the alloy $FeCu_4$ (JCPDS 03-065-7002) are similar to those of Cu (JCPDS01-070-3039). The presence of a CuFe alloy in the catalysts can thus not be excluded. The CNTs diffraction lines were apparent for 50CuFeCNTs, experimental CuFe content of 44.9 %) and for materials of lower CuFe content. When the loading of CuFe increased to 49.6% (70CuFeCNTs), the diffraction lines of CNTs are hardly visible. In addition, for 70CuFeCNTs the diffraction lines of metallic Fe are of low intensity with respect to the diffraction lines of Cu or $FeCu_4$ alloy. As elemental analysis proved that the Fe/Cu ratio is similar for all the supported material, this clearly indicates that CuFe alloy is formed, at least at high CuFe content.
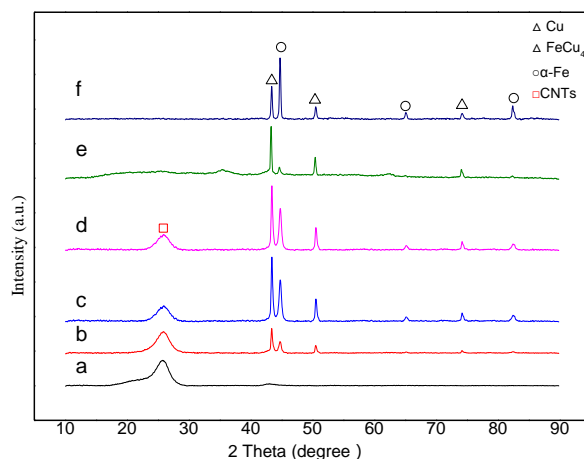
Figure 44 The XRD pattern of (a) pure CNTs calcined under N₂ atmosphere,

(b) 10CuFeCNTs, (c) 30CuFeCNTs, (d) 50CuFeCNTs, (e) 70CuFeCNTs, (f)

CuFe-precursor-N₂

The size of metallic Cu (CuFe alloy) and metallic Fe crystalline domains which were calculated by the Debye-Scherrer formula is presented in Table 21. The size of metallic Fe (33.1 nm) of CuFe-precursor-N₂ was apparently larger than for all the CuFe/CNTs catalysts. For metallic Cu or $CuFe_4$ alloy, the size of metallic Cu ($CuFe_4$ alloy) in CuFe-precursor-N₂ (33.6 nm) is higher than in 10CuFeCNTs (30.2 nm) and 30CuFeCNTs (30.1nm), but lower than it in 50CuFeCNTs (36.8 nm) and

70CuFeCNTs (35.8 nm)

From the results of particle size, it can be found that the CNTs as support can effectively increase the dispersion of metal phases and decrease the particles size at low loading of CuFe-precursor.

Table 21 Particle size of Cu or FeCu$_4$ alloy and Fe in CuFe/CNTs catalysts and CuFe-precursor-N$_2$

Catalysts	Particle size (nm)	
	Cu/FeCu$_4$ alloy	Fe
10CuFeCNTs	30.2	19.2
30CuFeCNTs	30.1	19.4
50CuFeCNTs	36.8	30.0
70CuFeCNTs	35.8	20.0
CuFe-precursor-N$_2$	33.6	33.1

The XRD patterns of 30CuFeTUD-1 and TUD-1 are shown in Figure 45. Copper oxides (CuO and Cu$_4$O$_3$) are detected in the catalyst. Because the diffraction lines of Fe$_3$O$_4$ are similar to that of CuFe$_2$O$_4$ spinel, it is not sure that the mixed CuFe spinel has been formed.
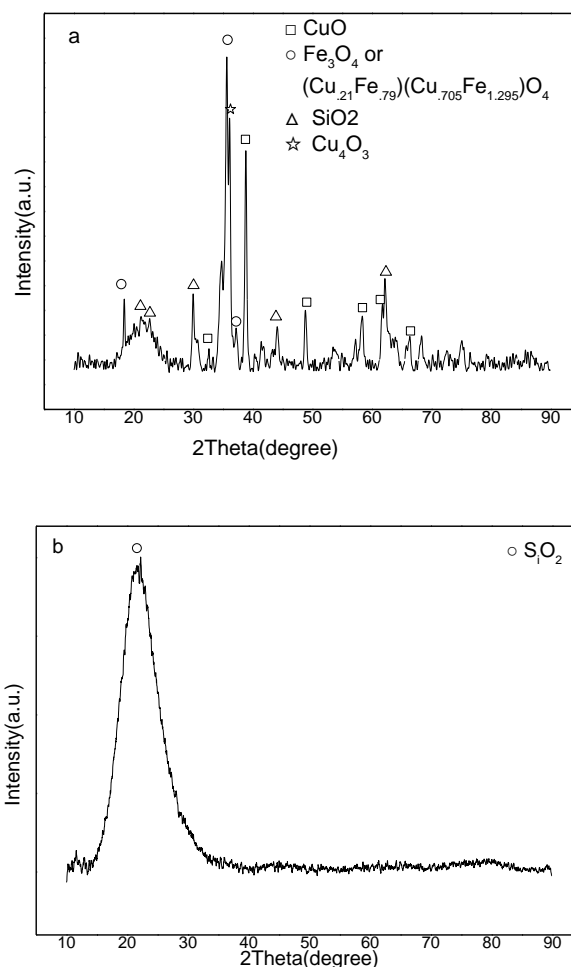
Figure 45 The XRD pattern of a) 30CuFeTUD-1 and b) TUD-1

IV.2.4 Scanning Electron Microscope (SEM)

The SEM images of 10CuFeCNTs, 30CuFeCNTs, 50CuFeCNTs, and 70CuFeCNTs are displayed in Figure 46. It can found that the metal particles highly dispersed on the carbon nanotubes for low loading of CuFe-precursor (10CuFeCNTs and 30CuFeCNTs). With the increasing loading of CuFe, there were much more big particles and sintered on the surface.
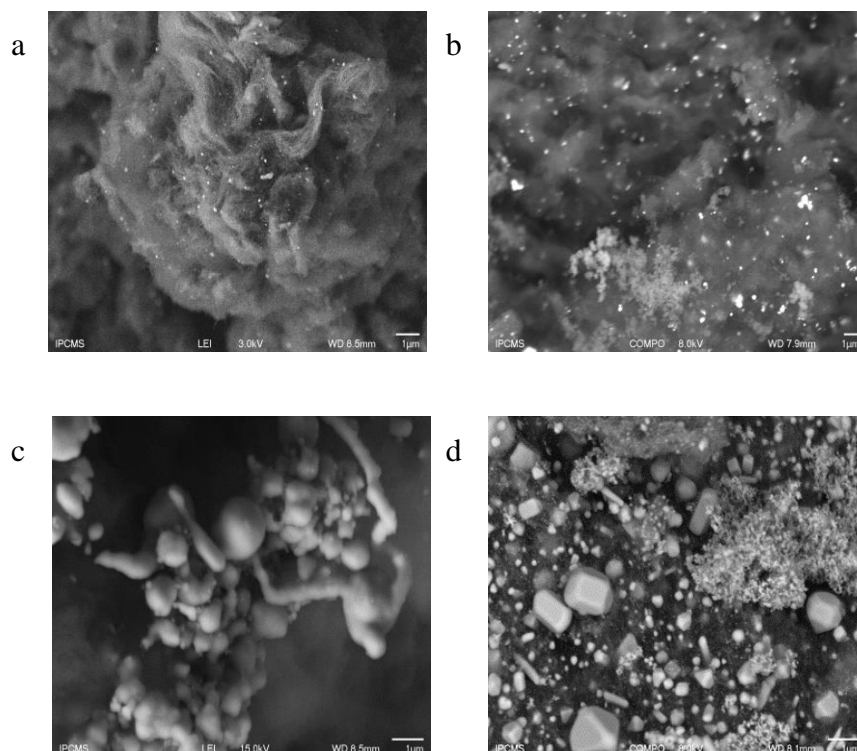
Figure 46 SEM images of (a) 10CuFeCNTs, (b) 30CuFeCNTs,

(c) 50CuFeCNTs and (d) 70CuFeCNTs

A theoretical loading lower than 50% appears to be better for the dispersion of metal particles and the interaction with support.

IV.2.5 Transmission electron microscopy (TEM)

TEM images of 30CuFeCNTs are shown in Figure 47. The diameter of big particles are around 25 nm and the small particles are around 10 nm. The lattice spacing at 0.28 nm corresponds to pure α-Fe (100) in bcc structure [7, 8], and a spacing of 0.24 nm may correspond to γ-Fe$_2$O$_3$ (311) (d-spacing 0.25 nm) [9]. The d-spacing of Cu (111) is 0.21 nm and it is difficult to defect Cu in the TEM images. The small particles are mainly metallic iron, and the big particles included metallic iron and iron oxide.
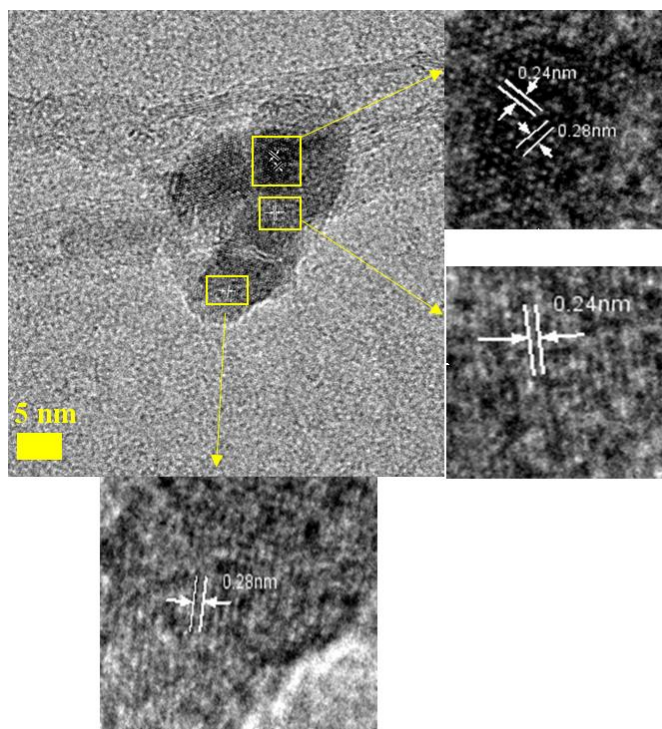
Figure 47 The TEM images of 30CuFeCNTs

IV.2.6 Mössbauer spectroscopy

The Mössbauer spectrum of 30CuFeCNTs is shown in Figure 48, and the magnetic parameters are presented in Table 22. The spectrum can be decomposed into three sub spectra. The sextet with isomer shift of 0.00 and corresponding values of hyperfine magnetic field (H_{hf}) at 33.3 T can be attributed to metallic α-Fe, and 71% of iron is under the form α-Fe. There are 16% of iron in paramagnetic metallic iron with isomer shift at -0.09 mm/s. The spectrum with isomer shift at 0.25 mm/s and H_{hf} at 47.3 T is attributed to Fe^{3+} in maghemite γ- Fe_2O_3. The presence of this oxide phase in small amount can explain that it has not been detected by XRD and is consistent with what has been observed by TEM. The quadrupole shift of all the three spectrum was zero.

From the analysis of Mössbauer spectroscopy, it is found that there are mainly metallic iron in the catalyst after calcination under N_2 atmosphere. Two kinds of metallic iron were detected. Combined with the results of XRD, it can be assumed

104

that the α-Fe along with CuFe alloy were formed in the catalysts with CNTs as support.
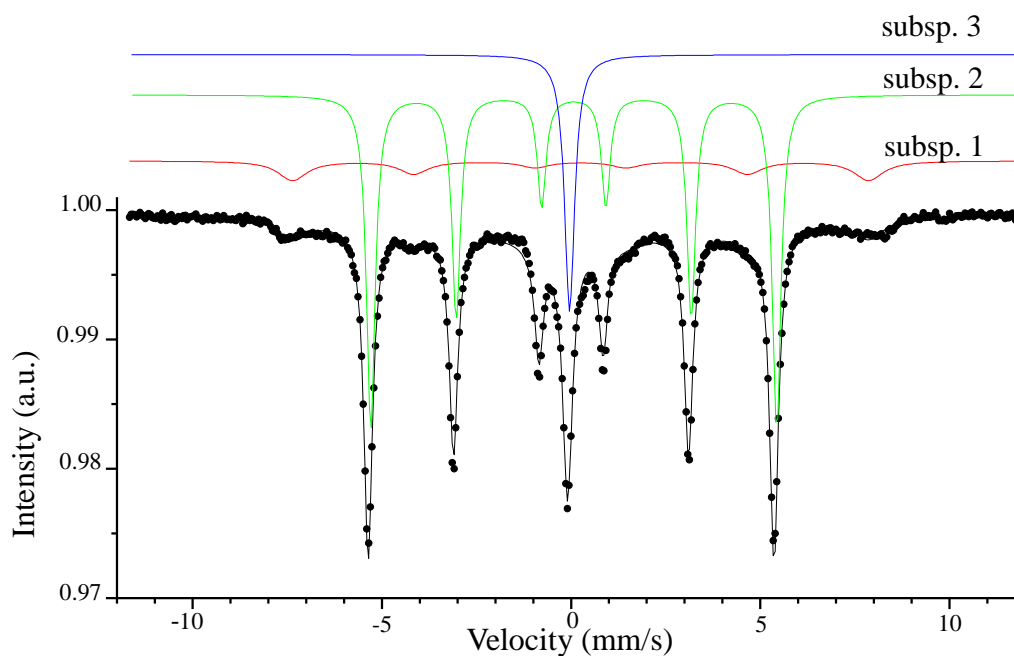
Figure 48 the Mössbauer spectrum of 30CuFeCNTs at room temperature

Table 22 The analysis of Mössbauer spectrum of 30CuFeCNTs at room temperature

	Isomer shift δ (mm/s)	Quadrupole splitting ΔE_Q	Hyperfine field B_{Hf}	Relative area (%)	Interpretation
Subsp. 1	0.25	0.00	47.3 T	13	Fe^{3+} in maghemite
Subsp. 2	0.00	0.00	33.3 T	71	Fe in metallic α-iron (ferromagnetic)
Subsp. 3	-0.09	0.00	N/A	16	Fe in metallic iron (paramagnetic)

IV.2.7 X-ray photoelectron spectroscopy (XPS)

IV.2.7.1 30CuFeCNTs

The spectra of Cu 2p, Fe 2p and O 1s regions of 30CuFeCNTs are presented in Figure 49 (a), (b) and (c). The binding energy (BE) at 932.8 eV can be attribute to Cu^0 and the BE at 934.1 eV with a broad satellite peak at 942.6 eV indicates the existent of Cu^{2+} [10].

The binding energy of Fe $2p_{3/2}$ and Fe $2p_{1/2}$ around 710.9 eV and 724.9 eV are consistent with the presence of Fe_3O_4, not evidenced in bulk, at the surface of the catalyst [11, 12]. The satellite peak at 718.5 eV is corresponding to Fe^{3+} in γ-Fe_2O_3 [13]. So there are Fe_3O_4 and γ-Fe_2O_3 on the surface of 30CuFeCNTs. The Fe $2p_{3/2}$ of Fe^0 is at around 707 eV [14], so it is difficult to detect metallic iron by XPS, which is maybe due to the easy oxidation of iron by air to lead to Fe_3O_4. The ratio of Fe/Cu on the surface of catalyst is 1.0.
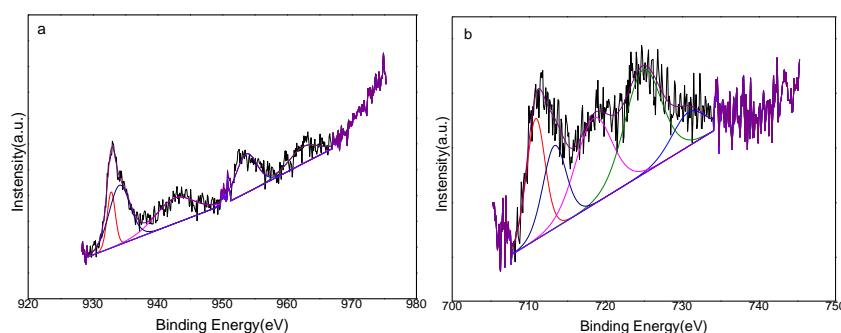
Figure 49 XPS of (a) Cu2p and (b) Fe2p of 30CuFeCNTs

IV.2.7.2 50CuFeCNTs

The spectra of Cu 2p, Fe 2p and O 1s of 50CuFeCNTs are displayed in Figure 50 (a), (b) and (c). Cu^0 (BE at 932.7 eV) also exists in the catalyst, the peak with binding energy at 935.1 eV, and a weak broad satellite peak at 942.1 eV indicates the existence of CuO at the surface. The peaks of Fe2p are of very low intensity, and there is mainly Fe^{3+} (BE at 713.1 eV) on the surface. The ratio of Fe/Cu on the surface of catalyst is 1.5.
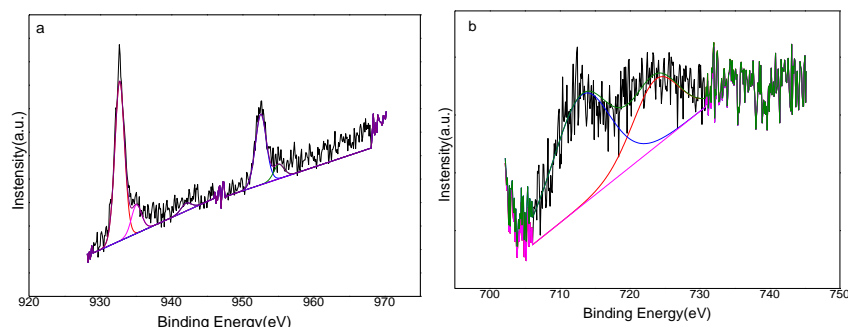
Figure 50 XPS of (a) Cu2p and (b) Fe2p of 50CuFeCNTs

IV.2.7.3 70CuFeCNTs

According to the spectra of Cu 2p in Figure 51 (a), there is Cu^0 (BE at 932.9 eV) in the catalyst. The peaks at 934.0 eV with a satellite peak at 942.0 eV indicates the existence of CuO.

As for 30CuFeCNTs, there are also Fe_3O_4 (BE at 710.8 eV and 713.0 eV and 724.7 eV) and γ-Fe_2O_3 (BE of satellite peak at 719.6 eV) on the surface of 70CuFeCNTs. The ratio of Fe/Cu on the surface of 70CuFeCNTs is 1.8.
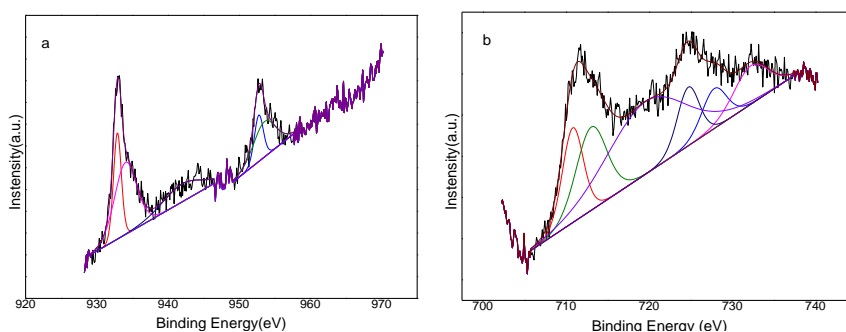
Figure 51 XPS of (a) Cu2p and (b) Fe2p of 70CuFeCNTs

From the results of XPS, we found that the ratio Fe/Cu on surface of catalysts increased with the loading of CuFe-precursor. The ratio of Fe/Cu on the surface of 70CuFeCNTs is similar to the result of elemental analysis that Fe/Cu ratio is 1.7. The ratio of Fe/Cu at low loading of CuFe-precursor are much lower than the desired ratio,

which is may be due to the strong cooperation of Fe and carbon nanotubes. The vacant in d-orbitals of Fe can form bonds with carbon atoms of CNTs [15], which lead to strong stabilization of iron on carbon materials [16].

Conclusions for the surface characterizations:

- ➢ Both supports (CNTs and TUD-1) can effectively increase the surface area of catalysts compared to the pure catalysts without support in chapter III.
- ➢ There are metallic Cu and CuFe alloy and metallic Fe in the catalysts with CNTs as support. A small amount of γ- Fe_2O_3 is also evidenced. The copper iron mixed spinel together with copper oxides exist in the catalysts with TUD-1 as support.
- ➢ Low loading of CuFe-precursor (10CuFeCNTs and 30CuFeCNTs) can promote the interaction with support especially CNTs. Smaller metal particles can be formed.

IV.2.8 H₂ temperature Programmed Reduction (H₂-TPR)

H₂-TPR was performed to study the reducibility of catalysts with supports. The H₂-TPR profiles of 10CuFeCNTs, 30CuFeCNTs, and 50CuFeCNTs are shown in Figure 52 and the corresponding H₂ consumption that was calculated according to H₂-TPR curve are given in Table 23. For CuFe/CNTs catalysts, the real H₂ consumption of all the catalysts were below 0.6 mmol·g⁻¹, which is much lower than the theoretic H₂ consumption. The theoretical H₂ consumption was calculated according to the results of elemental analysis and assumption that all the metals in catalysts existed in oxidation state which is clearly not the case, as explained before. All the catalysts can be easily reduced below 400 °C. It is consistent with thin layer of metal oxides on the surface.
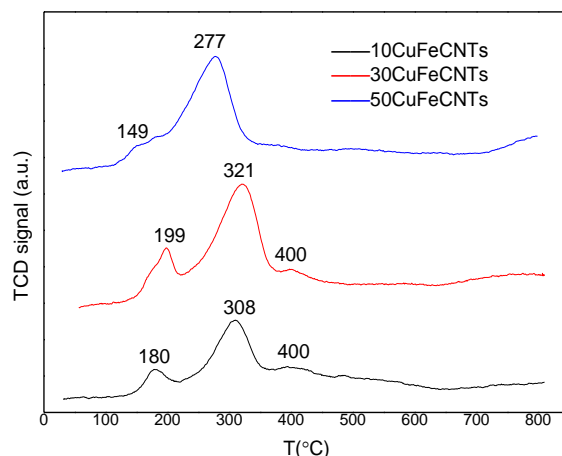
Figure 52 The H_2-TPR profiles of 10CuFeCNTs, 30CuFeCNTs, and 50CuFeCNTs

The H_2-TPR profile of 30CuFeTUD-1 is shown in Figure 53, and H_2 consumption is also calculated in Table 23. According to the result of XRD in Figure 45, there were copper oxides and copper iron mixed spinel in the catalyst. The reduction peak at 281 °C is attributed to the highly dispersed CuO [17]. The two peaks at 478 °C and 597 °C can be attributed to the reduction of copper iron mixed spinel and the reduction of Fe_3O_4 to Fe^0 *via* FeO. The reduction peak at high temperature (765 °C) may be due to the reduction of iron silicate species [18]. The H_2 consumption calculated according to H_2-TPR is 4.44 mmol·g^{-1}, and the theoretic H_2 consumption is 5.00 mmol·g^{-1}, around 88% of metals can be reduced.
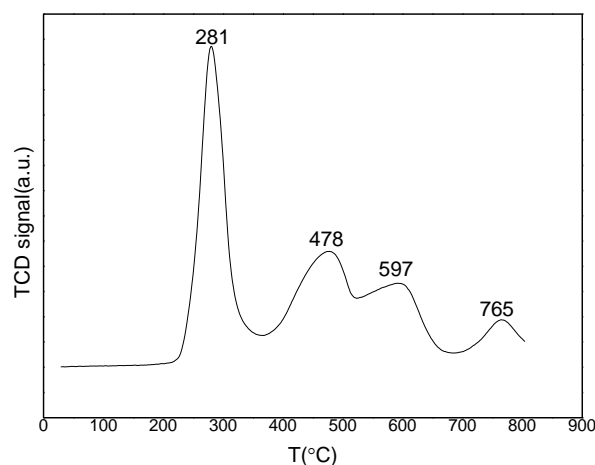
Figure 53 The H_2-TPR profile 30CuFeTUD-1

Table 23 The H$_2$ consumption of CuFe-based supported catalysts

Catalysts	H$_2$ consumption (mmol·g^{-1})	
	Real H$_2$ consumption	Theoretic H$_2$ consumption
10CuFeCNTs	0.39	1.41
30CuFeCNTs	0.51	5.27
50CuFeCNTs	0.48	10.03
30CuFeTUD-1	4.44	5.00

According to the analysis of Mössbauer spectroscopy, there are only 13% of iron in the oxide form of maghemite. That corresponds to 0.50 mmol of H$_2$ which is needed for the reduction of iron in every gram of 30CuFeCNTs catalyst. This is very similar to the results of H$_2$-TPR where the consumption is 0.51 mmol of H$_2$ per gram.

According to the results of H$_2$-TPR, the metals can be totally reduced with CNTs as support. 88% of metals can be reduced with TUD-1 as support. The reduction temperature of TUD-1 as support increased a lot compared to the CuFe catalyst without support in Chapter III.

IV.2.9 H$_2$ Temperature Programmed Desorption (H$_2$-TPD)

To quantity the metallic surface available for catalytic reaction, the H$_2$-TPD was carried out after partial reduction at 400 °C. The H$_2$-TPD profile of pure CNTs is shown in Figure 54 (a). There are four H$_2$ desorption peaks, the first desorption peak was present at a lower-temperature part (part I: ~238 ℃), the other three peaks was located at a higher-temperature part (part II : >500 °C). From the TPD profile of CH$_4$ and C$_2$H$_4$ desorption of pure CNTs in Figure 54 (b) and (c), it was found that there were small amount of CH$_4$ and C$_2$H$_4$ in the products. This may be due to two reasons: one is the dissociation of strongly adsorbed species [19], the other reason is the gasification of CNTs at high temperature. This is consistent with the results of Zhang

et al. [20]. The formation of methane is because the transition metals can act as catalysts and promote the reaction of hydrogen with carbon nanotubes when T is higher than 600 °C [21]. This implies that H$_2$ adsorption on the CNTs may be in the two forms: associative (molecular state) and dissociative (atomic state) [20].

According to the analysis, the peak in part I can be attributed to desorption of molecularly adsorbed hydrogen. The peaks in part II is due to strongly adsorbed H species.
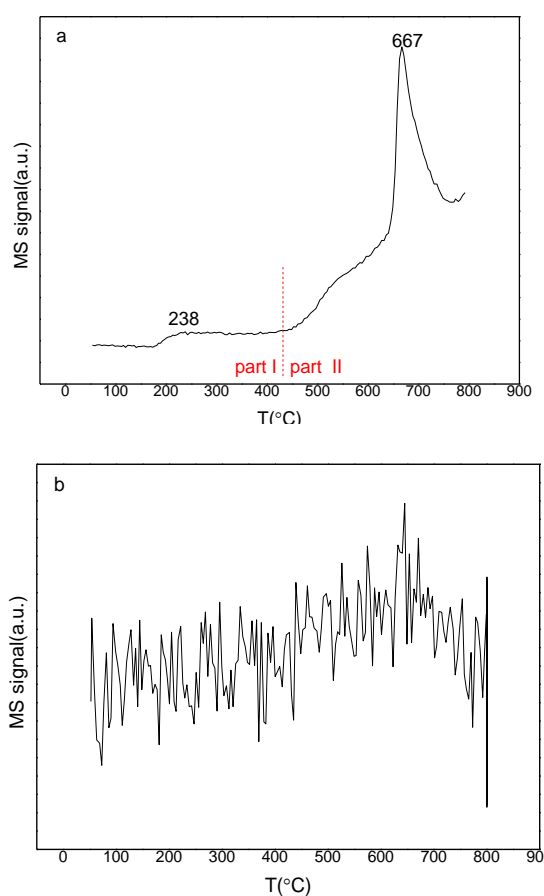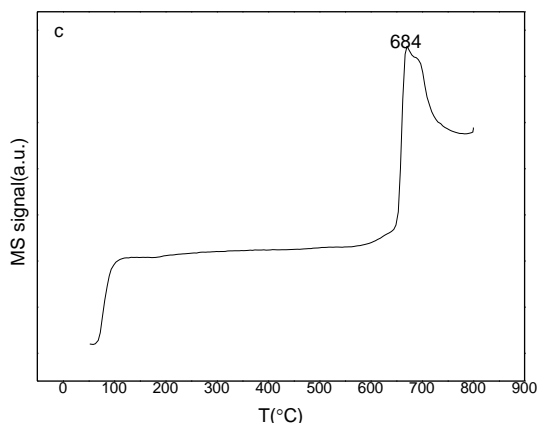
Figure 54 The TPD profiles of (a) H$_2$, (b) CH$_4$ and (c) C$_2$H$_4$ desorption of pure CNTs

The H$_2$ desorption profiles of 10CuFeCNTs, 30CuFeCNTs, 50CuFeCNTs and 70CuFeCNTs are presented in Figure 55. The quantity of desorbed H$_2$ was calculated in Table 24. The peaks at low temperature (Part I: below 400 °C) represents the H$_2$ desorption from metals sites (Fe and Cu and CuFe alloy) or carbon nanotubes for all the catalysts. There was only one peak in the low temperature region, which indicates only one type of adsorbed species. The desorption temperature and quantity of desorbed H$_2$ increased with the loading of CuFe from 257 °C to 327 °C for 10CuFeCNTs and 70CuFeCNTs respectively, and from 25 μmol·g^{-1} to 310 μmol·g^{-1} for 10CuFeCNTs and 70CuFeCNTs respectively.

According to the research of Yang [22], the H$_2$ desorption temperature on Fe sites was higher than on Cu sites, and there were two H$_2$ desorption peaks on the Fe-Cu based catalyst, so the only peak in part I could be an indicator of CuFe alloy. The good cooperation of Cu and Fe can form unsaturated coordination metal centers and form strong bonds with H$_2$ [22].

From the H$_2$-TPD analysis of pure CNTs, the H$_2$ that desorbed above 500 °C was mainly caused by CNTs, which may be attributed to the desorption of strongly chemisorbed H-species ((sp^2-C)-H species) [23, 24]. The quantity of H$_2$ desorption from part I increased with the loading of CuFe, and the quantity of H$_2$ desorption from part II decreased from 0.56 mmol·g^{-1} to 0.10 mmol·g^{-1} with the percentage of CNTs from 90% to 30%.

112

The metallic surface can be calculated according to H_2 desorption in the part I. The molar surface ratio of Fe/Cu is 1.0, 1.5 and 1.8 for 30CuFeCNTs, 50CuFeCNTs and 70CuFeCNTs respectively. The metallic surface of copper and iron is shown in Table 24. It can be found that 50CuFeCNTs has the highest metallic surface of copper and iron, 19.7 and 26.6 $m^2 \cdot g^{-1}_{cata}$ respectively. The metallic surface of copper and iron on the surface of 70CuFeCNTs are the lowest, 10.8 and 6.2 $m^2 \cdot g^{-1}_{cata}$ respectively.
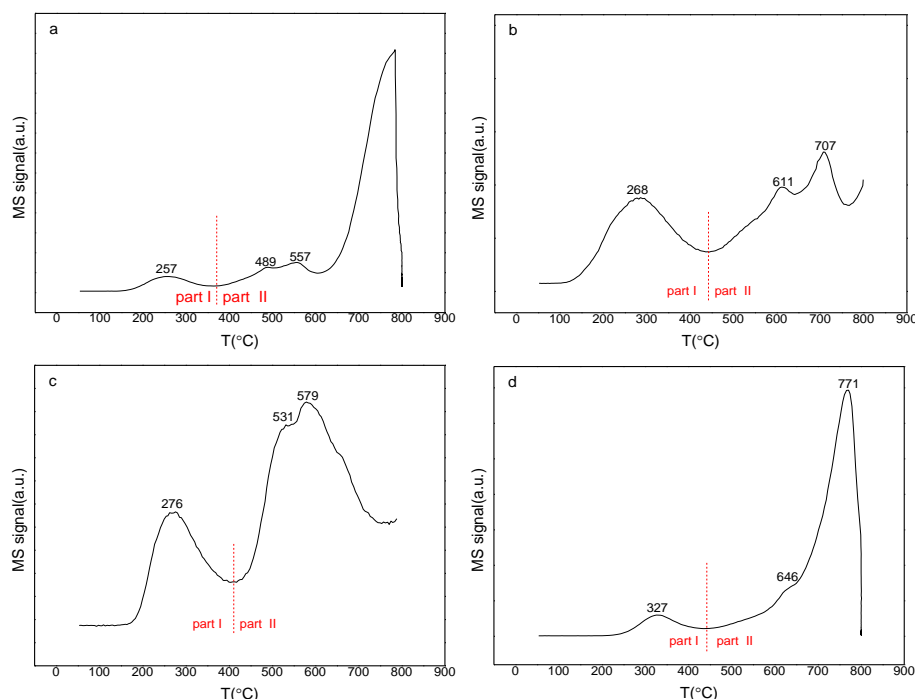
Figure 55 The H_2-TPD profiles of (a) 10CuFeCNTs, (b) 30CuFeCNTs,

(c) 50CuFeCNTs, and (d) 70CuFeCNTs

Table 24 The quantity of desorbed H_2 on the CuFe-based supported catalysts during H_2-TPD

process

Catalysts	H_2 desorption (mol·g^{-1})			Metallic surface (m^2·g$^{-1}_{cata.}$)		
	Part I	Part II	Total	Cu	Fe	Total
10CuFeCNTs	2.5×10^{-5}	5.6×10^{-4}	5.9×10^{-4}	-	-	-
30CuFeCNTs	3.4×10^{-5}	5.2×10^{-4}	5.5×10^{-4}	11.3	15.3	26.6
50CuFeCNTs	5.0×10^{-5}	1.7×10^{-4}	2.2×10^{-4}	19.7	26.6	46.3
70CuFeCNTs	3.1×10^{-4}	1.0×10^{-4}	1.4×10^{-4}	10.8	6.2	17.0

The H$_2$ desorption profiles of 30CuFeTUD-1 and TUD-1 are shown in Figure 56. There are two H$_2$ desorption peaks at 330 °C and 515 °C in the part I, which correspond to H$_2$ desorption from Cu sites and Fe sites respectively [22]. The big peaks above 600 °C was attributed to the strongly adsorbed H$_2$ on TUD-1. The H$_2$ desorption of part I, part II and total H$_2$ desorption of 30CuFeTUD-1 is 1.1×10^{-5}, 5.0×10^{-4} and 5.1×10^{-4} mol·g^{-1} respectively.
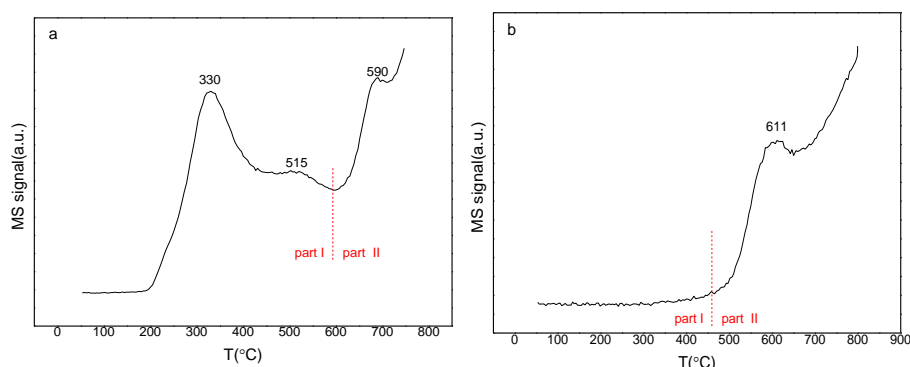
Figure 56 The H$_2$-TPD profiles of (a) 30CuFeTUD-1, (b) Pure TUD-1

From the results of H$_2$-TPD, compared to catalyst with TUD-1 as support, the catalysts with CNTs as support own better H$_2$ adsorption ability.

IV.2.10 NH$_3$ Temperature Programmed Desorption (NH$_3$-TPD)

In order to study the effect of acid sites on the surface of the supports in the reaction of higher alcohols synthesis (HAS), NH$_3$-TPD was performed. The NH$_3$ desorption curves of 30CuFeCNTs and 30CuFeTUD-1 and quantity of acid sites are shown in Figure 57.
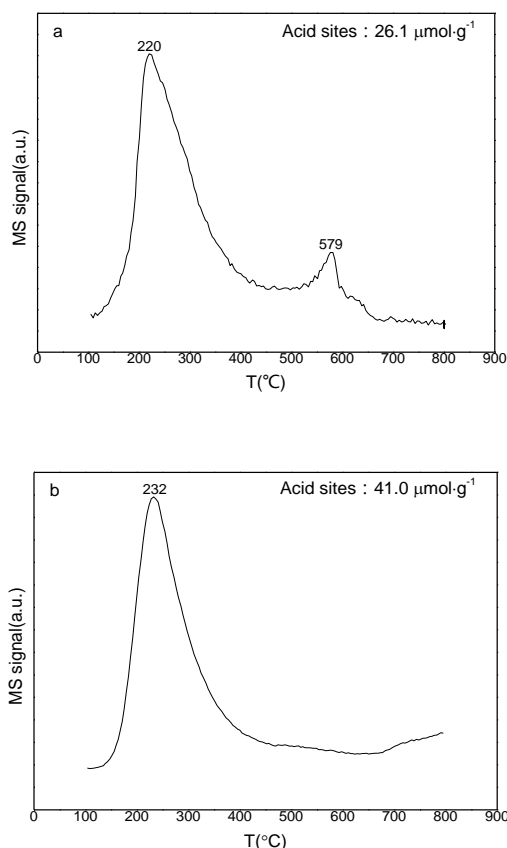
Figure 57 The NH$_3$-TPD profiles of a) 30CuFeCNTs and b) 30CuFeTUD-1

There are two NH$_3$ desorption peaks in the NH$_3$-TPD of 30CuFeCNTs, which indicates two different kinds of acid sites. Weaker acidic site desorb NH$_3$ at lower temperature of around 220 °C, and stronger acid sites are related to the desorption peak at higher temperature at about around 579 °C. For 30CuFeTUD-1, there are weak acid site (peak at around 232 °C), and there is also a little of NH$_3$ desorption above 700 °C.

For 30CuFeCNTs, the NH$_3$ desorption peak at around 220 °C may be due to the acidic groups on the surface of CNTs [25].

As for zeolites based catalyst, usually there are two different kinds of acid sites on the surface, one is at lower temperature (between 100 °C and 300 °C), it is attributed to the desorption of weakly bound ammonia. The peak at higher temperature region (between 300 °C and 500 °C) is usually attributed to the ammonia desorbed from Brønsted acid sites [26, 27].

According to the acid sites calculated in Figure 57, the number of acid sites on the surface of 30CuFeTUD-1 is much higher than on surface of 30CuFeCNTs, and mainly of same strength.

IV.2.11 CO_2 Temperature Programmed Desorption (CO_2-TPD)

CO_2-TPD are performed to characterize the intensity and strength of surface basic sites on samples 30CuFeCNTs and 30CuFeTUD-1. As shown in Figure 58 (a), there are two CO_2 desorption zones in the curve of 30CuFeCNTs. One low intensity peak appeared at about 100 °C-300 °C. This may relate to the desorption of molecular CO_2 [28]. Another strong peak was at higher temperature (555 °C). As for 30CuFeTUD-1, there were three kinds of basic sites, a strong intensity peak appeared at low temperature region (~130 ºC), and two overlapping peaks appeared at high temperature region (between 400 °C and 800 °C).

For Fe based-catalysts, there are two modes of CO_2 adsorption, a weak one corresponding to desorption at 50 °C-200 °C and a strong one where desorption is at 190-400 °C [29], so the peak at ~130 °C is attributed to the CO_2 desorption from Fe surface. Sandoval *et al.* [30] found that the multilayer adsorption of CO_2 only happened at very low adsorption temperature (below 193K), it was difficult to detect the signal of CO_2 when the adsorption temperature increased to ambient temperature, and the CO_2 can be dissociated on the surface of Cu/SiO_2 catalyst, so it is a little difficult to observe the CO_2 desorption peak on Cu surface. The CO_2 desorption peak at 555 °C may be due to peroxides species on the surface of carbon nanotubes [31-33]. The two types of strong basic sites at a wide temperature range (250 °C-800 °C) may be attributed to the TUD-1 support.
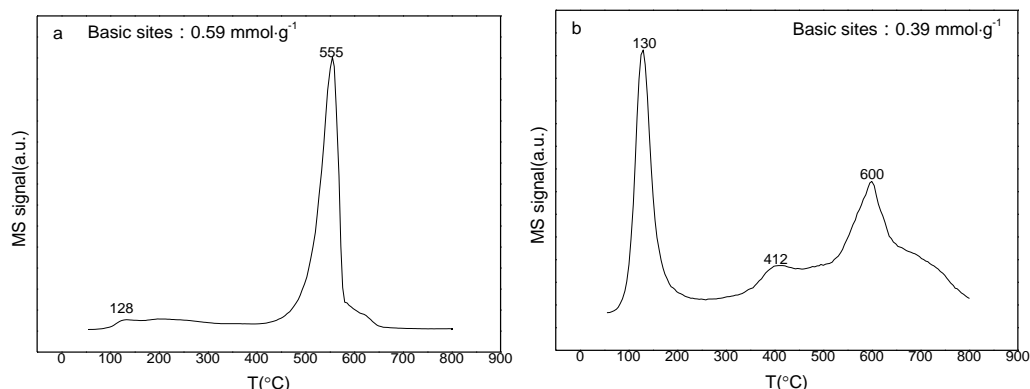
Figure 58 The CO$_2$ desorption profiles of a) 30CuFeCNTs and b) 30CuFeTUD-1

The basic sites were calculated in Figure 58, there are more basic sites on the surface of 30CuFeCNTs than it on the surface of 30CuFeTUD-1 and of much stronger strength.

To summarize the results of NH$_3$-TPD and CO$_2$-TPD, the acid-base property of surface was deeply dependent on the supports. The basic sites were more numerous than acid sites for both catalysts. 30CuFeCNTs owns relative more basic sites, and of higher strength, whereas 30CuFeTUD-1 presents relative more acid sites, but of similar strength.

IV.2.12 The XRD pattern after partial reduction

The XRD pattern of 30CuFeTUD-1 after reduction at 400 °C for 1 h is shown in Figure 59. There are only Cu and Fe metal in the catalyst after reduction. The H$_2$ consumption during this partial reduction was 2.2 mmol·g^{-1}. Compared to the total H$_2$ consumption in Table 23 of 4.4 mmol·g^{-1}, there are only 50% of reducible metals that have been reduced. This is consistent with the fact that this material is much more difficult to be reduced than CuFe-precursor-800 in chapter III.
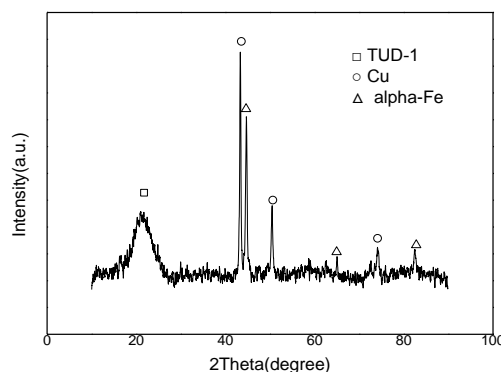
Figure 59 The XRD pattern of 30CuFeTUD-1 after reduction at 400°C for 1h

IV.2.13 Conclusions for the characterizations

➢ Catalysts with CNTs as support can be totally reduced. 30CuFeTUD-1 is more difficult to be reduced, only 50% can be reduced at 400 °C.

➢ 50CuFeCNTs has the highest metallic surface of copper and iron, 19.7 m^2·g^{-1}$_{cata}$ and 26.6 m^2·g^{-1}$_{cata}$ respectively.

➢ The basic sites were more numerous than acid sites for both catalysts. 30CuFeCNTs owns relative more basic sites, and of higher strength, whereas 30CuFeTUD-1 presents relative more acid sites, but of similar strength.

IV.3 Reaction results

The catalysts are tested under 50 bar and the temperature is 250 °C, 300 °C and 350 °C. The GHSV is 5000 h^{-1} (STP). The total flow rate is 50.0 mL·min^{-1} which includes 36.1 mL·min^{-1} of H$_2$, 12.0 mL·min^{-1} of CO$_2$, and 1.9 mL·min^{-1} of N$_2$. The volume of the catalysts bed is 0.6 cm^3. Before reaction, the catalyst is reduced at 400 °C for 1 h under pure H$_2$, the flow rate of H$_2$ is 11.8 mL·min^{-1}. The flow rate of feed gas was kept constant, so the mass of catalysts adjusted with respect to the apparent density. The mass of catalysts used for the reaction is shown in Table 25.

Table 25 The mass of catalyst used in reaction

Catalysts	Mass (g)
10CuFeCNTs	0.1011
30CuFeCNTs	0.1340
50CuFeCNTs	0.1813
70CuFeCNTs	0.3434
30CuFeTUD-1	0.4267

The CO_2 and H_2 conversion of catalysts 10CuFeCNTs, 30CuFeCNTs, 50CuFeCNTs, 70CuFeCNTs and 30CuFeTUD-1 at 250 °C, 300 °C and 350 °C are shown in Figure 60 and Figure 61. For all the catalysts, the reactivity at 250 °C is very low. Both the conversions of CO_2 and H_2 are lower than 10%. With the reaction temperature increase from 250 °C to 350 °C, the conversions of CO_2 were sharply increased up to more than 30% except for 10CuFeCNTs and 30CuFeTUD-1. The conversions of H_2 were also increased a lot, especially for catalysts 30CuFeCNTs, 50CuFeCNTs and 70CuFeCNTs, for which the conversion of H_2 were increased up to around 40% for the three catalysts. The catalyst 50CuFeCNTs presents the highest CO_2 and H_2 conversions, 34.1% and 43.4% respectively, at 350 °C. The CO_2 and H_2 conversions are similar with 30CuFeCNTs and 70CuFeCNTs: the CO_2 conversion is 19.3% and 20.6% at 300 °C, 33.5% and 33.0% at 350 °C respectively; the H_2 conversions are at 19.4% and 22.1% at 300 °C, and 39.1% and 40.1% at 350 °C respectively. For 10CuFeCNTs, because of the low loading of active phases, the CO_2 and H_2 conversion are less than 10% even at 350 °C, and the reactivity of 10CuFeCNTs at 250 °C is too low to be analyzed.

The CO_2 and H_2 conversions of CuFe on CNTs as support were much higher than for CuFe on TUD-1 as support at the same loading of CuFe of 30 %. For example, at 350 °C the CO_2 conversion is 33.5 % for 30CuFeCNTs compared to

21.9% for 30CuFeTUD-1.

Comparing to the results obtained on CuFe-precursor-800 in chapter III (CO_2 conversions are 10.1%, 22.6%, 29.8% at 250 °C, 300 °C and 350 °C respectively and H_2 conversions are 8.8%, 23.3%, 31.2% at 250 °C, 300 °C and 350 °C respectively), the CO_2 and H_2 conversions of 30CuFeTUD-1 are lower at the three reaction temperature. For CuFe/CNTs catalysts, although the conversion of CO_2 and H_2 are lower at 250 °C and 300 °C, the conversions obtained at 350 °C are slightly higher than for CuFe-precursor-800.
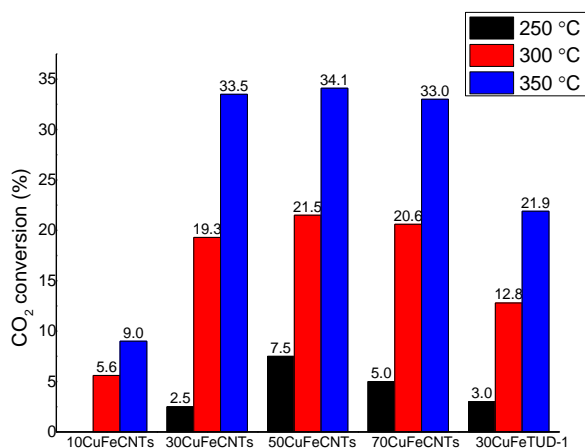
Figure 60 The CO_2 conversion of CuFe-based supported catalysts at 250 °C, 300 °C and 350 °C
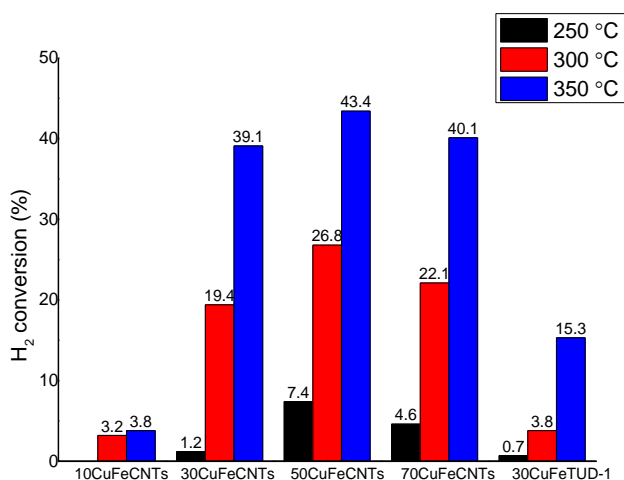
Figure 61 The H_2 conversion of CuFe-based supported catalysts at 250 °C, 300 °C and 350 °C

The selectivities and productivities of CO, alcohols (methanol and higher alcohols), hydrocarbons (methane, C_{2-5} hydrocarbons, C_{5+} hydrocarbons) and other oxygenates are displayed in Table 26 and Table 27.

The effect of temperature on the distribution of products

The main products of 30CuFeTUD-1 as catalyst are methanol and CO. At 250 °C, the selectivity to methanol is as high as 46.8% and the productivity is 47.5 $g \cdot kg^{-1} \cdot h^{-1}$. With the temperature increase to 350 °C, the selectivity to methanol decreases to 16.5% (productivity increases to 124.5 $g \cdot kg^{-1} \cdot h^{-1}$) whereas the selectivity to CO increases from 50.3% to 61.9% (productivity of CO increased from 23.9 $g \cdot kg^{-1} \cdot h^{-1}$ to 234.1 $g \cdot kg^{-1} \cdot h^{-1}$). More than 97% of alcohols produced is methanol, so the total selectivities to alcohols also decreased with reaction temperature increase (from 46.9% to 16.9% at temperature of 250 °C and 350 °C). The selectivity to hydrocarbons is very low for this catalyst at 250 and 300 °C (around 5 %). It reaches 21 % at 350 °C, methane being the main product in this fraction. This catalyst failed to increase the carbon chain. According to the mechanism of CO₂ synthesis to higher alcohols, the first step of the reaction is the RWSR, and the second step is synthesis of higher alcohols from $CO+H_2$ or CO_2+CO+H_2. The activity can be improved by increasing the active sites of Fe which works well at the growth of carbon chain.

For the 10CuFeCNTs, the active phases are too low to have enough reactivity, around 90% of C converted leads to CO.

For 30CuFeCNTs, low temperature (250 °C) is beneficial to the formation of single-carbon products, and more than 90% of products are CO and CH₄. When the temperature increases to 300 °C, the selectivity to C_{2+} hydrocarbons increase a lot (from 6.0% to 30.9%), the selectivity to higher alcohols also increases from 0.5% to 4.9%, and the productivity increases to 42.8 $g \cdot kg^{-1}_{cat} \cdot h^{-1}$. The maximum selectivity to higher alcohols is obtained for the reaction at 350 °C, 7.7%, and the productivity reaches to 108.9 $g \cdot kg^{-1} \cdot h^{-1}$. The selectivity to C_{2+} hydrocarbons also increased to

42.4%. The CO and CH$_4$ production was largely diminished, the selectivities decreased from 50.3% to 13.9% and 40.2% to 34.1% respectively with temperature from 250 °C to 350 °C.

For the 50CuFeCNTs, the most suitable temperature for the synthesis of higher alcohols is 300 °C, the highest selectivities and productivities to higher alcohols, 8.9% and 74.8 g·kg^{-1}·h^{-1} respectively are obtained. The single-carbon products (methanol and CO) kept decreasing with reaction temperature increase from 250 °C to 350 °C. The selectivity to methanol decreased from 7.2% to 1.2% and selectivity to methane decreased from 31.1% to 9.9%. High temperature is also beneficial to the synthesis of C$_{2+}$ hydrocarbons. The selectivity and productivity of C$_{2+}$ hydrocarbons reach 49.2% and 394.2 g·kg^{-1}·h^{-1} at 350 °C.

For the 70CuFeCNTs the increase of temperature is beneficial to the synthesis of C$_{2+}$ hydrocarbons and the selectivities increased from 19.7% to 49.3%. The selectivities to CO, alcohols and methane decreased. The highest productivities of higher alcohols is only 18.5 g·kg^{-1}·h^{-1} at 350 °C.

The effect of the loading of CuFe on the distribution of products

When HAS reactions were taken at 250 °C, the selectivities to alcohols (methanol and higher alcohols) and total hydrocarbons increased with the loading of CuFe. But the maximum productivities is obtained for 50CuFeCNTs because of the relative high CO$_2$ conversion. Selectivity to CO decreased from 50.3% to 21.5% with the increase of CuFe loading, but the highest productivity is also obtained for the reaction with 50CuFeCNTs as catalyst. The tendency of selectivities to CH$_4$ and C$_{2+}$ hydrocarbons is totally inverse, the selectivity of CH$_4$ first increased when the loading of CuFe at 44.9%, but decreased at the loading of 49.6% (results of elemental analysis).

For the reaction at 300 °C, the highest selectivities and productivities of alcohols (methanol and higher alcohols) and C$_{2+}$ hydrocarbons happened in the reaction with 50CuFeCNTs as catalyst. The low loading of CuFe is benefit to the formation of CO,

and the selectivity decreased with the loading increased. On the contrary to CO, the selectivities to total hydrocarbons increased with the loading of CuFe. The synthesis of CH_4 and C_{2+} hydrocarbons is competitive, when the selectivity of methane increased, the selectivities of C_{2+} hydrocarbons decreased.

For the reaction at 350 °C，the highest selectivities and productivities of higher alcohols were obtained in the reaction with 30CuFeCNTs as catalyst, the selectivities and productivities are 8.7% and 108.9 $g \cdot kg^{-1} \cdot h^{-1}$ respectively. The selectivity to CO sharply decreased from 86.5% to 9.8% with the loading of CuFe increased from 6.4% to 49.6% (results of elemental analysis). For the total hydrocarbons, the selectivities also increased with the Cu-Fe loading. So a suitable ratio of catalysts to carbon nanotubes and reaction temperature are required and impact the distribution of the products.

The comparison of CNTs and TUD-1 supports on the distribution of products

30CuFeTUD-1 is more suitable for the synthesis of CO and methanol, the selectivity to CO is much higher than for 30CuFeCNTs, especially at 350 °C. The selectivity to CO is 13.9% and 61.9% for 30CuFeCNTs and 30CuFeTUD-1 respectively. There is 46.8% of methanol in the products for 30CuFeTUD-1 as catalyst at 250 °C, meanwhile, only 2.9% of methanol was obtained in the products for 30CuFeCNTs as catalyst. There are more hydrocarbons and higher alcohols in the products of 30CuFeCNTs as catalyst.

The comparison of the distribution of products with catalyst CuFe-precursor-800 of chapter III

Compared to CuFe-precursor-800 in chapter III, when the catalysts are supported by CNTs, the selectivities to higher alcohols increased a little, but the productivities increased a lot. The highest productivities of higher alcohols is 108.9 $g \cdot kg^{-1} \cdot h^{-1}$, which

was obtained with 30CuFeCNTs as catalyst at 350 °C. This is around ten times higher than CuFe-precursor-800 as catalyst (11.2 g·kg^{-1}·h^{-1}) at the same temperature, because much less catalysts were used in the reactions of CuFe/CNTs. The selectivity to CO increased with temperature for catalysts supported by CNTs, but decreased for CuFe-precursor-800.

Compared to CuFe-precursor-800, The TUD-1 inhibited the synthesis of hydrocarbons, but increased the selectivity to CO and methanol.

As a conclusion for the reaction results, there is a balance between the metal or metal oxides active phases with the supports and reaction temperature. The catalysts with CNTs as supports are efficient for carbon chain growth, and lead to increased selectivities and productivities to the alcohols at high temperature. When TUD-1 is used as support only CO and methanol are produced.

Table 26 The selectivities to CO, alcohols, methanol, higher alcohols, hydrocarbon, CH_4, C_{2-5}, C_{5+} and other oxygenates

of CuFe-based supported catalysts

Catalysts	T/ ℃	CO_2 conversion (%)	Selectivities (mol. %)								
			CO	Alcohols (total)	Methanol	Higher alcohols	Hydrocarbons (total)	CH_4	C_{2-5}	C_{5+}	Other oxygenates
30CuFeCNTs		2.5	50.3	3.4	2.9	0.5	46.2	40.2	6.0	0.0	0.0
50CuFeCNTs	250	7.5	31.1	12.5	7.2	5.3	56.4	29.3	24.4	1.5	0.4
70CuFeCNTs		5.0	21.5	15.6	12.1	3.5	62.8	42.8	18.7	1.0	0.0
30CuFeTUD-1		3.0	47.1	46.9	46.8	0.2	5.8	2.5	3.1	0.2	0.0
10CuFeCNTs		5.6	88.0	2.2	0.8	1.5	9.8	5.9	3.6	0.1	0
30CuFeCNTs		19.3	22.8	8.9	3.9	4.9	68.2	35.3	30.9	0.9	0.0
50CuFeCNTs	300	21.5	13.5	13.2	4.3	8.9	73.3	29.1	41.0	2.6	0.6
70CuFeCNTs		20.6	14.3	6.6	3.2	3.4	78.5	36.2	39.2	2.6	0.3
30CuFeTUD-1		12.8	60.9	34.8	34.7	0.1	4.3	3.1	1.2	0.0	0.0
10CuFeCNTs		9.0	86.5	2.0	0.7	1.4	11.5	7.7	3.5	0.1	0
30CuFeCNTs		33.5	13.9	9.3	1.6	7.7	76.5	34.1	40.2	2.2	0.3
50CuFeCNTs	350	34.1	9.9	6.6	1.2	5.4	83.5	33.7	46.2	3.0	0.6
70CuFeCNTs		33.0	9.8	4.1	1.2	2.9	85.5	35.6	46.9	2.4	0.6
30CuFeTUD-1		21.9	61.9	16.9	16.5	0.5	21.1	14.7	6.3	0.1	0.0

Table 27 The productivities of CO, alcohols, methanol, higher alcohols, hydrocarbon, CH$_4$, C$_{2-5}$, C$_{5+}$ and other oxygenates

of CuFe-based supported catalysts

Catalysts	T/ °C	CO$_2$ conversion (%)	Productivities (g·kg^{-1}·h^{-1})								
			CO	Alcohols (Total)	Methanol	Higher alcohols	Hydrocarbons	CH$_4$	C$_{2-5}$	C$_{5+}$	Other oxygenates
30CuFeCNTs		2.5	73.4	9.1	8.5	0.6	38.3	33.6	4.7	0.0	0.0
50CuFeCNTs	250	7.5	122.5	73.1	56.1	16.1	122.1	66.1	52.2	3.8	1.5
70CuFeCNTs		5.0	28.0	35.2	31.5	3.7	45.7	31.9	13.0	0.8	0.1
30CuFeTUD-1		3.0	23.9	47.6	47.5	0.1	1.6	0.7	0.8	0.1	0.0
10CuFeCNTs		5.6	164.8	5.1	2.9	2.2	10.2	6.4	3.7	0.1	0
30CuFeCNTs		19.3	244.6	127.6	84.9	42.8	401.1	217.2	177.1	6.8	0.0
50CuFeCNTs	300	21.5	144.0	167.9	93.1	74.8	430.0	178.6	236.3	15.	4.1
70CuFeCNTs		20.6	74.6	46.9	33.7	13.2	225.1	108.1	111.6	5.4	1.5
30CuFeTUD-1		12.8	138.6	158.4	158.2	0.2	5.5	4.0	1.4	0.0	0.0
10CuFeCNTs		9.0	377.1	10.6	5.8	4.8	27.9	19.3	8.3	0.4	0.1
30CuFeCNTs		33.5	244.3	167.0	58.1	108.9	743.7	343.3	377.8	22.	5.9
50CuFeCNTs	350	34.1	149.7	99.0	35.5	63.5	686.4	292.1	372.5	21.	10.9
70CuFeCNTs		33.0	78.0	38.7	20.2	18.5	370.4	161.9	197.8	10.	4.4
30CuFeTUD-1		21.9	234.1	126.0	124.5	1.5	44.6	31.7	12.6	0.2	0.1

IV.4 Characterization after test

IV.4.1 X-Ray Diffraction after reaction

The XRD patterns of catalysts after reaction are shown in Figure 62. There are iron carbides in the catalyst after reaction of the catalysts with CNTs as support. The iron carbides are thought to be the active sites of Fischer-Tropsch synthesis [34]. There are also Cu and Fe mixed oxides in the catalysts after reaction. For TUD-1 as support, there are only Fe oxide and metallic Cu or CuFe alloy in the catalyst.
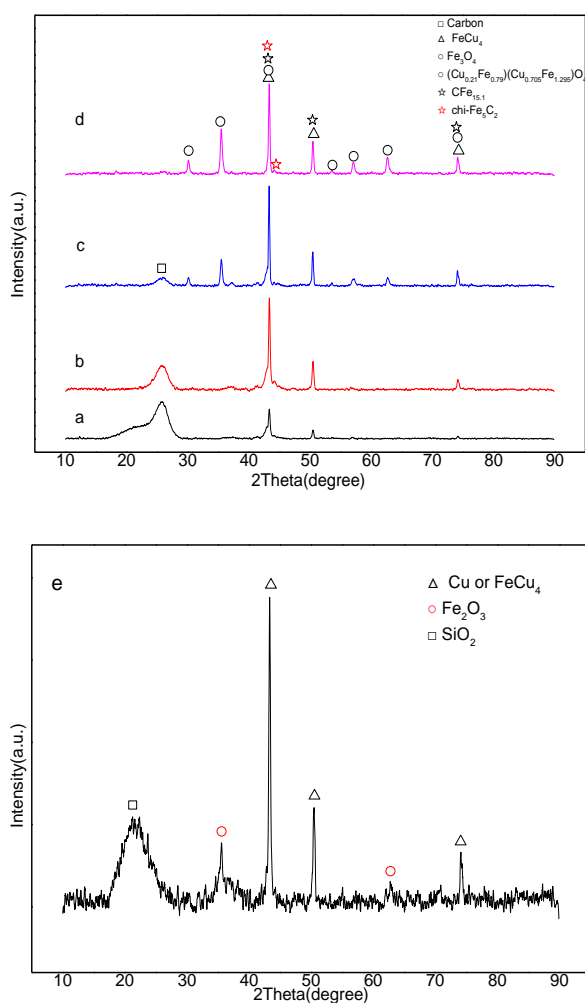
Figure 62 the XRD pattern of (a) 10CuFeCNTs, (b) 30CuFeCNTs,

(c) 50CuFeCNTs and (d) 70CuFeCNTs (e) 30CuFeTUD-1 after reaction

Comparing the XRD patterns of CNTs and TUD-1 as supports after reaction, we found that the carbon nanotube can promote the formation of iron carbides, which can be benefit to carbon chain growth. The Fe_2O_3 was thought to be the active phase of RWGS reaction [34], so there were mainly CO and methanol in the catalyst with TUD-1.

IV.4.2 TEM after reaction

The TEM images of 30CuFeCNTs after reaction are shown in Figure 63, there are typical core-shell structure in the catalyst after reaction. The diameter of core is around 18nm and the thickness of shell is around 3-8nm. Lattice spacing of the core is 0.20 nm. The lattice space of 0.23 corresponds to $CFe_{15.1}$ (111) [35], and lattice spacing of alpha-Fe (110) is 0.20 nm, which is similar to Fe_5C_2 (510) 0.205 nm [36], meanwhile, the CuFe alloy (111) exhibits a d-spacing of 0.22 nm. There are maybe Fe_5C_2 or alpha-Fe in the structure.

Combined to the results of XRD, the existence of Fe_5C_2 can be proposed. The lattice spacing of shell is around 0.36nm, which is attributed to CNTs.
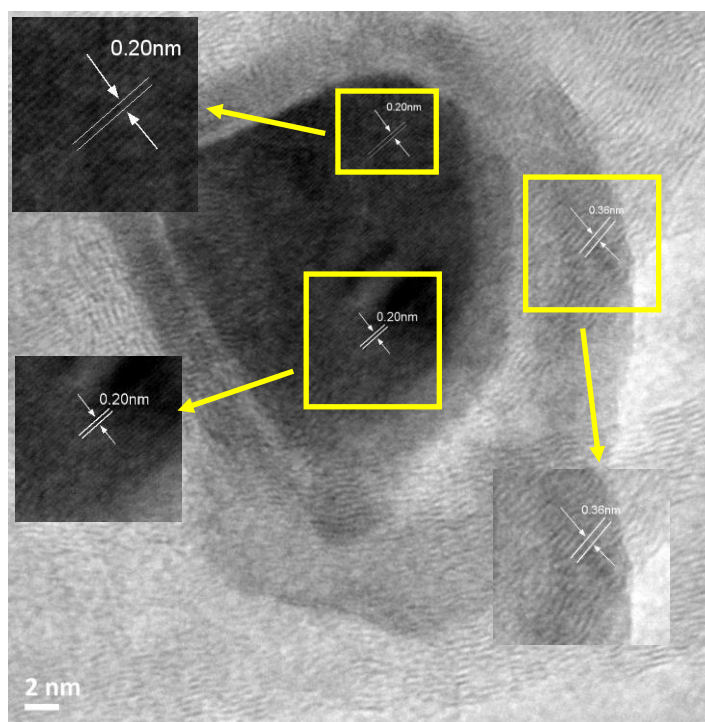
Figure 63 The TEM images of 30CuFeCNTs after reaction

IV.5 Discussion

At similar CuFe loading, the conversions of CO_2 and H_2 with CNTs are much higher than with TUD-1 at high temperature (300 °C and 350 °C), and the distribution of products is totally different. Yang found that the dissociative activation of H_2 was more difficult than activation of CO, and HAS reaction only happened after the dissociation of H_2 [37], so the activation of H_2 is a rate-determining step. The special sp^2-C surface of CNTs can not only help adsorption but also activate hydrogen and provide a micro-environment with higher stationary-state concentration of H-adspecies on the functioning catalyst. These active H-species adsorbed at surface of the CNTs could be readily transferred to metal active sites *via* the CNT-assisted hydrogen spillover [38]. The special surface property decides that the catalyst with CNTs own higher conversion.

The distribution of products are totally different with carbon nanotubes and TUD-1 as support, there are several reasons.

The first reason may be explained from the mechanism of higher alcohols synthesis. For the HAS reaction, dual sites is necessary and on the Cu modified F-T based catalyst, the active sites is Cu-M (M= F-T element) [39, 40]. The role of Fe is CO adsorption and dissociation and to promote the growth of carbon chains, meanwhile, Cu can adsorbe CO which can then be inserted into the carbon chain. The synergistic effect between Cu and Fe is key to alcohol formation [39]. A lot of researchers [41] found that FeC_x instead of Fe was the true active sites for CO dissociation and carbon chain propagation, so the real dual sites for higher alcohols synthesis is Cu-FeC_x, CO was adsorbed on the surface of FeC_x and dissociated and form surface CH_x monomer by hydrogenation, which initiates carbon chain propagation to form surface alkyl species. The surface alkyl species on FeC_x migrate to adjacent Cu site and combine with CO molecule, and then form surface acyl species [42]. The surface acyl species can be hydrogenated and form alcohols [39]. From the results of XRD patterns of catalysts after reaction, the iron carbides are

easily formed in the catalysts with carbon nanotubes as support, but no iron carbides was evidenced on the catalyst with TUD-1 as support. This is maybe the main reason responsible for the mainly single carbon compounds in the products of 30CuFeTUD-1.

The second reason maybe due to the different surface property. From the results of NH_3-TPD and CO_2-TPD, there are more basic sites and less acid sites in catalyst with CNTs as support than for the catalyst with TUD-1 as support, which may affect the distribution. Wang *et al.* [43] have studied the effect of ZrO_2, Al_2O_3 and La_2O_3 to the Co-Cu catalysts for higher alcohols synthesis. They found that the selectivity to higher alcohols on $CuCoLa_2O_3$ (34.9%) is far greater than for $CuCoAl_2O_3$ (13.1%) or $CuCoZrO_2$ (17.8%). La_2O_3 appeared to be more reactive, and a higher reactivity is usually linked to stronger basicity [44]. According to the results of ammonia and pyridine adsorption the ranking of Lewis acidity is: CoO, CuO, CaO < Ni_2O_3 < MgO < NiO < ZrO_2 < Cr_2O_3 < ZnO < TiO_2 < Al_2O_3, and the Lewis acidity of ZrO_2 is similar to that of La_2O_3[44], but compared to the medium and strong basic sites of La_2O_3, there is only negligible amount of weak basic sites on the surface of ZrO_2 [45], so the surface basicity is really important for the growth of carbon chain and synthesis of higher alcohols synthesis. Ernst *et al.* [46] also found that, the basicity of promoted catalysts can apparently increase the conversion of CO and increase the selectivity to C_{5+} together with high olefins/paraffins ratios during CO hydrogenation. The high surface-concentration of H-adspecies led to a greater inhibition for the RWGS reaction, so there are much less CO in the reaction with CNTs as support.

The loading of metal active phases can also effect the distribution of products. A suitable loading can not only promote the interaction between metals and support but also help to obtain the expected products. Metals with a few vacant d-orbitals (Ni, Fe, Co) have a higher affinity with carbon nanotubes and the strong metal-carbon bonds can lead to the formation of stable carbides [16], which are the important active phases for the CO_2 hydrogenation. From the results of SEM in Figure 46, we found that the high loading of metals precursor may lead to big metals particles on the surface of carbon nanotubes, which may decrease the interaction of metals with

support.

Temperature can also deeply affect the distribution of products. For the selectivities and productivities to higher alcohols, 300 °C is a suitable reaction temperature for catalyst 50CuFeCNTs and 350 °C is benefit for catalyst 30CuFeCNTs, under our reaction conditions.

The highest selectivities to higher alcohols has been obtained in the reaction of 30CuFeCNTs at 350 °C and the highest productivities of higher alcohols is 108.9 $g \cdot kg^{-1} \cdot h^{-1}$. This is higher than the results reported in literature at the similar conditions. The highest productivity to higher alcohols is 34.1 $g \cdot kg^{-1} \cdot h^{-1}$, reported by Li *et al.* [47] at 60bar and 300 °C on a K/Cu-Zn catalyst.

IV.6 Conclusions

In conclusion, the study shows that a proper support and suitable loading of active phases can deeply affect the distribution of products. The CNTs can promote the synthesis of iron carbide, which is essential for the Fischer-Tropsch reactivity. The TUD-1 support are more suitable for synthesis of single-carbon products. CNTs is a perfect support for the synthesis of long-chain products. Suitable modification of the catalyst surface could further improve the productivity to higher alcohols.

IV.7 References

[1] M. Gupta, M.L. Smith, J.J. Spivey, Heterogeneous Catalytic Conversion of Dry Syngas to Ethanol and Higher Alcohols on Cu-Based Catalysts, Acs Catalysis, 1 (2011) 641-656.

[2] X.Y. Quek, D.P. Liu, W.N.E. Cheo, H. Wang, Y. Chen, Y.H. Yang, Nickel-grafted TUD-1 mesoporous catalysts for carbon dioxide reforming of methane, Appl Catal B-Environ, 95 (2010) 374-382.

[3] H.B. Zhang, X.L. Liang, X. Dong, H.Y. Li, G.D. Lin, Multi-Walled Carbon Nanotubes as a Novel Promoter of Catalysts for CO/CO₂ Hydrogenation to Alcohols, Catalysis Surveys from Asia, 13 (2009) 41-58.

[4] J. Liu, Z. Guo, D. Childers, N. Schweitzer, C.L. Marshall, R.F. Klie, J.T. Miller, R.J. Meyer, Correlating the degree of metal-promoter interaction to ethanol selectivity over MnRh/CNTs CO hydrogenation catalysts, Journal of Catalysis, 313 (2014) 149-158.

[5] R. Anand, R. Maheswari, U. Hanefeld, Catalytic properties of the novel mesoporous aluminosilicate AlTUD-1, Journal of Catalysis, 242 (2006) 82-91.

[6] S. Storck, H. Bretinger, W.F. Maier, Characterization of micro- and mesoporous solids by physisorption methods and pore-size analysis, Appl Catal A Gen, 174 (1998) 137-146.

[7] B.Q. Wei, M. Shima, R. Pati, S.K. Nayak, D.J. Singh, R.Z. Ma, Y.B. Li, Y. Bando, S. Nasu, P.M. Ajayan, Room-temperature ferromagnetism in doped face-centered cubic Fe nanoparticles, Small, 2 (2006) 804-809.

[8] G.P. Shpen′kov, Friction surface phenomena, Elsevier, 1995.

[9] D. Predoi, E. Andronescu, M. Radu, M.C. Munteanu, A. Dinischiotu, Synthesis and Characterization of Bio-Compatible Maghemite Nanoparticles, Dig J Nanomater Bios, 5 (2010) 779-786.

[10] L.R. Radovic, Chemistry & physics of carbon, CRC Press, 2004.

[11] J.B. Mu, B. Chen, Z.C. Guo, M.Y. Zhang, Z.Y. Zhang, P. Zhang, C.L. Shao, Y.C. Liu, Highly dispersed Fe_3O_4 nanosheets on one-dimensional carbon nanofibers: Synthesis, formation mechanism, and electrochemical performance as supercapacitor electrode materials, Nanoscale, 3 (2011) 5034-5040.

[12] H. Yan, M. Zhang, H. Yan, Electrical transport, magnetic properties of the half-metallic Fe_3O_4-based Schottky diode, Journal of Magnetism and Magnetic Materials, 321 (2009) 2340-2344.

[13] A. Fujimori, M. Saeki, N. Kimizuka, M. Taniguchi, S. Suga, Photoemission Satellites and Electronic-Structure of Fe_2O_3, Phys Rev B, 34 (1986) 7318-7333.

[14] J.N. Fiedor, W.D. Bostick, R.J. Jarabek, J. Farrell, Understanding the mechanism of uranium removal from groundwater by zero-valent iron using X-ray photoelectron spectroscopy, Environmental science & technology, 32 (1998) 1466-1473.

[15] H.L. Zhuang, G.P. Zheng, A.K. Soh, Interactions between transition metals and defective carbon nanotubes, Comp Mater Sci, 43 (2008) 823-828.

[16] F. Banhart, Interactions between metals and carbon nanotubes: at the interface between old and new materials, Nanoscale, 1 (2009) 201-213.

[17] S. Kameoka, T. Tanabe, A.P. Tsai, Spinel $CuFe_2O_4$: a precursor for copper catalyst with high thermal stability and activity, Catalysis Letters, 100 (2005) 89-93.

[18] E. vanSteen, G.S. Sewell, R.A. Makhothe, C. Micklethwaite, H. Manstein, M. deLange, C.T. OConnor, TPR study on the preparation of impregnated Co/SiO_2 catalysts, Journal of Catalysis, 162 (1996) 220-229.

[19] X. Dong, H.B. Zhang, G.D. Lin, Y.Z. Yuan, K.R. Tsai, Highly active CNT-promoted Cu-ZnO-Al_2O_3 catalyst for methanol synthesis from $H_2/CO/CO_2$, Catalysis Letters, 85 (2003) 237-246.

[20] H.B. Zhang, X. Dong, G.D. Lin, X.L. Liang, H.Y. Li, Carbon nanotube-promoted Co-Cu catalyst for highly efficient synthesis of higher alcohols from syngas, Chemical Communications, (2005) 5094-5096.

[21] E. van Steen, F.F. Prinsloo, Comparison of preparation methods for carbon nanotubes supported iron Fischer-Tropsch catalysts, Catalysis Today, 71 (2002) 327-334.

[22] X. Yang, Y. Wei, Y. Su, L. Zhou, Characterization of fused Fe-Cu based catalyst for higher alcohols synthesis and DRIFTS investigation of TPSR, Fuel Processing Technology, 91 (2010) 1168-1173.

[23] G.D. Lin, X.L. Liang, Z.M. Liu, J.R. Xie, B.H. Chen, H.B. Zhang, Multi-walled carbon nanotubes as novel promoter of catalysts for certain hydrogenation and dehydrogenation reactions, Sci China Chem, 58 (2015) 47-59.

[24] C.H. Ma, H.Y. Li, G.D. Lin, H.B. Zhang, Ni-decorated carbon nanotube-promoted Ni-Mo-K catalyst for highly efficient synthesis of higher alcohols from syngas, Appl Catal B-Environ, 100 (2010) 245-253.

[25] W. Xia, X.L. Yin, S. Kundu, M. Sanchez, A. Birkner, C. Woll, M. Muhler, Visualization and functions of surface defects on carbon nanotubes created by catalytic etching, Carbon, 49 (2011) 299-305.

[26] F. Frusteri, M. Cordaro, C. Cannilla, G. Bonura, Multifunctionality of Cu-ZnO-ZrO₂/H-ZSM5 catalysts for the one-step CO₂-to-DME hydrogenation reaction, Appl Catal B-Environ, 162 (2015) 57-65.

[27] L. Rodriguez-Gonzalez, F. Hermes, M. Bertmer, E. Rodriguez-Castellon, A. Jimenez-Lopez, U. Simon, The acid properties of H-ZSM-5 as studied by NH₃-TPD and Al-27-MAS-NMR spectroscopy, Appl Catal A Gen, 328 (2007) 174-182.

[28] A.H.D. Batista, F.S.O. Ramos, T.P. Braga, C.L. Lima, F.F. de Sousa, E.B.D. Barros, J. Mendes, A.S. de Oliveira, J.R. de Sousa, A. Valentini, A.C. Oliveira, Mesoporous MAl2O4 (M = Cu, Ni, Fe or Mg) spinels: Characterisation and application in the catalytic dehydrogenation of ethylbenzene in the presence of CO₂, Appl Catal A Gen, 382 (2010) 148-157.

[29] J.C.S. de Araujo, C.B.A. Sousa, A.C. Oliveira, F.N.A. Freire, A.P. Ayala, A.C. Oliveira, Dehydrogenation of ethylbenzene with CO₂ to produce styrene over Fe-containing ceramic composites, Appl Catal A Gen, 377 (2010) 55-63.

[30] M.J. Sandoval, A.T. Bell, Temperature-Programmed Desorption Studies of the Interactions of H₂, CO, and CO₂ with Cu/SiO₂, Journal of Catalysis, 144 (1993) 227-237.

[31] J.H. Zhou, Z.J. Sui, J. Zhu, P. Li, C. De, Y.C. Dai, W.K. Yuan, Characterization of

surface oxygen complexes on carbon nanofibers by TPD, XPS and FT-IR, Carbon, 45 (2007) 785-796.

[32] U. Zielke, K.J. Huttinger, W.P. Hoffman, Surface-oxidized carbon fibers .1. Surface structure and chemistry, Carbon, 34 (1996) 983-998.

[33] D.M. Nevskaia, A. Santianes, V. Munoz, A. Guerrero-Ruiz, Interaction of aqueous solutions of phenol with commercial activated carbons: an adsorption and kinetic study, Carbon, 37 (1999) 1065-1074.

[34] M.Y. Ding, M.H. Qiu, J.G. Liu, Y.P. Li, T.J. Wang, L.L. Ma, C.Z. Wu, Influence of manganese promoter on co-precipitated Fe-Cu based catalysts for higher alcohols synthesis, Fuel, 109 (2013) 21-27.

[35] M.H. Chen, J.L. Liu, W.J. Zhou, J.Y. Lin, Z.X. Shen, Nitrogen-doped Graphene-Supported Transition-metals Carbide Electrocatalysts for Oxygen Reduction Reaction, Scientific reports, 5 (2015).

[36] V. Vij, J.N. Tiwari, W.G. Lee, T. Yoon, K.S. Kim, Hemoglobin-carbon nanotube derived noble-metal-free Fe$_5$C$_2$-based catalyst for highly efficient oxygen reduction reaction, Scientific reports, 6 (2016).

[37] X.M. Yang, Y. Wei, Y.L. Su, L.P. Zhou, Characterization of fused Fe-Cu based catalyst for higher alcohols synthesis and DRIFTS investigation of TPSR, Fuel Processing Technology, 91 (2010) 1168-1173.

[38] J.-J. Wang, J.-R. Xie, Y.-H. Huang, B.-H. Chen, G.-D. Lin, H.-B. Zhang, An efficient Ni–Mo–K sulfide catalyst doped with CNTs for conversion of syngas to ethanol and higher alcohols, Applied Catalysis A: General, 468 (2013) 44-51.

[39] K. Xiao, Z.H. Bao, X.Z. Qi, X.X. Wang, L.S. Zhong, M.G. Lin, K.G. Fang, Y.H. Sun, Unsupported CuFe bimetallic nanoparticles for higher alcohol synthesis via syngas, Catalysis Communications, 40 (2013) 154-157.

[40] K.G. Fang, D.B. Li, M.G. Lin, M.L. Xiang, W. Wei, Y.H. Sun, A short review of heterogeneous catalytic process for mixed alcohols synthesis via syngas, Catalysis Today, 147 (2009) 133-138.

[41] M.D. Shroff, D.S. Kalakkad, K.E. Coulter, S.D. Kohler, M.S. Harrington, N.B. Jackson, A.G. Sault, A.K. Datye, Activation of Precipitated Iron Fischer-Tropsch

Synthesis Catalysts, Journal of Catalysis, 156 (1995) 185-207.

[42] A. Kiennemann, A. Barama, S. Boujana, M.M. Bettahar, Higher Alcohol Synthesis on Modified Iron-Based Catalysts - Copper and Molybdenum Addition, Appl Catal A Gen, 99 (1993) 175-194.

[43] Z. Wang, J.J. Spivey, Effect of ZrO$_2$, Al$_2$O$_3$ and La$_2$O$_3$ on cobalt-copper catalysts for higher alcohols synthesis, Appl Catal A Gen, 507 (2015) 75-81.

[44] O.V. Manoilova, S.G. Podkolzin, B. Tope, J. Lercher, E.E. Stangland, J.M. Goupil, B.M. Weckhuysen, Surface acidity and basicity of La$_2$O$_3$, LaOCl, and LaCl$_3$ characterized by IR spectroscopy, TPD, and DFT calculations, Journal of Physical Chemistry B, 108 (2004) 15770-15781.

[45] S. Kus, M. Otremba, M. Taniewski, The catalytic performance in oxidative coupling of methane and the surface basicity of La$_2$O$_3$, Nd$_2$O$_3$, ZrO$_2$ and Nb$_2$O$_5$, Fuel, 82 (2003) 1331-1338.

[46] B. Ernst, L. Hilaire, A. Kiennemann, Effects of highly dispersed ceria addition on reducibility, activity and hydrocarbon chain growth of a Co/SiO$_2$ Fischer-Tropsch catalyst, Catalysis Today, 50 (1999) 413-427.

[47] S.G. Li, H.J. Guo, C.R. Luo, H.R. Zhang, L. Xiong, X.D. Chen, L.L. Ma, Effect of Iron Promoter on Structure and Performance of K/Cu-Zn Catalyst for Higher Alcohols Synthesis from CO$_2$ Hydrogenation, Catalysis Letters, 143 (2013) 345-355.

Chapter V

The effect of alkalis metals (K, Na, Cs) on HAS from CO_2 hydrogenation by CuFe/CNTs catalyst

V.1 Introduction

From the results of chapter IV, it has been found that the deposition of Cu and Fe precursors on carbon nanotubes can effectively lead to a catalyst with increased selectivities and productivities to higher alcohols with respect to a massive CuFe-precursor-800 catalyst, but there are still more than 50% of hydrocarbons in the products distribution. Researchers found that the synthesis of hydrocarbons and dimethyl ether from CO_2/CO hydrogenation is strongly dependent on the acid sites on the surface of catalysts [1,2]. In order to inhibit the formation of hydrocarbons and increase selectivities to higher alcohols, different kinds of promoters included the alkalis are reported in literature [3-9]. The addition of optimum amount of alkalis as chemical promoters can neutralize the surface acidity [10], strongly suppress the production of CH_4 and facilitate the adsorption of CO_2. It is also reported that it allows the decrease of the selectivity to methanol to the benefit of linear primary higher alcohols [4].

In this chapter, a systematic investigation of alkalis promoted 30CuFeCNTs for the synthesis of higher alcohols from CO_2 hydrogenation will be done. The effect of K at different concentrations and Na, Cs as promoters on the product distribution will be discussed. According to the results, we try to find the beneficial dopants and concentration for the synthesis of higher alcohols.

V.2 The preparation of catalysts

The catalyst 30CuFeCNTs (typically 0.6g), prepared in Chapter IV, was used to deposit 1 wt% promoters (K, Na, Cs). For the potassium, catalysts with three concentrations (0.5, 1.0 and 1.5 wt%) were prepared. The pore volume impregnation method with an ethanol-water (50:50) alkalis carbonate solution was used. The concentrations of ions are shown in Table 28. After impregnation, the samples were

dried at 100 °C for 8 h. At last, the samples were annealed under N_2 atmosphere at 800 °C for 6 h with heating ramp 2 °C·min^{-1}.

Table 28 The volume and concentration of alkalis carbonates for the impregnation

Catalysts	Volume (mL)	Concentration of ions (mol · mL^{-1})
0.5K30CuFeCNTs	1.44	1.3×10^{-5}
1K30CuFeCNTs	1.44	2.5×10^{-5}
1.5K30CuFeCNTs	1.44	3.8×10^{-5}
1Cs30CuFeCNTs	1.44	7.4×10^{-6}
1Na30CuFeCNTs	1.44	4.3×10^{-5}

V.3 Catalysts characterizations

V.3.1 Composition and textural proprieties

The elemental analysis of catalysts is displayed in Table 29, and the BET surface, pore volume and density of catalysts are shown in Table 30. The experimental results are almost similar to expected theoretical contents.

Table 29 The elemental analysis of promoted catalysts

Catalysts	Experimental (wt %)			Theoretical (wt %)		
	K	Na	Cs	K	Na	Cs
0.5K30CuFeCNTs	0.08± 0.03	-	-	0.11	-	-
1K30CuFeCNTs	0.19 ± 0.03	-	-	0.22	-	-
1.5K30CuFeCNTs	0.25 ± 0.05	-	-	0.33	-	-
1Na30CuFeCNTs	-	0.26 ± 0.07	-	-	0.22	-
1Cs30CuFeCNTs	-	-	0.21 ± 0.06	-	-	0.22

The loading by promoters affected slightly the surface area, pore volume and density compared to 30CuFeCNTs discussed in chapter IV. All the BET surface areas

of promoted catalysts decreased except for 1Cs30CuFeCNTs. 1Cs30CuFeCNTs owns relatively higher surface area and pore volume than the other catalysts.

Table 30 The BET surface area, pore volume and density of promoted catalysts and of 30CuFeCNTs

Catalyst	BET surface area ($m^2 \cdot g^{-1}$)	Pore volume ($cm^3 \cdot g^{-1}$)	Density ($g \cdot cm^{-3}$)
0.5K30CuFeCNTs	269	0.92	0.25
1K30CuFeCNTs	269	0.91	0.25
1.5K30CuFeCNTs	251	0.91	0.23
1Na30CuFeCNTs	262	0.90	0.25
1Cs30CuFeCNTs	289	0.97	0.24
30CuFeCNTs	276	1.17	0.20

V.3.2 X-Ray Diffraction (XRD) before reaction

XRD pattern of catalysts are presented in Figure 64, which confirm the existence of CNTs, iron oxides, and small amounts of copper iron spinel in the catalysts. The diffractogramms of Cu (JCPDS 01-085-1326) or CuFe alloy (JCPDS 03-065-7002), iron carbide (00-052-0521) are similar, so it is difficult to detect that CuFe alloy or iron carbides exist in these catalysts. Compared to the XRD patterns of 30CuFeCNTs in chapter IV, part of copper iron spinel and Fe$_3$O$_4$ instead of metallic iron were formed, which is maybe due to the oxidation of iron during the impregnation step and further calcination.

Figure 64 The XRD profiles of catalysts of (a) 0.5K30CuFeCNTs, (b) 1K30CuFeCNTs, (c) 1.5K30CuFeCNs, (d) 1Na30CuFeCNTs, (e) 1Cs30CuFeCNTs and (g) 30CuFeCNTs

V.3.3 H$_2$ Temperature Programmed Desorption (H$_2$-TPD)

The H$_2$-TPD profiles of promoted catalysts are presented in Figure 65. Four peaks were found in the H$_2$ desorption curve. Similarly to the results of H$_2$-TPD of 30CuFeCNTs in chapter IV, the peaks between 100 °C and 400 °C (Part I) could be attributed to the weakly adsorbed molecular H$_2$ on surface of metals (Cu or Fe) [11] or metals alloy or carbon nanotubes [12]. The peaks at higher temperature (part II: higher than 400 °C) may be attributed to the desorption of strongly adsorbed H-species (dissociatively adsorbed H$_2$) [13] or the gasification of CNTs.
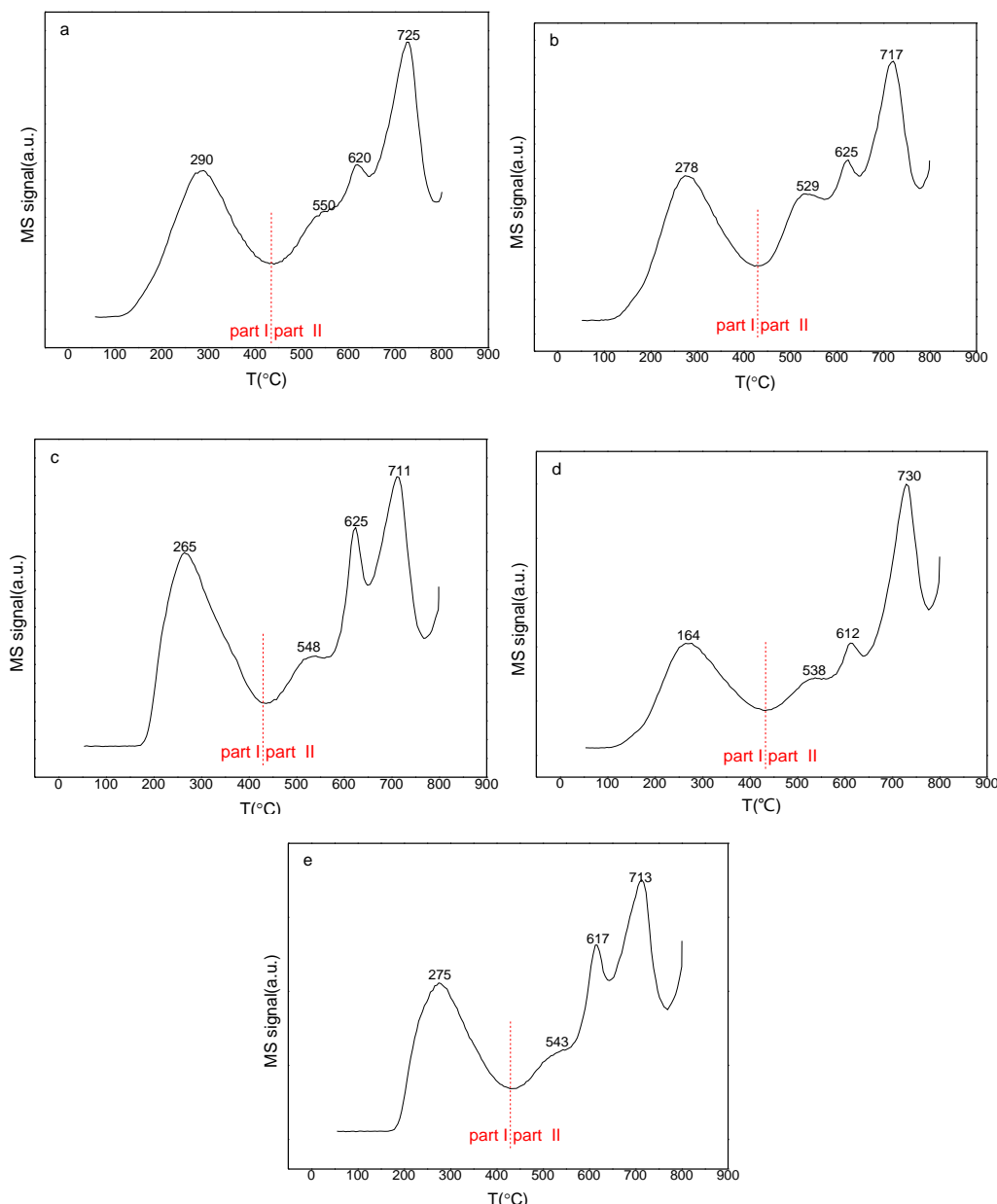
Figure 65 The H_2-TPD profiles of (a) 0.5K30CuFeCNTs, (b) 1K30CuFeCNTs, (c) 1.5K30CuFeCNTs, (d) 1Na30CuFeCNTs, (e) 1Cs30CuFeCNTs

The quantity of desorbed H_2 in Part I and Part II were calculated in Table 31, we can found that most of hydrogen adspecies corresponded to peaks in Part II. The quantity of weakly adsorbed H_2 on metallic surface (Part I) increased with the loading of K, and decreased in order K>Cs=Na. The H_2 desorption from the metallic phases (part I) of promoted catalysts are much higher than it from 30CuFeCNTs.

The calculation of the metallic surface has not been done because XPS studies were not performed an these materials and no information about Fe/Cu repartition at

the surface was available. Nevertheless, the value of hydrogen desorbed in part I is a good indicator of the amount of metallic surface.

Table 31 The quantity of desorbed H_2 on Part I and Part II and total desorbed H_2
at the surface of promoted-catalysts during H_2-TPD process

Catalysts	H_2 desorption (mol·g^{-1})		
	Part I	Part II	Total
0.5K30CuFeCNTs	4.7×10^{-5}	1.6×10^{-4}	2.1×10^{-4}
1K30CuFeCNTs	5.9×10^{-5}	2.3×10^{-4}	2.9×10^{-4}
1.5K30CuFeCNTs	6.4×10^{-5}	1.9×10^{-4}	2.6×10^{-4}
1Na30CuFeCNTs	5.6×10^{-5}	1.7×10^{-4}	2.3×10^{-4}
1Cs30CuFeCNTs	5.6×10^{-5}	1.7×10^{-4}	2.3×10^{-4}
30CuFeCNTs	3.4×10^{-5}	5.2×10^{-4}	5.5×10^{-4}

V.3.4 CO_2 Temperature Programmed Desorption (CO_2-TPD)

CO_2-TPD are performed to study the change of intensity and strength of surface basic sites on alkalis promoted catalysts. The profiles are shown in Figure 66 and the basic sites are calculated in Table 32. The amount of basic sites of promoted catalysts are much higher than for 30CuFeCNTs, except for 0.5K30CuFeCNTs.
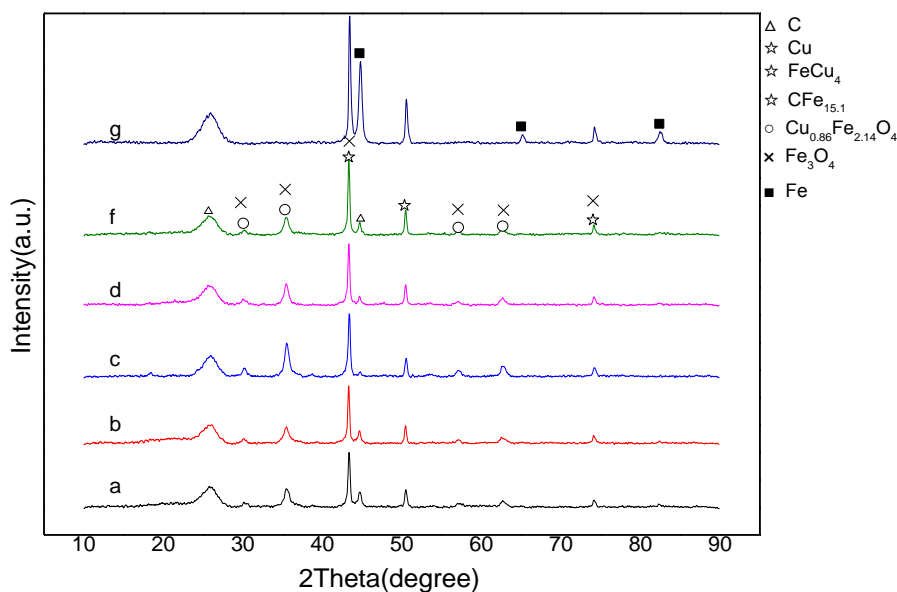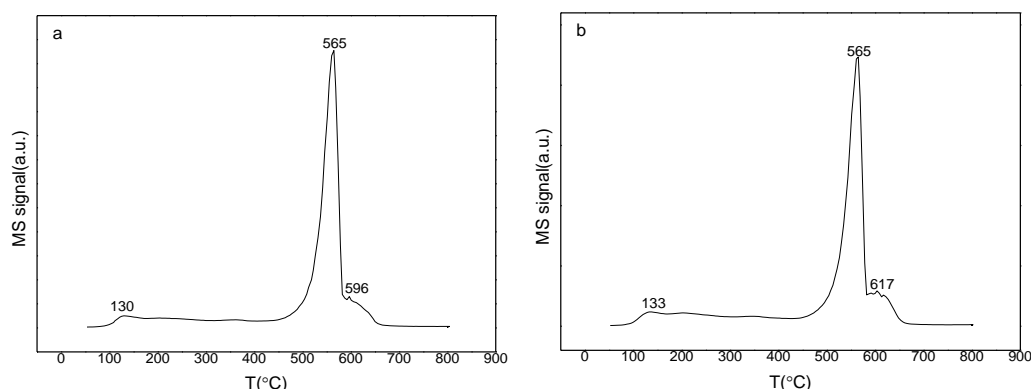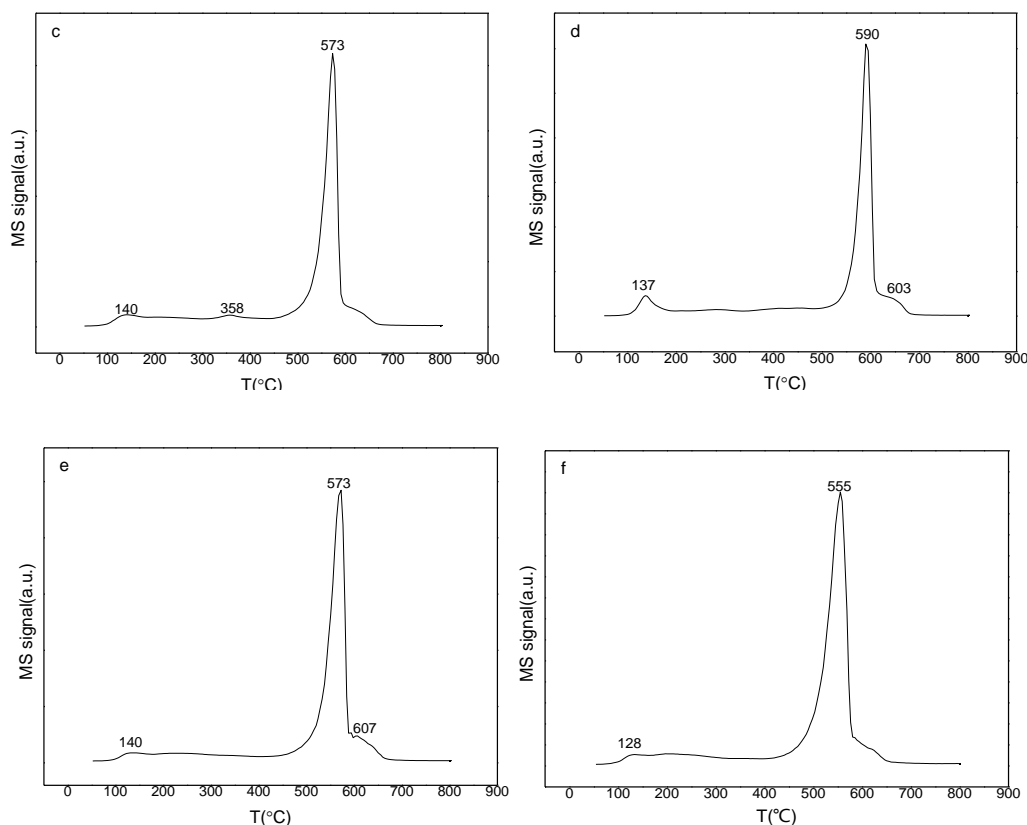
Figure 66 The profiles of desorbed CO$_2$ at the surface of (a) 0.5K30CuFeCNTs, (b) 1K30CuFeCNTs, (c) 1.5K30CuFeCNTs, (d) 1Na30CuFeCNTs, (e) 1Cs30CuFeCNTs and (f) 30CuFeCNTs during CO$_2$-TPD process

Table 32 The quantity of desorbed CO$_2$ and the basic sites at the surface of promoted-catalysts during CO$_2$-TPD process

Catalysts	CO$_2$ desorption (mmol·g^{-1})	Basic sites (mmol·g^{-1})
0.5K30CuFeCNTs	0.57	0.57
1K30CuFeCNTs	0.72	0.72
1.5K30CuFeCNTs	0.67	0.67
1Na30CuFeCNTs	0.74	0.74
1Cs30CuFeCNTs	0.75	0.75
30CuFeCNTs	0.59	0.59

V.3.5 Conclusions for the characterizations

➢ Cu^0 or FeCu$_4$ alloy along with iron oxides and copper iron spinel were formed in

the promoted catalysts.

➢ Promoted catalysts have higher H_2 desorption from metallic phases.

➢ Promoted catalyst have more basic sites than 30CuFeCNTs, except for 0.5K30CuFeCNTs.

V.3.6 Reaction results

The conditions for the tests are similar to the conditions in chapter IV. The tests were performed under 50 bar and the temperature was 250 °C, 300 °C and 350 °C. The GHSV was 5000 h^{-1}. The ratio of CO_2 and H_2 was 3. The catalysts were reduced under pure H_2 at 400 °C for 1 h before the test. The flow rate of feed gas was kept constant, so the mass of catalysts adjusted with respect to the apparent density. The mass of catalysts used for the reaction is shown in

Table 33. In order to collect enough liquid for the analysis, the reaction time is about 70 h at 250 °C, 20 h at 300 °C and 21 h at 350 °C.

Table 33 The mass of catalysts used in reactions

Catalysts	Mass (g)
1Na30CuFeCNTs	0.1524
0.5K30CuFeCNTs	0.1474
1K30CuFeCNTs	0.1521
1.5K30CuFeCNTs	0.1388
1Cs30CuFeCNTs	0.1458

The CO_2 conversions at different temperatures are shown in Figure 67. 1K30CuFeCNTs and 1Cs30CuFeCNTs present similar CO_2 conversion at 250 °C, around 9.3%, and 300 °C, around 21%. Nevertheless, at 350 °C, the CO_2 conversion obtained on 1Cs30CuFeCNTs is much higher than on 1K30CuFeCNTs: 38.5% compared to 26.3%, respectively. 1Na30CuFeCNTs displayed the lowest CO_2 conversion compared to 1K30CuFeCNTs and 1Cs30CuFeCNTs over the whole range of reaction temperature.

Among the K-promoted series, compared to the CO_2 conversion for

0.5K30CuFeCNTs and 1.5K30CuFeCNTs, 1K30CuFeCNTs had the highest CO_2 conversion at low temperature (250 °C), but when temperature increased, the activity of 0.5KCuFeCNTs was largely better than that of 1K30CuFeCNTs and 1.5K30CuFeCNTs. The CO_2 conversion reached 42.5% at 350 °C, which is the highest CO_2 conversion among all the promoted catalysts.

Compared to 30CuFeCNTs, the CO_2 conversions of promoted catalysts are higher at low temperature (250 °C). When temperature increased to 300 °C and 350 °C, only 1K30CuFeCNTs, 1Cs30CuFeCNTs and 0.5K30CuFeCNTs performed better conversion of CO_2 than 30CuFeCNTs.
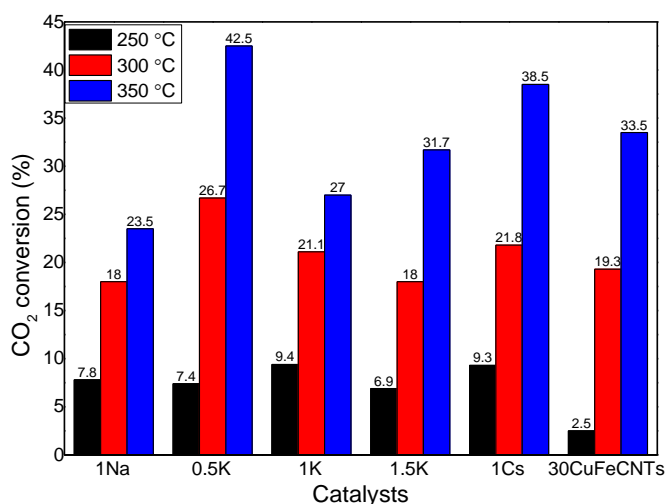
Figure 67 The CO_2 conversion of different temperature for the promoted catalysts and 30CuFeCNTs

Figure 68 displays the H_2 conversion of promoted catalysts and 30CuFeCNTs at 250 °C, 300 °C and 350 °C. Compared to 1K30CuFeCNTs and 1Na30CuFeCNTs, 1Cs30CuFeCNTs has the highest H_2 conversions from 250 °C to 350 °C (6.9%, 24.2% and 47.8% respectively). The H_2 conversion of 1K30CuFeCNTs is a little bit higher than 1Na30CuFeCNTs at 300 °C and 350 °C.

For the loading of different concentration of K, 0.5K30CuFeCNTs displayed higher H_2 activity than 1K30CuFeCNTs and 1.5K30CuFeCNTs, especially at high temperature 300 °C and 350 °C (24.3% and 42.5% respectively).

Compared to 30CuFeCNTs, only 1Cs30CuFeCNTs and 0.5K30CuFeCNTs have higher activities than 30CuFeCNTs at all the reaction temperature.
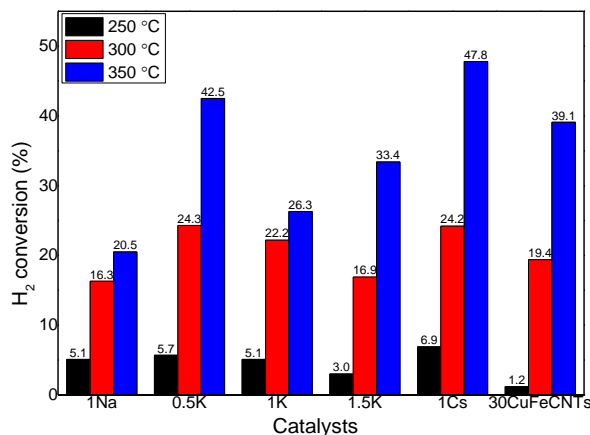
Figure 68 The H_2 conversion of different temperature for the promoted catalysts and 30CuFeCNTs

The stability of the catalytic behavior has been evaluated for three catalysts (0.5K30CuFeCNTs, 1.5K30CuFeCNTs and 1Cs30CuFeCNTs) at 350 °C. The change of CO_2 and H_2 conversions with time are shown in Figure 69.

1Cs30CuFeCNTs and 1.5K30CuFeCNTs have similar stability. CO_2 conversion of 1Cs30CuFeCNTs only decreased of 5% during the reaction time from 21h to 51h, and H_2 conversion only decreased 9%. 0.5K30CuFeCNTs was the most affected catalyst, the CO_2 and H_2 conversions decreased to 18% and 21% respectively during reaction time from 22h to 65h. For 1.5K30CuFeCNTs, the activity for CO_2 is stable, and the conversion only decreased of 6% during reaction time from 14h to 66h at 350 °C, but the H_2 conversion sharply decreased from 33% to 12% during the same reaction time, which may indicate a change in selectivity versus time and different active sites involved in the whole reaction.

Cu and Fe own big difference at the properties as CO_2 adsorbents. Krause *et al.* [14] found that potassium led to a strong interaction between CO_2 and adsorbents, and the properties of iron and copper played at secondary role, and the work of copper and iron with CO_2 were mainly through the interaction of potassium. So suitable loading of potassium can largely increase the conversion of CO_2.
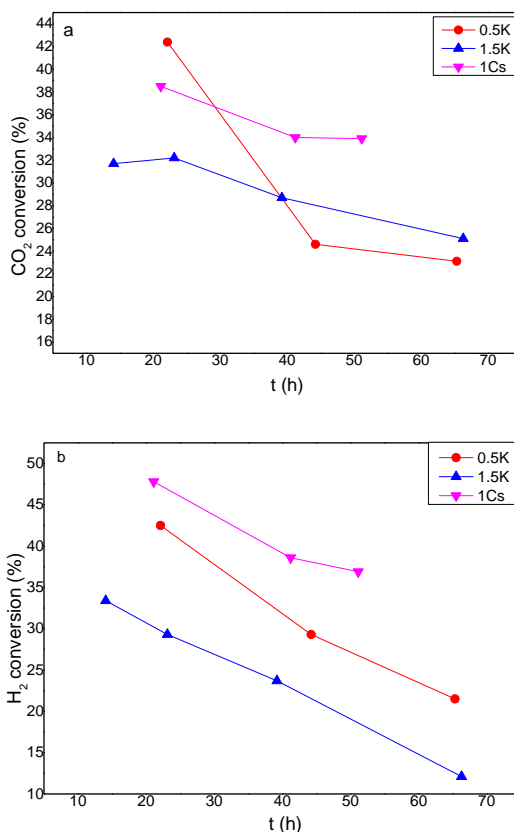
Figure 69 Change of CO_2 (a) and H_2 (b) conversion of 0.5Krepeat30CuFeCNTs,

1.5K30CuFeCNTs and 1Cs30CuFeCNTs at 350 °C with time

The selectivities and productivities of products are shown in Table 34 and Table 35. For all the promoted catalysts, the selectivity to CO decreased with the reaction temperature increase. On the contrary, the selectivities to hydrocarbons increased with reaction temperature, especially the C_{2+} hydrocarbons selectivity. The high temperature is also beneficial for the synthesis of higher alcohols and inhibit the production of methanol. Selectivities and productivities of all the products except for CO and C_{5+} hydrocarbons decreased with increasing loading of K at 250 °C and 300 °C. The concentration of K affects slightly the selectivities to C_{5+} hydrocarbons, but can apparently promote the synthesis of CO. The selectivity to CO increased from 45.2% to 84.4% with the loading K increased from 0.5% to 1.5% percentage at 250 °C. Meanwhile, the selectivity increased from 34.4% to 51.3% at 300 °C. The selectivities to hydrocarbons except for C_{5+} decreased with the increased loading of

promoter K, but the productivities of 1.5KCuFeCNTs are higher than 1KCuFeCNTs. The selectivities and productivities of alcohols included methanol and higher alcohols with 0.5K30CuFeCNTs and 1.5K30CuFeCNTs as catalysts are similar, but selectivities and productivities of alcohols decreased a lot when 1K30CuFeCNTs was used. The highest productivities of higher alcohols is 371.9 $g \cdot kg^{-1} \cdot h^{-1}$ with 0.5KCuFeCNTs as catalyst at 350 °C.

For the reaction at 250 °C, 1Cs30CuFeCNTs shows the highest selectivities and productivities of higher alcohols and hydrocarbons especially C_{2+} hydrocarbons. It also has the lowest selectivity to CO (50.0%). The selectivity and productivity of higher alcohols are 10.0% and 43.9 $g \cdot kg^{-1} \cdot h^{-1}$ respectively. This is almost two times higher than for 1Na30CuFeCNTs (23.7 $g \cdot kg^{-1} \cdot h^{-1}$) and 1K30CuFeCNTs (20.7 $g \cdot kg^{-1} \cdot h^{-1}$).

Although the loading of K changed a little between the three catalysts (0.5K30CuFeCNTs, 1K30CuFeCNTs and 1.5K30CuFeCNTs), the distribution of products changed a lot. The selectivity to CO increased from 45.2% to 84.8% with the loading of K increased from 0.5% to 1.5%, meanwhile, the selectivities to alcohols (methanol and higher alcohols) and hydrocarbons (methane and C_{2+} hydrocarbons) decreased. The selectivities to higher alcohols decreased from 8.0% to 2.0% with the loading of K from 0.5% to 1.5%, and the productivity of higher alcohols of 1.5K30CuFeCNTs is only 6.6 $g \cdot kg^{-1} \cdot h^{-1}$, which is much lower than 30.1 $g \cdot kg^{-1} \cdot h^{-1}$ for 0.5K30CuFeCNTs.

When temperature increased to 300 °C, 1Cs30CuFeCNTs also exhibits the highest selectivity and productivity of hydrocarbons (20.5% and 366.7 $g \cdot kg^{-1} \cdot h^{-1}$). However the highest selectivity and productivity of higher alcohols were obtained in the reaction of 1K30CuFeCNTs as catalyst, 16.6 % and 150.4 $g \cdot kg^{-1} \cdot h^{-1}$ respectively. The selectivity to CO decreased in the order Na>K>Cs.

Same to the reactions at 250 °C, 0.5K30CuFeCNTs also has the highest

selectivities and productivities of alcohols (methanol and higher alcohols) and hydrocarbons. The selectivities to higher alcohols increased to 17.3% and the productivities reached 213.9 g·kg^{-1}·h^{-1}.

With temperature increasing from 300 °C to 350 °C, the selectivities to higher alcohols keep increasing with 1Cs30CuFeCNTs as catalyst, from 10.0% to 16.5%, and the productivities increased from 107.6 to 253.0 g·kg^{-1}·h^{-1}. This is much higher than for 1Na30CuFeCNTs and 1K30CuFeCNTs as catalysts. The use of Cs as promotor can effectively inhibit the synthesis of CO and promote the synthesis of alcohols.

Different from the results at 250 °C and 300 °C, 1.5K30CuFeCNTs presents the highest selectivity to higher alcohols (26.0%) and 0.5K30CuFeCNTs has the highest productivities of higher alcohols (370.7 g·kg^{-1}·h^{-1}) at 350 °C.

Table 34 The selectivities to CO, alcohols, methanol, higher alcohols, hydrocarbon, CH_4, C_{2-5}, C_{5+} and other oxygenates of promoted catalysts and 30CuFeCNTs

Catalysts	T/ °C	CO_2 conversion (%)	Selectivities								
			CO	Alcohols (Total)	Methanol	Higher alcohols	Hydrocarbons (Total)	CH_4	C_{2-5}	C_{5+}	Other oxygenates
1Na30CuFeCNTs		7.8	53.2	14.5	7.8	6.7	31.9	16.0	14.8	1.1	0.1
0.5K30CuFeCNTs		7.4	45.2	15.9	7.0	8.9	38.5	19.3	17.9	1.2	0.1
1K30CuFeCNTs	250	9.4	71.2	6.9	2.0	4.9	21.6	10.4	10.2	1.0	0.1
1.5K30CuFeCNTs		6.9	84.8	2.5	0.5	2.0	12.2	6	5.7	0.5	0.4
1Cs30CuFeCNTs		9.3	50.0	11.7	1.7	10.0	37.8	20	16.6	1.2	0.2
30CuFeCNTs		2.5	50.3	3.4	2.9	0.5	46.2	40.2	6.0	0.0	0.0
1Na30CuFeCNTs		18.0	40.0	17.5	4.5	13.0	41.8	13.7	25.9	2.2	0.3
0.5K30CuFeCNTs		26.7	34.4	21.1	3.8	17.3	43.6	14.7	26.8	2.2	0.3
1K30CuFeCNTs	300	21.1	38.9	18.9	2.3	16.6	41.6	13.8	25.3	2.5	0.4
1.5K30CuFeCNTs		18.0	51.3	15.5	1.2	14.3	32.6	12.1	18.3	2.2	0.4
1Cs30CuFeCNTs		21.8	25.5	15.8	4.5	11.3	57.7	20.5	34.5	2.8	0.3
30CuFeCNTs		19.3	22.8	8.9	3.9	4.9	68.2	35.3	30.9	0.9	0.0
1Na30CuFeCNTs		23.5	38.5	13.6	1.2	12.4	47.1	14.4	30.1	2.6	0.5
0.5K30CuFeCNTs		42.5	31.9	21.7	1.0	20.7	45.5	13.6	29.4	2.5	0.7
1K30CuFeCNTs	350	27.0	39.3	15.1	1.0	14.1	44.9	13.5	28.5	2.9	0.4
1.5K30CuFeCNTs		31.7	29.9	27.2	1.2	26.0	42.1	13.8	25.7	2.7	0.7
1Cs30CuFeCNTs		38.5	14.2	17.2	0.9	16.5	67.5	22.4	42.0	3.1	0.9
30CuFeCNTs		33.5	13.9	9.3	1.6	7.7	76.5	34.1	40.2	2.2	0.3

Table 35 The selectivities to CO, alcohols, methanol, higher alcohols, hydrocarbon, CH_4, C_{2-5}, C_{5+} and other oxygenates of promoted catalysts and 30CuFeCNTs

Catalysts	T/ °C	CO_2 conversion (%)	Productivities (g·kg^{-1}·h^{-1})								
			CO	Alcohols (Total)	Methanol	Higher alcohols	Hydrocarbons (Total)	CH_4	C_{2-5}	C_{5+}	Other oxygenates
1Na30CuFeCNTs		7.8	232.1	92.1	68.5	23.7	76.8	40.1	34.2	2.5	0.5
0.5K30CuFeCNTs		7.4	189.2	88.7	56.1	30.1	88.7	46.4	39.5	2.8	0.4
1K30CuFeCNTs	250	9.4	376.0	41.5	20.8	20.7	62.5	31.5	28.1	2.9	0.4
1.5K30CuFeCNTs		6.9	348.9	10.8	4.2	6.6	27.3	14.1	12.2	1.0	1.5
1Cs30CuFeCNTs		9.3	268.1	62.0	18.1	43.9	111.9	61.3	46.9	3.7	0.8
30CuFeCNTs		2.5	73.4	9.1	8.5	0.6	38.3	33.6	4.7	0.0	0.0
1Na30CuFeCNTs		18.0	386.3	190.1	88.4	101.7	216.1	75.8	129.2	11.2	2.6
0.5K30CuFeCNTs		26.7	523.6	329.6	56.1	213.9	359.6	128.3	213.3	18.0	4.6
1K30CuFeCNTs		21.1	433.9	201.0	50.6	150.4	247.5	88.1	144.9	14.4	3.5
1.5K30CuFeCNTs	300	18.0	530.7	145	25.4	119.6	180.7	71.9	97.2	11.6	3.4
1Cs30CuFeCNTs		21.8	298.6	212.1	104.5	107.6	366.7	137.5	211.5	17.7	3.5
30CuFeCNTs		19.3	244.6	127.6	84.9	42.8	401.1	217.2	177.1	6.8	0.0
1Na30CuFeCNTs		23.5	483.5	156.1	30.2	125.8	316.4	103.8	195.2	17.4	5.0
0.5K30CuFeCNTs		42.5	705.1	417.9	56.0	370.7	539.6	172.7	337.3	29.5	12.6
1K30CuFeCNTs		27.0	543.3	185.8	28.4	157.5	330.7	106.8	202.6	21.3	5.4
1.5K30CuFeCNTs	350	31.7	510.5	401.2	41.1	360.1	383.1	134.4	224.8	23.9	9.8
1Cs30CuFeCNTs		38.5	272.7	287.7	34.7	253.0	697.0	246.4	418.8	31.8	14.7
30CuFeCNTs		33.5	244.3	167.0	58.1	108.9	743.7	343.3	377.8	22.5	5.9

The effect of reaction time on the distribution of products is presented in Figure 70. From the results, it can be said that the selectivities to hydrocarbons have a slight increase during the very beginning 24 h and then keep decreasing. The selectivity to CO keeps increasing and the selectivities to alcohols keep decreasing during the whole reaction. Promoter Cs leads to the best stability in the product distribution in the synthesis of higher alcohols.
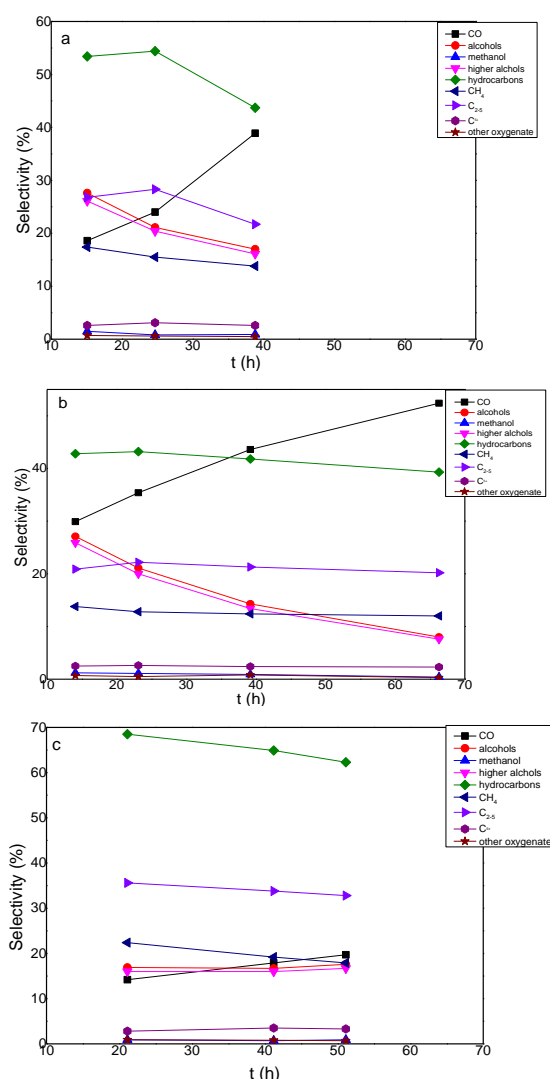

Figure 70 The change of selectivities to products with time with
(a) 0.5K30CuFeCNTs, (b) 1.5K30CuFeCNTs, (c) 1Cs30CuFeCNTs

As conclusion for the reaction results, the suitable addition of alkalis as promoters can effectively increase CO$_2$ and H$_2$ conversions and promote the selectivity and productivity of higher alcohols compared to catalyst without promoters

(30CuFeCNTs). The concentration and species of promoters, reaction temperature and reaction time can affect the distribution of products.

V.3.7 The characterizations of catalysts after reactions

V.3.7.1 X-ray Diffraction (XRD) after reaction

The XRD patterns of promoted catalysts after reactions are shown in Figure 71. Fe_5C_2 carbides were detected in the catalyst, which is the active phase for FT reaction [15]. Compared to the XRD patterns of catalysts before reaction, the iron oxides and copper iron spinel disappeared.
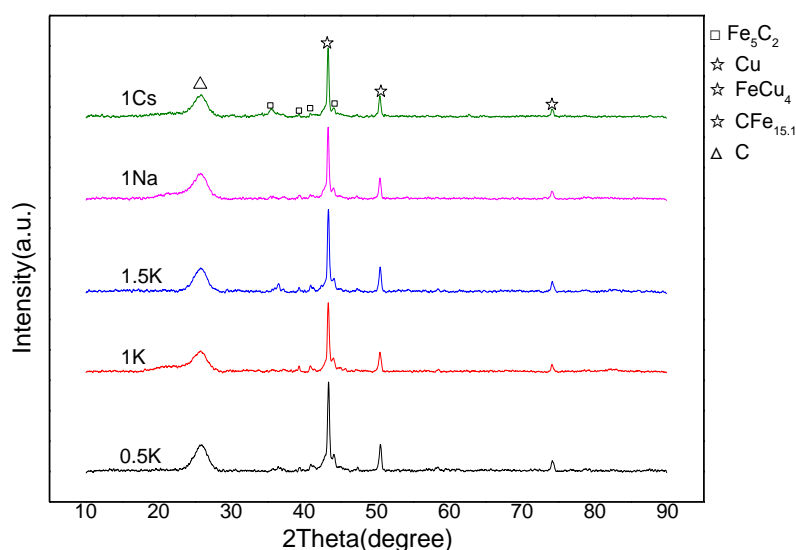
Figure 71 XRD profiles of catalysts after reaction

V.3.7.2 Transmission Electron Microscopy (TEM) after reaction

The TEM images of catalyst 1K30CuFeCNTs after reaction are presented in Figure 72. Compared to the results before reaction, there are only several core-shell structure of particles which disperse among carbon nanotubes. The core is around

154

20nm and the shell is between 3-6nm. The metals phases may sinter during the reaction.

The lattice spacing 0.32 nm agrees with the (002) spacing of graphitic carbon [16, 17], and 0.21 nm corresponds to Fe_5C_2 (510) (0.205nm)[18] or Cu (111) or $FeCu_4$ (111) [19], which is consistent with the XRD results.
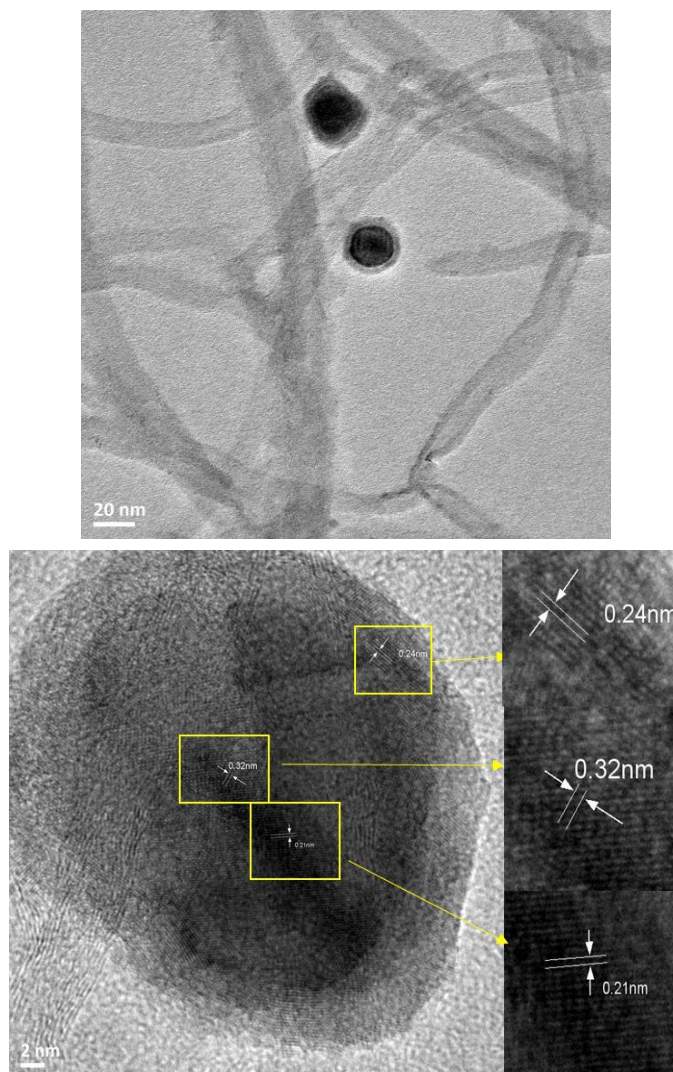
Figure 72 The TEM images of 1K30CuFeCNTs after reaction

V.4 Discussion

The selectivities to higher alcohols have been greatly increased by adding alkalis as dopants. The addition of alkalis promoters can deeply affect the distribution of products and effectively increase selectivity and productivity of higher alcohols. The

dopants can either act as electronic promoters or as structural promoters, or possibly as both [20, 21]. From the results of XRD and TEM, we can found that the addition of alkalis can promote the formation of iron carbide, which is a key active phases for the activity of Fischer-Tropsch reaction. More, the alkalis can modify the surface properties and increase the basic sites, as it has been shown before. It also can lower the electron density of d-vacant metals such as Fe by donating electrons [22] and enhance the dissociative adsorption of CO and lower the adsorption of H_2 [20]. Compared to 30CuFeCNTs, the selectivities for hydrocarbons decreased a lot (less than 50%), which may be due to the blocking of acid sites.

The suitable amount of alkalis depends on the properties of the supports and the nature of the promoter. For example potassium in this reaction, 0.5KCuFeCNTs clearly promotes selectivity and productivity of high alcohols better than 1K30CuFeCNTs. At too high concentration, potassium may block the active phases and decrease the activity. 1Cs30CuFeCNTs also presented better performance than 1K30CuFeCNTs at high temperature (350 °C). Cesium is known as perfect promoter to stabilize the formyl intermediate species [23,24], this may lead to the higher stability of catalyst 1Cs30CuFeCNTs, even at 350 °C.

The synthesis of higher alcohols from CO_2 hydrogenation is a difficult reaction, and there are few researchers about this reaction. The results in our reaction are much better than the others, even compared to the synthesis of higher alcohols from CO hydrogenation [25, 26]. In the study of Haijun Guo *et al.* [25], the highest selectivity of higher alcohols was only about 3.8% from the CO_2 hydrogenation and at 350 °C and 6 MPa. Guilong Liu *et al.*[27] synthesized the higher alcohols from syngas based on Cu-Co/Li_2O_3-SiO_2 catalyst, and the highest productivity of higher alcohols is only 52.5 g·kg^{-1}·h^{-1} at 330 °C and 3 MPa.

V.5 Conclusions

The utilization of alkalis as promoters does not only lead to increase the

conversion of CO_2 and H_2, but also enhance the selectivities to the desired products, higher alcohols. The performance of promoters can be affected by the concentration, reaction temperature and reaction time. The catalyst 0.5K30CuFeCNTs owns the highest productivities (370.7 $g\cdot kg^{-1}\cdot h^{-1}$) of higher alcohols at 350 °C and 50 bar, and 1.5K30CuFeCNTs has the highest selectivity (26.0%) of high alcohols at 350 °C.

V.6 Literatures

[1] Y.K. Park, K.C. Park, S.K. Ihm, Hydrocarbon synthesis through CO$_2$ hydrogenation over CuZnOZrO$_2$/zeolite hybrid catalysts, Catalysis Today, 44 (1998) 165-173.

[2] S.H. Kang, J.W. Bae, P.S.S. Prasad, K.W. Jun, Fischer-Tropsch synthesis using zeolite-supported iron catalysts for the production of light hydrocarbons, Catalysis Letters, 125 (2008) 264-270.

[3] Y.L. Su, Y. Liu, Y.Q. Guo, Z.M. Liu, Effect of alumina on Fe-Cu-Zn-K-Al catalyst for synthesis of higher alcohols, Chinese Journal of Catalysis, 24 (2003) 799-803.

[4] N. Tien-Thao, M.H. Zahedi-Niaki, H. Alamdari, S. Kaliaguine, Effect of alkali additives over nanocrystalline Co-Cu-based perovskites as catalysts for higher-alcohol synthesis, Journal of Catalysis, 245 (2007) 348-357.

[5] A.F. Noels, A. Demonceau, A.J. Hubert, P. Teyssie, C.A.G. Dodet, P. Meunier, A.H.N. Germain, Higher Alcohols Synthesis over Alkali-Metal Promoted Co-Cu-Zn Catalysts, Hung J Ind Chem, 21 (1993) 27-33.

[6] T. Ishida, T. Yanagihara, X.H. Liu, H. Ohashi, A. Hamasaki, T. Honma, H. Oji, T. Yokoyama, M. Tokunaga, Synthesis of higher alcohols by Fischer-Tropsch synthesis over alkali metal-modified cobalt catalysts, Appl Catal A Gen, 458 (2013) 145-154.

[7] A.M. Hilmen, M.T. Xu, M.J.L. Gines, E. Iglesia, Synthesis of higher alcohols on copper catalysts supported on alkali-promoted basic oxides, Appl Catal A Gen, 169 (1998) 355-372.

[8] J. Sun, Q.X. Cai, Y. Wan, S.L. Wan, L. Wang, J.D. Lin, D.H. Mei, Y. Wang, Promotional Effects of Cesium Promoter on Higher Alcohol Synthesis from Syngas over Cesium-Promoted Cu/ZnO/Al$_2$O$_3$ Catalysts, Acs Catalysis, 6 (2016) 5771-5785.

[9] M.G. Lin, K.G. Fang, D.B. Li, Y.H. Sun, Effect of Zn and Mn promoters on copper-iron based catalysts for higher alcohol synthesis, Acta Phys-Chim Sin, 24 (2008) 833-838.

[10] P. Moriceau, B. Taouk, E. Bordes, P. Courtine, Correlations between the optical basicity of catalysts and their selectivity in oxidation of alcohols, ammoxidation and

combustion of hydrocarbons, Catalysis Today, 61 (2000) 197-201.

[11] X.M. Yang, Y. Wei, Y.L. Su, L.P. Zhou, Characterization of fused Fe-Cu based catalyst for higher alcohols synthesis and DRIFTS investigation of TPSR, Fuel Processing Technology, 91 (2010) 1168-1173.

[12] X.M. Ma, G.D. Lin, H.B. Zhang, Co-decorated carbon nanotube-supported Co-Mo-K sulfide catalyst for higher alcohol synthesis, Catalysis Letters, 111 (2006) 141-151.

[13] X. Dong, H.B. Zhang, G.D. Lin, Y.Z. Yuan, K.R. Tsai, Highly active CNT-promoted Cu-ZnO-Al_2O_3 catalyst for methanol synthesis from H_2/CO/CO_2, Catalysis Letters, 85 (2003) 237-246.

[14] J. Krause, D. Borgmann, G. Wedler, Photoelectron spectroscopic study of the adsorption of carbon dioxide on Cu(110) and Cu(110)/K - As compared with the systems Fe(110)/CO_2 and Fe(110)/(K+ CO_2), Surf Sci, 347 (1996) 1-10.

[15] W. Wang, S.P. Wang, X.B. Ma, J.L. Gong, Recent advances in catalytic hydrogenation of carbon dioxide, Chemical Society reviews, 40 (2011) 3703-3727.

[16] H.C. Zhang, H. Ming, S.Y. Lian, H. Huang, H.T. Li, L.L. Zhang, Y. Liu, Z.H. Kang, S.T. Lee, Fe_2O_3/carbon quantum dots complex photocatalysts and their enhanced photocatalytic activity under visible light, Dalton transactions, 40 (2011) 10822-10825.

[17] X.Z. Wang, Z.B. Zhao, J.Y. Qu, Z.Y. Wang, J.S. Qiu, Fabrication and characterization of magnetic Fe_3O_4-CNT composites, J Phys Chem Solids, 71 (2010) 673-676.

[18] V. Vij, J.N. Tiwari, W.G. Lee, T. Yoon, K.S. Kim, Hemoglobin-carbon nanotube derived noble-metal-free Fe_5C_2-based catalyst for highly efficient oxygen reduction reaction, Scientific reports, 6 (2016).

[19] K. Xiao, Z.H. Bao, X.Z. Qi, X.X. Wang, L.S. Zhong, M.G. Lin, K.G. Fang, Y.H. Sun, Unsupported CuFe bimetallic nanoparticles for higher alcohol synthesis via syngas, Catalysis Communications, 40 (2013) 154-157.

[20] S. Saeidi, N.A.S. Amin, M.R. Rahimpour, Hydrogenation of CO_2 to value-added products-A review and potential future developments, Journal of CO_2 Utilization, 5

(2014) 66-81.

[21] R.W. Dorner, D.R. Hardy, F.W. Williams, H.D. Willauer, Heterogeneous catalytic CO_2 conversion to value-added hydrocarbons, Energ Environ Sci, 3 (2010) 884-890.

[22] T.S. M.E. Dry, L.J. Boshoff, G.J. Oosthuizen, Heats of chemisorption on promoted iron surfaces and the role of alkali in Fischer-Tropsch synthesis, Journal of Catalysis, 15 (1969) 190-199.

[23] M.T. Xu, E. Iglesia, Carbon-carbon bond formation pathways in CO hydrogenation to higher alcohols, Journal of Catalysis, 188 (1999) 125-131.

[24] A. Cosultchi, M. Perez-Luna, J.A. Morales-Serna, M. Salmon, Characterization of Modified Fischer-Tropsch Catalysts Promoted with Alkaline Metals for Higher Alcohol Synthesis, Catalysis Letters, 142 (2012) 368-377.

[25] H.J. Guo, S.G. Li, F. Peng, H.R. Zhang, L. Xiong, C. Huang, C. Wang, X.D. Chen, Roles Investigation of Promoters in K/Cu-Zn Catalyst and Higher Alcohols Synthesis from CO_2 Hydrogenation over a Novel Two-Stage Bed Catalyst Combination System, Catalysis Letters, 145 (2015) 620-630.

[26] C. Sun, D.S. Mao, L.P. Han, J. Yu, Effect of impregnation sequence on performance of SiO_2 supported Cu-Fe catalysts for higher alcohols synthesis from syngas, Catalysis Communications, 84 (2016) 175-178.

[27] G.L. Liu, T. Niu, D.M. Pan, F. Liu, Y. Liu, Preparation of bimetal Cu-Co nanoparticles supported on meso-macroporous SiO_2 and their application to higher alcohols synthesis from syngas, Appl Catal A Gen, 483 (2014) 10-18.

Chapter VI

Conclusions and perspectives

The synthesis of higher alcohols from CO_2 hydrogenation is a useful and interesting reaction, but it is also a very difficult reaction. In this thesis, different kinds of metals, supports and promoters were in view of designing an optimal catalytic system being able to be active and to promote the selective formation of higher alcohols with respect to CO, methanol, methane and higher hydrocarbons.

Four kinds of spinel-based catalysts ($CoFe_2O_4$, $CuFe_2O_4$, $CuCo_2O_4$, $Cu_{0.5}Co_{0.5}Fe_2O_4$) were prepared by pseudo sol-gel method. The $CoFe_2O_4$ spinel can be easily synthesized and high calcination temperature increase crystallinity of spinel phase. For $CuFe_2O_4$ spinel, the $CuFe_2O_4$ spinel is always formed along with CuO, high calcination temperature can lead to Cu-deficiency copper iron spinel. $CuCo_2O_4$ spinel is the most difficult to be synthesized, because of the low thermal stability there are mainly CuO and Co_3O_4 in the CuCo-precursor after calcination at high temperature. For Cu, Co and Fe mixed catalyst, the phases CuFe-spinel and CoFe-spinel may have been formed in the material after calcination, but the CuCoFe mixed spinel was not evidenced by XRD.

The four kinds of spinel-based catalysts were tested in a fixed bed reactor under 50 bar with a ratio of H_2/CO_2 equal to 3 from 250 °C to 350 °C. From the distribution of products, it can be found that Cu, Co and Fe elements work differently. CoFe-precursor-800 catalyst is more suitable for the synthesis of hydrocarbons especially C_{2+} hydrocarbons. CuCo-precursor-800 is better to be used for the synthesis of methane and methanol. CuFe-precursor-800 is beneficial for the synthesis of C_{2+} hydrocarbons and higher alcohols. In the CO_2 hydrogenation, Co acts as a methanation catalyst rather than acting as a FT catalyst, because of the different reaction mechanism between CO hydrogenation and CO_2 hydrogenation. In order to inhibit the formation of huge amount of hydrocarbons, it is better to choose catalysts without Co in the CO_2 hydrogenation reaction.

In order to increase the surface area of spinel-based catalysts and increase the selectivity to higher alcohols, CNTs and TUD-1 were chosen as supports for CuFe-precursor-800 catalyst. The study shows that a proper support and suitable

162

loading of active phases can deeply effect the distribution of products. The CNTs can promote the synthesis of iron carbides, which is essential for the Fischer-Tropsch reactivity. The TUD-1 support are more suitable for synthesis of single-carbon products (methane and methanol). CNTs is a perfect support for the synthesis of long-chain products (higher alcohols and C_{2+} hydrocarbons). The selectivity to higher alcohols increased a little compared to CuFe-precursor-800. There are only metallic copper and iron in the catalyst after reduction, which may limit the synthesis of higher alcohols.

Alkalis (Na, K, Cs) were chosen as promoters to decrease the selectivity to hydrocarbons and increase the selectivity to higher alcohols for CuFe/CNTs catalysts. The addition of alkalis as promoters does not only lead to increase the conversion of CO_2 and H_2, but also enhance the selectivity to the desired products, higher alcohols. The performance of promoted catalyst can be affected by the loading of promoter, reaction temperature and reaction time. The catalyst 0.5K30CuFeCNTs owns the highest productivities (370.7 $g \cdot kg^{-1} \cdot h^{-1}$) of higher alcohols at 350 °C and 50 bar, and 1.5K30CuFeCNTs has the highest selectivity (26.0%) of high alcohols at 350 °C. 1Cs30CuFeCNTs has the highest stability for higher alcohols synthesis. The results are much higher than the similar studies.

The addition of alkalis apparently increased the amount of basic sites, which may be responsible for the higher selectivity of higher alcohols. According to the results, the alkalis can act as electronic promoter or structural promoter or both.

According to a series of study and test, the selectivity to higher alcohols increased a lot than pure spinel-based catalyst, but there are still many properties of catalysts which can be studied, modified and improved.

The mechanism of the effect of alkalis promoters to the distribution of products need to be deeply studied.

Better promoters can be chosen to increase the cooperation of two active sites and increase the selectivity of higher alcohols. Mn, for example, can active as structural promoter and electronic promoter.

UNIVERSITÉ DE STRASBOURG

Qinqin JI

The synthesis of higher alcohols from CO$_2$ hydrogenation with Co, Cu, Fe-based catalysts

ICPEES
Institut de Chimie et
Procédés pour l'Énergie,
l'Environnement et la Santé

Résumé

Le CO$_2$ est une source de carbone propre pour les réactions chimiques, nombreux chercheurs ont étudié l'utilisation du CO$_2$. Les alcools supérieurs sont des additifs de carburant propres. La synthèse des alcools supérieurs à partir de l'hydrogénation du CO a également été étudiée par de nombreux chercheurs, mais il existe peu de littératures sur la synthèse des alcools supérieurs à partir de l'hydrogénation du CO$_2$, qui est une réaction complexe et difficile. Les catalyseurs utilisés pour la synthèse des alcools supérieurs nécessitent au moins deux phases actives et une bonne synergie. Dans notre étude, nous avons etudié les catalyseurs spinelle basés sur Co. Cu. Fe et l'effet des supports (CNTs et TUD-1) et celui des promoteurs (K, Na, Cs) à la réaction de HAS. Nous avons trouvé que le catalyseur CuFe-précurseur-800 est favorable pour la synthèse d'hydrocarbures en C$_{2+}$ et d'alcools supérieurs. Dans l'hydrogénation du CO$_2$, Co agit comme catalyseur de méthanisation plutôt que comme catalyseur FT, en raison du mécanisme de réaction différent entre l'hydrogénation du CO et celle du CO$_2$. Afin d'inhiber la formation d'hydrocarbures de quantités importante, il est préférable de choisir des catalyseurs sans Co dans la réaction d'hydrogénation du CO$_2$. En comparant les fonctions des CNT et du TUD-1, nous avons constaté que le CNT est un support parfait pour la synthèse de produits à longue chaîne (alcools supérieurs et hydrocarbures C$_{2+}$). Le support TUD-1 est plus adapté à la synthèse de produits à un seul carbone (méthane et méthanol) .L'addition d'alcalis en tant que promoteurs conduit non seulement à augmenter la conversion de CO$_2$ et H$_2$, mais augmente également la sélectivité des produits visés fortement, des alcools supérieurs. Le catalyseur 0.5K30CuFeCNTs possède une productivités les plus élevées (370.7 g · kg^{-1} · h^{-1}) d'alcools supérieurs à 350 ° C et 50 bar.

Mots clé : CO$_2$, hydrogénation, alcools supérieurs, spinelle

Résumé en anglais

CO$_2$ is a clean carbon source for the chemical reactions, many researchers have studied the utilization of CO$_2$. Higher alcohols are clean fuel additives. The synthesis of higher alcohols from CO hydrogenation has also been studied by many researchers, but there are few literatures about the synthesis of higher alcohols from CO$_2$ hydrogenation, which is a complex and difficult reaction. The catalysts that used for higher alcohols synthesis need at least two active phases and good cooperation. In our study, we tested the Co. Cu. Fe spinel-based catalysts and the effect of supports (CNTs and TUD-1) and promoters (K, Na, Cs) to the HAS reaction. We found that catalyst CuFe-precursor-800 is beneficial for the synthesis of C$_{2+}$ hydrocarbons and higher alcohols. In the CO$_2$ hydrogenation, Co acts as a methanation catalyst rather than acting as a FT catalyst, because of the different reaction mechanism between CO hydrogenation and CO$_2$ hydrogenation. In order to inhibit the formation of huge amount of hydrocarbons, it is better to choose catalysts without Co in the CO$_2$ hydrogenation reaction. Compared the functions of CNTs and TUD-1, we found that CNTs is a perfect support for the synthesis of long-chain products (higher alcohols and C$_{2+}$ hydrocarbons). The TUD-1 support are more suitable for synthesis of single-carbon products (methane and methanol).The addition of alkalis as promoters does not only lead to increase the conversion of CO$_2$ and H$_2$, but also sharply increased the selectivity to the desired products, higher alcohols. The catalyst 0.5K30CuFeCNTs owns the highest productivities (370.7 g·kg^{-1}·h^{-1}) of higher alcohols at 350 °C and 50 bar.

Keywords: CO$_2$, hydrogenation, higher alcohols, spinel